1994-06

The diurnal cycle of high-frequency temperature variability at 0*, 140*W on seasonal and interannual time scales

Brainard, Russell E.

Monterey, California. Naval Postgraduate School

NAVAL POSTGRADUATE SCHOOL
Monterey, California

DISSERTATION

THE DIURNAL CYCLE OF HIGH-FREQUENCY TEMPERATURE VARIABILITY AT 0°,140°W ON SEASONAL AND INTERANNUAL TIME SCALES

by

Russell E. Brainard

June 1994

Dissertation Supervisor: Roland W. Garwood, Jr.

REPORT DOCUMENTATION PAGE

Form Approved
OMB No. 0704-0188

1. AGENCY USE ONLY (Leave blank)	2. REPORT DATE	3. REPORT TYPE AND DATES COVERED
	16 June 1994	Doctoral Dissertation

4. TITLE AND SUBTITLE
THE DIURNAL CYCLE OF HIGH-FREQUENCY TEMPERATURE VARIABILITY AT 0°, 140°W ON SEASONAL AND INTERANNUAL TIME SCALES

5. FUNDING NUMBERS

6. AUTHOR(S)

Russell E. Brainard

7. PERFORMING ORGANIZATION NAME(S) AND ADDRESS(ES)

Naval Postgraduate School
Department of Oceanography
Monterey, CA 93943-5000

Pacific Marine Environmental Laboratory
7600 Sand Point Way N.E.
Seattle, WA 98115-0070

8. PERFORMING ORGANIZATION REPORT NUMBER

9. SPONSORING / MONITORING AGENCY NAME(S) AND ADDRESS(ES)

Naval Postgraduate School
Department of Oceanography
Monterey, CA 93943-5000

Pacific Marine Environmental Laboratory
7600 Sand Point Way N.E.
Seattle, WA 98115-0070

10. SPONSORING / MONITORING AGENCY REPORT NUMBER

11. SUPPLEMENTARY NOTES

12a. DISTRIBUTION / AVAILABILITY STATEMENT

Approved for public release; distribution is unlimited.

12b. DISTRIBUTION CODE

13. ABSTRACT *(Maximum 200 words)*

The diurnal cycle of high-frequency temperature fluctuations attributable to turbulence and internal waves in the upper central equatorial Pacific Ocean is found to persist over most of the period November 1983 - October 1987. Moored temperature and velocity data in the upper 300 m at 0°, 140°W during this four-year period were used to: 1) determine the vertical extent of the diurnal cycle of turbulence and internal waves and evaluate its contribution to the equatorial zonal momentum balance, and 2) determine whether the diurnal cycle of turbulence and internal waves varied seasonally and interannually in response to varying surface forcing and ambient stability conditions. Using 15-minute spot-sampled temperature data at 35 m, 60 m, 100 m, 140 m, 200 m, and 300 m, isotherm displacement variance (IDV) was computed for each six-hour time period as a proxy for vertical overturning and displacement associated with turbulence and internal waves. The time series of monthly mean IDV for each of the six-hour time bins showed the magnitude of the diurnal cycle of turbulence and internal waves (ΔIDV) as a function of season and depth.

The diurnal change in IDV was pronounced at both the 35-m and the 60-m depths, with nighttime IDV significantly greater than daytime IDV. This result is consistent with TROPIC HEAT microstructure observations over two periods of a few days to weeks, showing that IDV is a useful proxy for turbulence and internal wave energy during periods when microstructure measurements are not available. The magnitude of ΔIDV decayed sharply with depth below 60 m, indicating that little diurnally-modulated internal gravity wave energy had propagated down through the equatorial undercurrent core. Hence, internal wave propagation does not appear to be important for loss of zonal momentum to the regions below the core

14. SUBJECT TERMS	15. NUMBER OF PAGES
Equatorial Ocean Dynamics, Turbulence, Internal Waves, Diurnal Cycle of Upper Ocean Processes, Seasonal and Interannual Variability of Upper Ocean.	169
	16. PRICE CODE

17. SECURITY CLASSIFICATION OF REPORT	18. SECURITY CLASSIFICATION OF THIS PAGE	19. SECURITY CLASSIFICATION OF ABSTRACT	20. LIMITATION OF ABSTRACT
Unclassified	Unclassified	Unclassified	Unlimited

abstract con't

of the undercurrent.

Monthly means of both IDV and ΔIDV at 35 m and 60 m suggest that turbulence and internal waves varied over seasonal and interannual time scales. Seasonally, maxima of IDV and ΔIDV occurred during the boreal winter, when wind speed and mixed-layer depth were at their annual maxima and shortwave radiation was at its annual minimum. Minima of IDV and ΔIDV occurred during the boreal spring, when wind speed and mixed-layer depth were at their annual minima and shortwave radiation was at its annual maximum. Over the 48-month period of study, ΔIDV at 35 m and 60 m were significantly correlated with wind speed, zonal wind, mixed-layer depth, diurnal range of mixed-layer depth, buoyancy frequency, and shortwave radiation. The strong correlations are consistent with the use of IDV as a proxy for turbulence-wave processes associated with shear production and buoyancy flux in the marginally stable entrainment zone between the surface well-mixed layer and the undercurrent core.

Approved for public release; distribution is unlimited

The Diurnal Cycle of High-Frequency Temperature Variability at 0°,140°W On Seasonal and Interannual Time Scales

by

Russell E. Brainard
Lieutenant Commander, NOAA
B.S., Marine Science, Texas A&M University, 1981
M.S., Oceanography, Naval Postgraduate School, 1986

Submitted in partial fulfillment of the
requirements for the degree of

DOCTOR OF PHILOSOPHY IN PHYSICAL OCEANOGRAPHY

from the

NAVAL POSTGRADUATE SCHOOL

June 1994

Author: [redacted]
Russell E. Brainard

Approved by:

[redacted]
Roland W. Garwood, Jr.
Professor of Oceanography
Dissertation Supervisor

[redacted]
Michael J. McPhaden
External Member
PMEL, NOAA

[redacted]
Albert J. Semtner
Professor of Oceanography

[redacted]
Steven R. Ramp
Associate Research Professor of Oceanography

[redacted]
Kenneth L. Davidson
Professor of Meteorology

[redacted]
Maurice D. Weir
Professor of Mathematics

Approved by: [redacted]
Curtis A. Collins, Chairman, Department of Oceanography

Approved by: [redacted]
Richard S. Elster, Dean of Instruction

ABSTRACT

The diurnal cycle of high-frequency temperature fluctuations attributable to turbulence and internal waves in the upper central equatorial Pacific Ocean is found to persist over most of the period November 1983 - October 1987. Moored temperature and velocity data in the upper 300 m at 0°, 140°W during this four-year period were used to: 1) determine the vertical extent of the diurnal cycle of turbulence and internal waves and evaluate its contribution to the equatorial zonal momentum balance, and 2) determine whether the diurnal cycle of turbulence and internal waves varied seasonally and interannually in response to varying surface forcing and ambient stability conditions. Using 15-minute spot-sampled temperature data at 35 m, 60 m, 100 m, 140 m, 200 m, and 300 m, isotherm displacement variance (IDV) was computed for each six-hour time period as a proxy for vertical overturning and displacement associated with turbulence and internal waves. The time series of monthly mean IDV for each of the six-hour time bins showed the magnitude of the diurnal cycle of turbulence and internal waves (ΔIDV) as a function of season and depth.

The diurnal change in IDV was pronounced at both the 35-m and the 60-m depths, with nighttime IDV significantly greater than daytime IDV. This result is consistent with TROPIC HEAT microstructure observations over two periods of a few days to weeks, showing that IDV is a useful proxy for turbulence and internal wave energy during periods when microstructure measurements are not available. The magnitude of ΔIDV decayed sharply with depth below 60 m, indicating that little diurnally-modulated internal gravity wave energy had propagated down through the equatorial undercurrent core. Hence, internal wave propagation does not appear to be important for loss of zonal momentum to the regions below the core of the undercurrent.

Monthly means of both IDV and ΔIDV at 35 m and 60 m suggest that turbulence and internal waves varied over seasonal and interannual time scales. Seasonally, maxima of IDV and ΔIDV occurred during the boreal winter, when wind speed and mixed-layer depth were at their annual maxima and shortwave radiation was at its annual minimum. Minima of IDV and ΔIDV occurred during the boreal spring, when wind speed and

mixed-layer depth were at their annual minima and shortwave radiation was at its annual maximum. Over the 48-month period of study, ΔIDV at 35 m and 60 m were significantly correlated with wind speed, zonal wind, mixed-layer depth, diurnal range of mixed-layer depth, buoyancy frequency, and shortwave radiation. These strong correlations are consistent with the use of IDV as a proxy for turbulence-wave processes associated with shear production and buoyancy flux in the marginally stable entrainment zone between the surface well-mixed layer and the undercurrent core.

TABLE OF CONTENTS

LIST OF TABLES

LIST OF FIGURES

ACKNOWLEDGEMENTS

I would like to thank my advisor and committee chairman, Bill Garwood, for continued guidance, support and encouragement over the duration of my graduate education. Spanning five NOAA Corps assignments (from the South Pole to Monterey to Honolulu to Monterey to Seattle) and a couple of topic changes, Bill's patience, persistence, and friendship helped me navigate the shoals of the doctoral process. I would also like to thank my co-advisor, Mike McPhaden, for helping me identify this research topic, allowing me to use the TOGA TAO mooring data, and for providing outstanding scientific guidance and insight. Steve Ramp, Bert Semtner, Ken Davidson and Maurice Weir provided valuable suggestions that contributed to improving this dissertation. Stimulating discussions and collaborations with Niklas Schneider, Ren-Chieh Lien, Eric Skyllingstad, Hemantha Wijesekera, Janet Sprintall, Bill Lavelle, Arlene Bird, and Billy Kessler were extremely helpful throughout this research. I am indebted to the fine scientific and support staff at PMEL for assisting in many of the technical details of this undertaking, particularly Margie McCarty, Paul Freitag, Nancy Soreide, Dai McClurg, and Jerry Davison. I thank John Bullister for allowing me to use his computers and office for improved word processing. I thank James Beauchamp for providing the ISCCP solar irradiance data and helpful discussions. I am also indebted to the NOAA Corps and the many senior officers who supported and encouraged these graduate studies over the years.

I would like to thank my friends at the Naval Postgraduate School, Pacific Fisheries Environmental Group, Pacific Marine Environmental Laboratory, and my fellow officers in the NOAA Corps for helping me enjoy these graduate school years. My friends helped me keep a somewhat balanced perspective and continue to experience some aspects of a normal life. Special thanks to Mimi Brainard who shared most of the highs and lows of this effort and provided continued encouragement throughout. Finally, I would like to thank my family for always being understanding and supportive.

I. INTRODUCTION

A. INTRODUCTION

In recent years, we have become increasingly aware of the variable nature of the earth's climate and of the need to predict climatic variations arising from natural and man-made causes. The large El Nino/Southern Oscillation (ENSO) event of 1982-83 focused attention on understanding the interaction of the ocean and atmosphere in the equatorial Pacific Ocean (Cane, 1983; Rasmussen and Wallace, 1983). The Southern Oscillation, an aperiodic interannual fluctuation between warm and cold oceanic states, has its largest signature in and over the tropical Pacific and Indian Oceans, but it is known to affect oceanic and atmospheric conditions globally (Philander, 1990). Numerical modeling experiments have shown that most of the interannual variability of the tropical atmosphere is related to the changes in the boundary conditions at the ocean surface, particularly sea surface temperature (SST) fluctuations associated with El Nino (Lau, 1981, Shukla and Wallace, 1983). SST anomalies in the equatorial Pacific modify the fluxes of heat and moisture between the ocean and atmosphere and have been linked to displacement of large-scale atmospheric circulation patterns over the American continent and elsewhere (Bjerknes, 1969; Wyrtki, 1975; Horel and Wallace, 1981; Trenberth et al., 1988).

In addition to the direct physical role the equatorial upper ocean plays in modulating global climate, through photosynthesis it also plays an essential role in the cycling of oxygen, carbon dioxide (CO_2), and other atmospheric constituents through the global system. In this manner, the upper ocean regulates the levels of greenhouse gases in the atmosphere, most notably CO_2, and hence global climate (Takahashi, 1989). In particular, upwelling of CO_2-rich subsurface waters make the equatorial Pacific the most important oceanic CO_2 source in the oceans (Takahashi et al., 1992). Although the source intensity of CO_2 in the equatorial Pacific seasonally varies a relatively minor amount (about 25%) during non-El Nino years, this source is eliminated by the blanketing effect

of warm, low-CO_2 surface water that spreads eastward from the western Pacific during El Nino warm events. Similarly, the upper equatorial Pacific constitutes an important link in the oceanic food chain. These pervasive influences provide the motivation for studying the upper equatorial Pacific Ocean (Kraus, 1977).

The ocean circulation is driven at the surface by wind stress and by buoyancy forcing due to heating, cooling, evaporation, and precipitation. This direct forcing by the wind stress and the buoyancy flux is generally absorbed within a surface layer that is often nearly homogeneous in temperature, salinity, and density due to turbulent mixing, and is therefore commonly referred to as the ocean surface mixed layer. The thickness of this mixed layer ranges from near zero during periods of light winds and strong heating to greater than a hundred meters under conditions of strong cooling and high winds. The direct effect of surface forcing is not always limited to the mixed layer, however, but sometimes extends into the density-stratified region below the mixed layer. This transition region of surface influence, in which surface layer turbulence provides the energy to entrain the stratified fluid below, is often referred to as the entrainment zone.

TROPIC HEAT experiment (Eriksen, 1985) microstructure measurements in the central equatorial Pacific in November 1984 and April 1987 showed a pronounced diurnal cycle in vertical turbulent mixing rate in both the surface mixed layer and in the stratified region below the mixed layer (Gregg et al., 1985; Moum and Caldwell, 1985; Moum et al., 1992a). Since the turbulent dissipation varied diurnally at depths significantly greater than the penetration of the surface well-mixed layer, turbulent mixing appears to have been caused by processes other than conventional mixed-layer physics (Moum and Caldwell, 1985; Moum et al., 1989; Peters et al., 1988). Since the only forcing having strong and persistent night-to-day differences was the solar insolation (Moum and Caldwell, 1985), the diurnal cycle in dissipation presumably must have been modulated by the diurnally-varying surface buoyancy flux.

Although the mechanisms responsible for the diurnal cycle of turbulent dissipation in the pycnocline remain uncertain, it has been suggested that internal gravity waves propagating downward from the base of the mixed layer to the highly sheared pycnocline might be responsible for the sporadic deep mixing (Gregg et al., 1985; Toole et al., 1987;

Peters et al., 1988; Dillon et al., 1989; Moum et al., 1989). Some of these investigations reported a diurnal cycle of high-frequency wavelike motions coincident with the diurnal cycle of dissipation (Moum et al., 1992b). According to this hypothesis, the internal waves provide the additional energy necessary to initiate dynamic instabilities and turbulent mixing. Recently, Wijesekera and Dillon (1991), McPhaden and Peters (1992), Moum et al. (1992a), and Hebert et al. (1992) have presented evidence from microstructure profilers, moored buoys, and towed thermistor chains that is consistent with this hypothesis. These studies present observations of a distinct, narrow frequency-band, and diurnally-varying signal in temperature records obtained in the low Richardson number shear flow above the Equatorial Undercurrent (EUC) core (Moum et al. 1992b). The moored buoy temperature records showed diurnally-varying high-frequency wavelike motions, possibly internal waves, where the measured frequency of 10-30 cph in the presence of the strong mean flow of the equatorial undercurrent (EUC) implied an intrinsic frequency near the buoyancy frequency of N = 5-7 cph (McPhaden and Peters, 1992). The zonal wavelength was approximately 150-250 m (Moum et al., 1992a,b). It is possible that the observed fluctuations represented a forced mode resulting from local shear instability of the mean flow or a combination of internal waves and shear instabilities.

Skyllingstad and Denbo (1994) used a two-dimensional, non-hydrostatic, large eddy simulation model to examine the hypothesized diurnal cycle of downward propagating internal waves in the central equatorial Pacific. Their model was initialized and forced with temperature, velocity, and wind observations from TROPIC HEAT. Their model results were consistent with the TROPIC HEAT microstructure observations and with the general hypothesis that internal waves, generated in or at the base of the diurnally-varying surface mixed layer, propagate downward into the stratified, high-shear flow above the EUC. A more thorough literature review of equatorial internal waves and turbulent mixing is presented in Chapter II.

The results from the TROPIC HEAT observations and numerical modeling studies to date have helped describe the diurnal cycle of turbulent mixing in the central equatorial Pacific at the times of those observations. Unfortunately, these observations are

temporally scarce, being limited to a few occasions of intense sampling over periods ranging from a few days to a few weeks. This scarcity of microstructure observations limits the ability to examine the diurnal cycle of internal waves and turbulent mixing under a more complete range of surface forcing and dynamic stability conditions. Both surface forcing and dynamic stability conditions in the central equatorial Pacific are known to vary on many different temporal scales, from diurnal to seasonal and interannual. Although the available observations have suggested possible relationships among the diurnal cycle of turbulent mixing in the stratified region and the local wind speed, wind direction, and vertical velocity shear in the water column (Moum et al., 1992a; McPhaden and Peters, 1992; Skyllingstad and Denbo, 1994), the short time span of the observations limits our ability to derive generalized relationships between forcing and internal mixing.

In addition to the scarcity of microstructure data, the TROPIC HEAT microstructure observations were limited in their vertical extent to the upper 120 m or so, roughly the depth of the EUC core. Although this depth range appears adequate to examine the directly forced mixed-layer processes and the entrainment zone between the mixed layer and the EUC core, it has not allowed adequate investigation of the vertical extent of the diurnal cycle of the internal wavefield. In particular, prior studies have not been able to determine whether or not these waves transport momentum and energy from the surface generation region through the EUC to the high shear flow beneath the core. The resolution of this issue is important to explain the equatorial momentum balance, which is discussed in further detail in Chapter II.

B. RESEARCH OBJECTIVES AND STRUCTURE OF DISSERTATION

This dissertation concerns the vertical extent and time variability of the diurnal cycle of high-frequency temperature fluctuations in the central equatorial Pacific. Unlike prior investigations that examined the diurnal cycle of turbulence and internal waves using a few short periods of high temporal and vertical resolution microstructure data, this study examines the response of the mixed layer and internal wave field to the time varying background conditions and forcing over a four-year period using moored buoy

data. Specifically, moored buoy data (McPhaden and Taft, 1988; McPhaden and Hayes, 1990) from 0°, 140°W for the period, November 1983 - October 1987, are utilized to investigate the diurnal cycle of the high-frequency temperature variability, as described by isotherm displacement variance (IDV), under varying surface forcing, stratification and velocity conditions. These observations of IDV could reflect high-frequency internal gravity waves, local shear instabilities, turbulence, or some combination of these processes. The magnitude of the IDV may be an effective measure of all of these processes, but it generally is not a means of distinguishing among them.

While the vertical range of data sets used in prior studies extended only to about 120 meters, the mooring data span from the surface to 300 meters, allowing a more complete examination of the vertical structure of the diurnally-varying high-frequency temperature fluctuations and the relationship between these wavelike motions and the EUC. Statistical relationships between the vertical structure of the diurnal cycle of high-frequency temperature variability and surface winds, the surface buoyancy flux, and the dynamic stability are found. Furthermore, the contribution of the diurnally varying high-frequency wavefield to the heat and momentum balances along the equator are discussed.

In Chapter II, a more complete review of the relevant literature concerning equatorial upper ocean dynamics is presented, with particular regard to high-frequency internal waves and turbulent mixing. Both analyses of observations and numerical modeling studies are reviewed. In Chapter III, the data sets are described and data processing methods are discussed. The procedures for computing IDV and the diurnal cycle of IDV are discussed. This is followed by a description of a sensitivity study to validate this procedure. In Chapter IV, the seasonal and interannual variability of the background oceanic and atmospheric conditions during the period of study are presented. In Chapter V, the seasonal and interannual variability of high-frequency IDV is discussed, and relationships between IDV and surface forcing, dynamic stability, and mixed-layer depth are examined. In Chapter VI, the focus is on the diurnal cycle of IDV. With only a few exceptions, it will be shown that the diurnal cycle of turbulence and internal waves, as indicated by IDV, was confined above the core of the EUC and usually above the 100 m depth. Relationships between the diurnal cycle of IDV and surface

forcing and dynamic stability parameters, as well as diurnal cycles of these parameters are discussed. This is followed by an examination of the relationships between the diurnal cycle of IDV and the mixed-layer depth and the diurnal range of the mixed-layer depth. The interpretation of IDV in terms of turbulence and high-frequency internal waves is further examined by investigating the diurnal variability of the wave momentum flux for the month of November 1984. The combined analyses suggest that IDV is related to turbulence or high-frequency internal waves transporting horizontal momentum from the surface layer to the stratified region, but not through the EUC core. The chapter concludes with a discussion of two additional possible sources of variability, mooring motion and gravitational tides, which are shown to be unlikely to generate the observed diurnal cycle of IDV. Chapter VII includes a discussion of the results, followed by the conclusions and recommendations for further investigation.

II. LITERATURE REVIEW

A. EQUATORIAL UPPER OCEAN DYNAMICS

The physical processes of the upper equatorial oceans are unique due to the presence of the large vertical shear associated with the EUC and the vanishing of the vertical component of planetary rotation. The westward trade winds along the equator result in upwelling of O(3 m day^{-1}) driven by Ekman divergence in the surface waters and geostrophic convergence deeper in the water column (Wyrtki, 1981; Halpern et al., 1989). This westward wind stress and strong upwelling produce a tongue of relatively cold surface water and a shallow main thermocline in the eastern equatorial Pacific and relatively warm surface water and a deep main thermocline in the western equatorial Pacific. This upwelling provides a source of cool water for the surface layer. The principal cause of changes in the depth of the equatorial thermocline is a horizontal redistribution of warm surface waters in response to the large-scale winds (Wyrtki, 1975; Merle, 1980; Duing and Leetmaa, 1980; Stevensen and Niiler, 1983; Molinari et al., 1985). Advection strongly influences SST, particularly in the eastern part of the basin. During El Nino, for example, the eastern tropical Pacific is warmed by the eastward advection of warm surface waters associated with the elevation of the thermocline in the west and its deepening in the east. This advective warming competes with cooling by upwelling. Since the mean vertical velocity component vanishes at the ocean surface, mixing processes determine the extent to which upwelling affects SST. Mixing processes also affect the intensity of the equatorial currents.

The steady-state zonal momentum budget at the equator includes the zonal convergence of zonal momentum, upwelling of eastward momentum, the zonal pressure gradient, the divergence of the mesoscale eddy flux, and the turbulent vertical stress (Bryden and Brady, 1985; Dillon et al., 1989),

$$\overline{U}\overline{U}_x + \overline{W}\overline{U}_z + \frac{1}{\rho}\overline{P}_x + (\overline{U'U'})_x + (\overline{U'V'})_y = -(\overline{U'W'})_z = \frac{1}{\rho}(\overline{\tau^x})_z \ , \qquad (1)$$

where $\overline{U}$ and $\overline{V}$ are mean zonal (positive eastward) and meridional (positive northward) velocities, $\overline{P}$ is mean pressure, ρ is density, $\overline{U'U'}$, $\overline{U'V'}$, and $\overline{U'W'}$ are the zonal, meridional, and vertical turbulent fluxes of zonal momentum, and τ^x is the zonal wind stress. Subscripts x, y, and z denote partial differentiation in the zonal (positive eastward), meridional (positive northward), and vertical (positive upward) directions . Analyses of observations (McPhaden and Taft, 1988) and diagnostic models (Bryden and Brady, 1985,1989) indicate that on annual time scales the principal zonal momentum balance in the equatorial upper ocean is between the vertically integrated zonal pressure gradient force and the wind stress, which is vertically distributed by turbulent mixing (Crawford and Osborn, 1981).

Examination of the terms in the vertically integrated zonal momentum equations indicates that the zonal pressure gradient is not balanced by the surface wind stress on shorter time scales (Dillon et al., 1989; Hebert et al., 1991). The strength of the wind plays a significant role in determining both the magnitude and, likely, the mechanisms of momentum transport between the surface and the core of the EUC. During low wind conditions the turbulent stress divergence was significantly different in magnitude and vertical structure from that found during strong winds (Hebert et al., 1991).

In November 1984, the measured turbulent stress divergence was too large above 40 m to balance the residual term in the zonal momentum budget of Bryden and Brady (1985,1989), and decayed exponentially with depth from the wind stress value at the surface. On the other hand, in April 1987 the turbulent stress divergence was smaller than that required by Bryden and Brady (1985,1989). Using data from the NORPAX Hawaii-to-Tahiti Shuttle Experiment, Johnson and Luther (1994) presented evidence for a rough zonal momentum balance at 90-117 m, even neglecting vertical stresses. Since their more directly measured estimate of the zonal momentum budget has a vertical structure in good agreement with the available, dissipation-derived estimates of turbulent vertical stresses,

they concluded that the suggestion of an imbalance in Bryden and Brady's momentum budget below the thermocline was probably erroneous. If the Johnson and Luther momentum budget is correct, the proposed requirement for vertically propagating waves to balance the budget (Dillon et al. 1989) is not necessary.

In general, momentum input by wind stress is vertically distributed by turbulent mixing. The depth of mixing is dependent on the static and dynamic stability of the water column. This vertical distribution of momentum in the upper ocean dictates which modes of equatorial Kelvin and Rossby waves are forced, and governs the response of the zonal pressure gradient and the EUC to changes in the wind stress (Schudlich, 1991). In summary, the vertical profile of wind stress in the equatorial ocean is an important, yet poorly understood, aspect of the large-scale equatorial circulation.

In the central equatorial Pacific, the South Equatorial Current (SEC) flows westward at speeds averaging about 0.3 ms^{-1}. On the equator, beneath the SEC, the eastward flowing EUC attains speeds as high as 1.5 ms^{-1}. Resultant vertical shear between the surface mixed layer and the EUC core often exceeds 0.02 s^{-1}, and is sufficiently strong to maintain a gradient Richardson number, Ri, of less than unity above the undercurrent core (Gregg et al., 1985; Chereskin et al., 1986; Moum et al., 1989), where $Ri=N^2/S^2$ (N is the local buoyancy frequency and S is the magnitude of the vertical shear of the horizontal current). Theoretical and laboratory research indicates that laminar flow becomes unstable to Kelvin-Helmholtz wave formation and the onset of turbulence when Ri is less than a critical Richardson number, Ri_c of 0.25. Once turbulent, however, the turbulence may continue until the Richardson number reaches a terminal value, Ri_t of about 1.0 (Stull, 1988). In addition to a low Ri, indicating dynamic instability, the onset of turbulence often requires some triggering energy (Stull, 1988). Thus, the low mean Ri observed in the high shear region below the equatorial mixed layer is on the margin of dynamic stability and subject to the onset of turbulence with the addition of additional kinetic energy.

The equatorial mixed layer system is a somewhat special case with regard to the oceanic planetary boundary layer (Garwood et al., 1989). In general, the Obukhov length

scale, $L = \frac{(\tau/\rho)^{3/2}}{B_0}$, is the limiting depth for oceanic mixed layers under the influence of wind stress, τ, and buoyancy flux B_0 (Obukhov, 1946). Complicating the equatorial mixed-layer system, upwelling may reduce the thickness of the surface layer to a fraction of the Obukhov length (Muller et al., 1984). While L is the limiting scale for the surface layer, Garwood et al. (1989) proposed that Rossby and Montgomery's (1935) neutral planetary boundary layer scale, u_*/f, where u_* is the friction velocity and f is the Coriolis parameter, may be an appropriate limit for the thickness of the entrainment zone, δ_{max}. Off the equator, δ_{max} is often a small fraction of the mixed-layer depth, and therefore has been approximated as a discontinuity in bulk models of the oceanic mixed-layer. If not for advection, the entrainment zone at the equator would thicken indefinitely. With typical mean upwelling conditions along the equator, Garwood et al. (1989) found an entrainment zone thickness of about 100 m under a shallow mixed layer, in good agreement with the deep diurnal cycle of turbulence observed during TROPIC HEAT.

The rate of turbulent kinetic energy dissipation and the vertical turbulent fluxes of heat, mass, and momentum are seldom measured directly but can be inferred from measurements of vertical temperature gradients and horizontal velocity. Early measurements, by means of free-falling instruments that were tracked very accurately, revealed that turbulent dissipation is higher near the equator than in extratropical latitudes. Dissipation is high even below the core of the EUC (Gregg, 1976; Gregg and Sanford, 1980; Gargett and Osborn, 1981), presumably a consequence of the large vertical shear. These early results were subsequently used to devise parameterizations for the turbulent mixing of momentum and heat in terms of Ri (Moum and Caldwell, 1985; Peters et al., 1987). When used in numerical models, these parameterizations lead to simulations that are more realistic than those with constant coefficients of eddy viscosity and diffusivity (Pacanowski and Philander, 1981). Although these parameterizations were significant improvements, they remain inadequate for satisfactory modeling of the tropical Pacific (Philander, 1990).

B. MICROSTRUCTURE OBSERVATIONS OF THE EQUATORIAL UPPER OCEAN

Microstructure observations in November 1984 near 0°, 140°W, as part of the TROPIC HEAT Experiment, revealed a large diurnal cycle in vertical turbulent mixing rates (quantified by the rate of viscous dissipation of turbulent kinetic energy) that was previously unknown at the equator (Gregg et al., 1985; Moum and Caldwell, 1985; Peters et al., 1988; Moum et al., 1989). During the day, when strong solar heating stabilized the upper 10-20 m, little turbulent dissipation was observed; what dissipation existed was limited to depths less than about 10 m. During the night, when surface cooling and wind mixing reduced the mixed-layer temperature, dissipation increased by two orders of magnitude, from 10^{-8} to 10^{-6} W kg^{-1}, indicative of vigorous mixing, down to depths of 80-90 m, more than twice the depth of the convectively active surface mixed layer, which reached to about 35 m at night. The enhanced dissipation at night typically occurred in bursts of turbulence lasting 2-3 hours. Peak dissipation rates in the pycnocline lagged those near the surface by several hours and were associated with individual turbulent overturns up to 10 m thick (Moum et al., 1989).

Observations of increased mixing in the surface layers of the ocean at night, when a loss of heat to the atmosphere destabilizes the upper ocean, have been made in many locations. What is unique about the measurements in the central equatorial Pacific is the intensity of the turbulence and its presence in the stratified region below the mixed layer. In contrast, observations from the upper ocean at mid latitudes show that values of dissipation associated with turbulent mixing penetrate only about 10 m below the mixed layer at night even when the mixed layer is very deep, O(100 m) (Shay and Gregg, 1986; Lombardo and Gregg, 1989; Price et al., 1986). Although the equatorial pycnocline was well stratified (N = 5-9 cph), the high vertical shear was sufficient to maintain Ri between 0.25 and 1.0, suggesting marginal dynamic stability, and a tendency toward the formation of turbulence. Interestingly, no similar diurnal cycle was apparent in the computed values of Ri (Chereskin et al., 1986). This suggests that the relationship between turbulent dissipation and local Ri may not be simple (Peters et al., 1988). It is possible, however, that an important diurnal variation in Ri might occur on vertical scales too short to be

resolved with the 10-12 m resolution of the TROPIC HEAT data. Preliminary analysis of more recent data from the Tropical Instability Wave Experiment (TIWE) in December 1991 suggest a possible diurnal cycle of Ri in the mixed layer (Lien et al., 1994); however, these data require further analysis.

C. EQUATORIAL INTERNAL WAVES

1. Observations

Although the physical mechanism for the diurnal cycle of turbulent dissipation in the pycnocline remains uncertain, several investigators have speculated that internal gravity waves might play an important role (Gregg et al., 1985; Peters et al., 1988; Dillon et al., 1989; Moum et al., 1989; Wijesekera and Dillon, 1991; McPhaden and Peters, 1992; and Moum et al., 1992a,b). The general hypothesis is that after sunset, high-frequency (near N) internal waves are generated just below the mixed layer as a result of turbulent convective overturns. These waves propagate downward, become unstable, and generate turbulent eddies above the undercurrent core at locations where Ri is reduced to subcritical values by superposition of wave and mean current velocities (Wijesekera and Dillon, 1991). Dillon et al. (1989) and Hebert et al. (1991) also suggested that internal waves were likely to be important in the large-scale zonal momentum balance of the pycnocline. Both of their turbulent stress divergence estimates were based on the assumption of an approximate local balance between production and dissipation of turbulent kinetic energy, neglecting buoyancy flux. They speculated that this local balance assumption might not be valid, because in addition to vertical diffusive fluxes caused by local shear instability, internal waves might play an important role in equatorial dynamics by the downward transport of zonal momentum. It remains unclear whether these internal waves, if generated, transfer momentum through the EUC into the deep ocean, or break and dissipate in the high shear region above the EUC core. Johnson and Luther (1994) indicated that although such mechanisms may occur, they are not necessary to achieve a zonal momentum balance on the equator.

In theoretical studies, Booker and Bretherton (1967), Bretherton (1966,1969), and Muller (1976) demonstrated the possibility of vertical transport of zonal

momentum by internal gravity waves. Boundary layer perturbations can generate internal waves that may transfer energy and momentum into the fluid interior, bypassing the usual turbulent-diffusion mechanism. Wijesekera and Dillon (1991) proposed two ways in which the eddies of a cooled boundary layer could result in the excitation of internal gravity waves in the underlying stable layer, thermal forcing and shear forcing (the obstacle effect). They concluded that in the central equatorial Pacific, shear forcing is more efficient, and therefore more likely. In a series of observational and numerical modeling studies of the atmospheric planetary boundary layer, Mason and Sykes (1982), Clark et al. (1986), Kuettner et al. (1987), and Huff and Clark (1989) found that boundary layer eddies are able to impinge upon the stratified layer above. In the presence of vertical shear, these eddies represent a localized form drag, or obstacle, to the overlying flow. These impinging eddies, or obstacles, then excite internal gravity waves (analogous to the generation of mountain lee waves). Similarly in the oceanic mixed layer, Wijesekera and Dillon (1991) hypothesize the generation of downward propagating internal gravity waves at the base of the mixed layer with a horizontal phase velocity equal to the average advection velocity of the mixed-layer eddies. Based on the average westward advection of the mixed layer during their November 1984 observation period, they concluded westward and downward propagating waves would be excited. McPhaden and Peters (1992) pointed out that for several months each boreal spring the near-surface flow is eastward (McPhaden and Taft, 1988), implying downward and eastward wave propagation during those periods. In either case, the mean vertical velocity structure associated with the EUC would suggest downward and westward wave momentum flux. The atmospheric studies showed that the horizontal length scales of the excited waves are several times larger than the height of the convective boundary layer, and that the waves tend to modify the boundary layer from which they were generated by some sort of feedback mechanism which is not yet understood (Clark et al., 1986).

Recently, several observational studies have supported the hypothesized role of internal waves in the turbulent energy balance of the pycnocline. Wijesekera and Dillon (1991) found a pronounced diurnal variation in both high-frequency isopycnal displacement variance and turbulent kinetic energy dissipation rate. Their isopycnal

displacement variance values were computed as the root mean square (rms) vertical displacement from a Thorpe-reordered stable density profile (additional discussion on this computation is provided in Chapter III) (Thorpe, 1977). The vertical correlation of isopycnal displacement variance indicated vertical length scales of the wave field greater than 100 m. They found significant correlation at a 0.1-day lag between internal wave displacement variance and turbulence, as inferred from calculations of the available potential energy of fluctuations (APEF):

$$APEF \approx \frac{1}{2M}\sum_{i=1}^{M} d'(\frac{\rho'}{\rho_0})g \approx \frac{1}{2}N^2L_T^2 \qquad m^2s^{-2} \qquad (2a)$$

$$L_T=[\frac{1}{M}\sum_{i=1}^{M} d'^2\ ]\ , \qquad (2b)$$

where d', ρ', ρ_0, and g are the Thorpe displacement, the density fluctuation between stable (reordered) and unstable (observed) density profiles, mean density ($\approx$1000 kg m^{-3}), and the acceleration of gravity ($\approx$9.8 m s^{-2}), respectively. APEF is a measure of the maximum potential energy that can be released by a turbulent overturn (Dillon and Park, 1987). From this 0.1-day lagged correlation, they surmised that the observed nighttime mixing in the pycnocline could be a result of instability of the high-frequency internal waves, which are initiated a few hours prior to the intense turbulent mixing. Using TROPIC HEAT 2 data, Moum et al. (1992a) found high correlations between turbulent dissipation (from continuous microstructure profiles) and high-frequency internal gravity waves (from towed thermistor chain data) along the equator from 140°W to 110° W in April 1987. During the first 4 days of their record, patches of high-frequency signal appeared intermittently and were concentrated in the period following sunset until several hours past sunrise. The duration of the patches was several minutes to many hours, corresponding to several hundreds of meters to several tens of kilometers in the zonal direction. The spectrum of isopycnal displacement variance was dominated by a narrow band of frequencies between 18-36 cph (corresponding to 150-250 m zonal wavelength) of internal waves. Both turbulence and internal waves varied diurnally. By the fifth day, the high-frequency component of the temperature variance was weak, and for the

remaining 10 days there was little or no high-frequency signal in the record. Moum et al. (1992a) attributed the difference between the first 4 days and the remainder of the period to a drop in the wind speed.

McPhaden and Peters (1992) analyzed data from a vertical array of fast sampling (1 minute) temperature recorders near the surface on a mooring at 0°, 140°W in May-June 1987. Their analyses indicated the existence of a diurnal cycle in IDV that was most pronounced at frequencies of 10-30 cph, and that was coherent over the 31 m vertical extent of the array between 30 m and 61 m. They estimated a nighttime isotherm displacement amplitude of 0.5-2 m, and that zonal wavelengths were roughly 100-300 m, consistent with towed thermistor chain data of Moum et al. (1992a). They speculated that the observed diurnal cycle was due to a combination of internal waves remotely generated at the base of the nighttime mixed layer and local shear instability of the large-scale flow. They showed that the appearance of internal waves in the pycnocline at frequencies higher than the local buoyancy frequency (4-8 cph) could be attributed to Doppler shifting by the EUC. In addition to their analysis of fast sampling temperature recorders for May-June 1987, McPhaden and Peters (1992) examined more coarsely resolved 15-minute temperature time series for November 1984, April 1987, and May-June 1987. When averaged over 30 days, these data also indicated the presence of a diurnal cycle in the higher frequencies. A comparison of the diurnal range in IDV for these three periods led them to suggest that the magnitude of the diurnal cycle may be related to the strength of the wind forcing and intensity of the vertical shear.

There is evidence indicating that the November 1984 and April 1987 turbulent dissipation data at 0°, 140°W are not representative of mixing across the entire equatorial Pacific, but merely represent mixing resulting from the conditions at that location at those times. In results from the WEC88 cruise along 150°W in February and March 1988, Carr et al. (1992) noted an absence of a clear diurnal signal of dissipation. With low wind speed, high incoming irradiance, low sea surface temperature, and a shallower EUC, environmental conditions were notably different from those during TROPIC HEAT 1. Similarly, the TROPIC HEAT 2 results found diurnal variability of high-frequency temperature signals during the first 4 or 5 days (nearer 140°W) and little

or no high-frequency signal for the remainder of the experiment's 14 days as the vessel moved eastward toward 110°W (Moum et al., 1992a). In the data collected to date, pronounced diurnal variability of turbulent dissipation in the pycnocline has been observed only at or near 0°, 140°W, and only during periods of moderate or strong westward winds.

2. Linear Wave Theory

This dissertation focuses on the diurnal cycle of high-frequency (near N) isotherm displacement variance at 0°, 140°W. Although the wavelike phenomena measured by IDV may be non-linear, the detailed structure is not adequately resolved to determine the degree of non-linearity, and a linear analysis is undertaken to provide insight into the behavior of small-amplitude wavelike fluctuations in this domain. Preliminary to the following statistical analysis, this section provides a brief review of linear internal wave theory in an equatorial ocean, as applicable to the diurnal cycle of the internal waves.

Following Boyd (1989), the equations for the vertical structure of linear internal waves in mean shear flows are derived. Starting with the linearized set of Boussinesq equations in non-rotating coordinates with mean flow $U = U(z)$ in the x-direction, the governing equations are:

$$D_t u + w u_z = -p_x \tag{3a}$$

$$D_t v = -p_y \tag{3b}$$

$$D_t w + b = -p_z \tag{3c}$$

$$D_t b - w N^2 = 0 \tag{3d}$$

$$u_x + v_y + w_z = 0, \tag{3e}$$

in which $b = g\rho\rho_o^{-1}$ is the buoyancy perturbation with perturbation density ρ, and p is the perturbation pressure divided by the mean density. The perturbation velocities are $\mathbf{u} = (u,v,w)$ in Cartesian coordinates, with u eastward. $D_t = \partial_t + U\partial_x$ incorporates advection by the mean zonal flow. Subscripts x, y, z, and t denote differentiation. Assuming negligible north-south variation of the mean fields and a meridional wavelength much less than 500 km, the mean shear flow can be considered to be horizontally invariant. For plane waves, these simplifications lead to a vertical structure equation (Boyd et al., 1993):

$$G_{zz}(z) + m^2 G(z) = 0, \tag{4}$$

where m is the local vertical wavenumber, given by

$$m^2 = K^2 \frac{(N^2-\sigma^2)}{\sigma^2} + \frac{kU_{zz}}{\sigma} , \tag{5}$$

and σ is the intrinsic frequency, i.e. the frequency measured by an observer moving at the local mean speed U, and $\mathbf{K} = (k,l,0) = (K\cos\theta, K\sin\theta, 0)$ is the horizontal wavenumber. When $m^2 > 0$, the solutions $G(z)$ are locally oscillatory, and when $m^2 < 0$, they are exponential. Equations (4) and (5) plus boundary conditions completely specify the wave solutions to (3a-e) when both $N(z)$ and $U(z)$ are specified. This dispersion relation is shown to be singular at the critical depths, at which the intrinsic frequency vanishes, $\sigma = \omega(1-U\cos\theta/c) = 0$. Although it might not be applicable to the low Ri shear flow at the equator, Booker and Bretherton (1967) have shown that vertically propagating waves are strongly attenuated in passing through the critical layer, provided $Ri >> 0.25$.

Following Boyd (1989), the polarization relations for the remaining fluctuation variables are determined:

$$\begin{bmatrix} u \\ v \\ p \\ w \end{bmatrix}(x,z,t) = \begin{bmatrix} -i\frac{l^2 U_z}{K^2\sigma} & i\frac{k}{K^2} \\ i\frac{klU_z}{K^2\sigma} & i\frac{k}{K^2} \\ i\frac{kU_z}{K^2} & i\frac{\sigma}{K^2} \\ 1 & 0 \end{bmatrix} \begin{bmatrix} G(z) \\ G_z(z) \end{bmatrix} e^{i(\mathbf{K}\cdot\mathbf{x}-\omega t)} . \tag{6}$$

The polarization equations relate the fluctuation variables u, v, w, and p to the vertical structure solution $G(z)$.

3. Spectral Models

A kinematic description of oceanic internal waves is usually based on the hypothesis that the wave field is composed of a random superposition of linear waves. The Garrett and Munk (GM) spectral model has become a standard description for deep ocean internal waves (Garrett and Munk, 1972,1975; Munk, 1981). The GM model was empirically derived from observations of one-dimensional spectra of frequency from moored current meters and horizontal wavenumber from towed thermistors. The GM

formulation is based on an infinite ocean having no top or bottom boundaries and a slowly varying buoyancy frequency profile, $N(z)$, compared with the fluctuations of the waves. This permits the vertical variation of wave amplitude and vertical wavelength to be scaled by $N(z)$ using the WKB approximation. In the upper ocean, say from the surface to 200 m, the GM model is expected to have limited application due to large changes in buoyancy frequency with depth and the reflection of waves from the surface boundary (Levine, 1987). Despite these limitations, the GM spectrum has been compared with upper ocean measurements made by acoustic doppler profilers, moored current meters, thermistor chains, and CTD profiles (Pinkel, 1975, 1981, 1984; Kase and Siedler, 1980; Levine et al., 1983a,b; McPhaden, 1985; Chereskin et al., 1986). These comparisons indicate that while some aspects of the GM spectrum are consistent with the data, many are not.

Studies have suggested that space and time variability in the equatorial ocean may be substantially different from variability at mid latitudes (Wunsch and Webb, 1979; Eriksen, 1980; Toole and Hayes, 1984; McPhaden, 1985). In comparing the high-frequency variability of equatorial TROPIC HEAT microstructure data with that observed at other latitudes in terms of the GM model, Chereskin et al., (1986) found that contemporaneous isopycnal displacement and velocity spectra yielded spectral energy levels which differed by a factor of 4. They found that this difference could be accounted for by vertical advection by the waves of the background shear flow. They also found that the GM spectral energy level estimated from vertical displacement was similar to the spectral energy level for many of the observations from which Levine et al. (1985) had removed the scaling of the GM model.

Boyd (1989) and Boyd et al. (1993) used TROPIC HEAT observations and a simple spectral model to characterize the high-frequency internal wavefield in the strongly sheared upper equatorial Pacific. Their observations consisted of temperature and velocity data from four moorings spanning the equator between 1.5°N to 3°S along 140°W for the period November 1984 to June 1985. In these papers, they compare their observations and model output to the GM model spectrum. The GM model spectrum is based on the following assumptions which are questionable in the central equatorial

Pacific: i) the no-mean-flow linear internal wave dispersion relation is valid, ii) the internal wavefield is vertically symmetric (same amount of energy propagates up and down) and horizontally isotropic, iii) the internal wave energy spectrum is separable into a function of frequency times a function of wavenumber, where the function of frequency is independent of wavenumber and the function of wavenumber is independent of frequency except for a bandwidth scale factor.

Following Boyd et al. (1993), several of the GM model assumptions are expected to be violated in the strongly sheared upper ocean zonal mean flows at the equator along 140°W, including the following: i) the linear dispersion relation will be modified by the vertical curvature of the mean flow and by Doppler shifting in the intrinsic frequency; ii) the mean zonal currents may impose directional asymmetry on the energy spectrum through critical layers involving zonally propagating waves; and iii) in the neighborhood of the ocean surface, a fixed phase relationship between upward and downward propagating components is expected. In addition to these violations of the GM assumptions, the fact that linear internal waves advect the mean flow readily leads to the expectation that many of the observed statistics will differ significantly from the canonical GM model. The fit to coherence of velocity components at vertical separations is not good (Boyd, 1989). Vertical advection, which is not included into the GM model, has been held responsible for the small vertical coherence length scale and the observed decrease in that length scale with increasing frequency (Muller et al., 1978).

D. REVIEW OF EQUATORIAL MODELING STUDIES

Several modeling studies during the past two decades have illustrated the role of the upper ocean mixed layer in the equatorial circulation (Hughes, 1980; Schopf and Cane, 1983; Garwood et al. 1989; Schudlich and Price, 1992). In one of the first models designed to explain tropical and equatorial mixed layers, Hughes (1980) predicted a simple balance between local wind and heating, modified by upwelling, resulting in a mixed-layer depth equivalent to the Obukhov length scale. This simple 1-1/2 layer model did not include an undercurrent and therefore no horizontal advection, and was limited by a simple parameterization of entrainment into a quiescent lower layer. More realistic

primitive equation models of the large-scale equatorial circulation, with Ri-dependent mixing, showed that without a mean surface heating, the EUC is eliminated by a westward wind stress in a manner of days (Pacanowski and Philander, 1981). This result was similarly found by Schopf and Cane (1983).

The role of diurnal variations in surface heating was explored by Kraus (1987). He used a mixed-layer model that parameterizes local vertical fluxes of energy and momentum by the transilient method of Stull and Kraus (1987). This method involves a spectrum of differently sized eddies. Kraus (1987) included a representation of the mean EUC and showed that turbulent mixing occurs well below the mixed layer at the equator. Garwood et al. (1989) and Schudlich and Price (1992) used one-dimensional models initialized with realistic stratification and shear of the EUC to simulate the diurnal cycle of dissipation observed during TROPIC HEAT. Garwood et al. (1989), using typical central equatorial Pacific forcing, found that instabilities initiated just below the surface layer ripple down into the water column and reach their deepest extent of about 90 m only after many hours. Their experiments suggested that Ri alone is a poor predictor of the rate of turbulent mixing in the pycnocline. Schudlich and Price (1992) showed that while the daytime phase appears unaffected by the EUC, the nighttime phase of the diurnal cycle is strongly affected by the EUC. The diurnal cycle in their model was relatively insensitive to other equatorial ocean features, such as the zonal pressure gradient and upwelling. Although neither of these models included internal gravity waves and both simulated a diurnal cycle in dissipation, Schudlich and Price (1992) showed that the models do not simulate the observed intermittence of the dissipation on hourly time scales. They suggested that this might be due to the exclusion of internal waves that may trigger local shear instabilities.

Using a two-dimensional, non-hydrostatic, large-eddy simulation model, Skyllingstad and Denbo (1994) performed several experiments to investigate the formation and maintenance of high-frequency internal waves in the central equatorial Pacific. In their numerical experiments, internal waves were generated in the surface mixed layer by a type of Kelvin-Helmholtz instability that is dependent on both the flow Reynolds number and Richardson number. It would appear that Reynolds number in the central

equatorial Pacific is always greater than their computed critical Reynolds number, and therefore not important as a predictor of instability in this region. Internal waves amplified when Ri was less than 0.05 and decayed when Ri exceeded 0.05. Their model results showed that the diurnal heating cycle drives a diurnal variation in the mixed-layer Ri value, which tends to modulate diurnally the generation of the internal waves with a maximum intensity just before sunrise. The modeled sensitivity of internal wave formation to the surface wind stress direction could also be explained in terms of reduced mixed-layer shear. In their simulations, easterly winds promoted strong mixed-layer current shear, low Ri and a strong diurnal cycle of internal waves, while westerly winds led to weak shear in the mixed layer, higher Ri, and reduced internal wave activity. Additionally, Skyllingstad and Denbo (1994) found that the wave momentum flux was comparable to bulk estimates of large-scale fluxes given in Hebert et al. (1991) and Dillon et al. (1989), indicating that internal waves can be a significant process in the zonal momentum budget of the equatorial currents. In the surface mixed layer, the internal waves gained eastward momentum at the expense of the background flow. In some cases, this momentum was transferred back to the mean flow at a critical level resulting in a deceleration below the undercurrent core. Otherwise, the waves tended to decrease the current velocity above the undercurrent core.

III. DATA AND METHODS

A. DATA DESCRIPTION

1. EPOCS/TOGA TAO Mooring Data

The data used in this dissertation consist primarily of time-series measurements from taut-wire surface moorings located at 0°, 140°W in 4300 m of water for the period from November 1983 through October 1987. Mooring deployments and recoveries were made at roughly six-month intervals. These moorings were deployed as part of the National Oceanic and Atmospheric Administration's (NOAA) Equatorial Pacific Ocean Climate Studies (EPOCS) Program and later the Tropical Ocean-Global Atmosphere (TOGA) Program's Tropical Atmosphere Ocean Array (TOGA TAO).

These moorings were instrumented with Yellow Springs Instrument air and sea surface temperature sensors at nominal heights/depths of 3 m above the sea surface and 1 m below the sea surface, respectively, seven EG&G model 610 Vector Averaging Current Meters (VACMs) and six Sea Data Temperature Recorders (TRs) in the upper 300 m, and Vector Averaging Wind Recorders (VAWRs) at a height of 4 m above the mean water line. Several EG&G Model 630 Vector Measuring Current Meters (VMCMs) were also used. The VACMs recorded 15-minute averaged velocities and temperatures and the TRs recorded 15-minute spot samples of temperature. The VAWR is an inverted VACM equipped with a Climet three-cup anemometer and a pivoted vane (Freitag et al., 1989). There have been some changes in subsurface instrument depths during the 4 year period of this investigation due to changing program priorities. Figure 3.1 illustrates a typical mooring arrangement. Tables 3.1 and 3.2 provide actual time lines for instruments at each of the depths used in this analysis for temperature and velocity, respectively. There are gaps in some of the time series due to occasional instrument failures. Further information on the collection and initial processing of these data is available in Freitag et al. (1987), Freitag and McPhaden (1988), and Yue et al. (1991). Monthly means and seasonal cycles of each of these time series measurements for the period 1983-1991 are available in McPhaden and McCarty (1992).

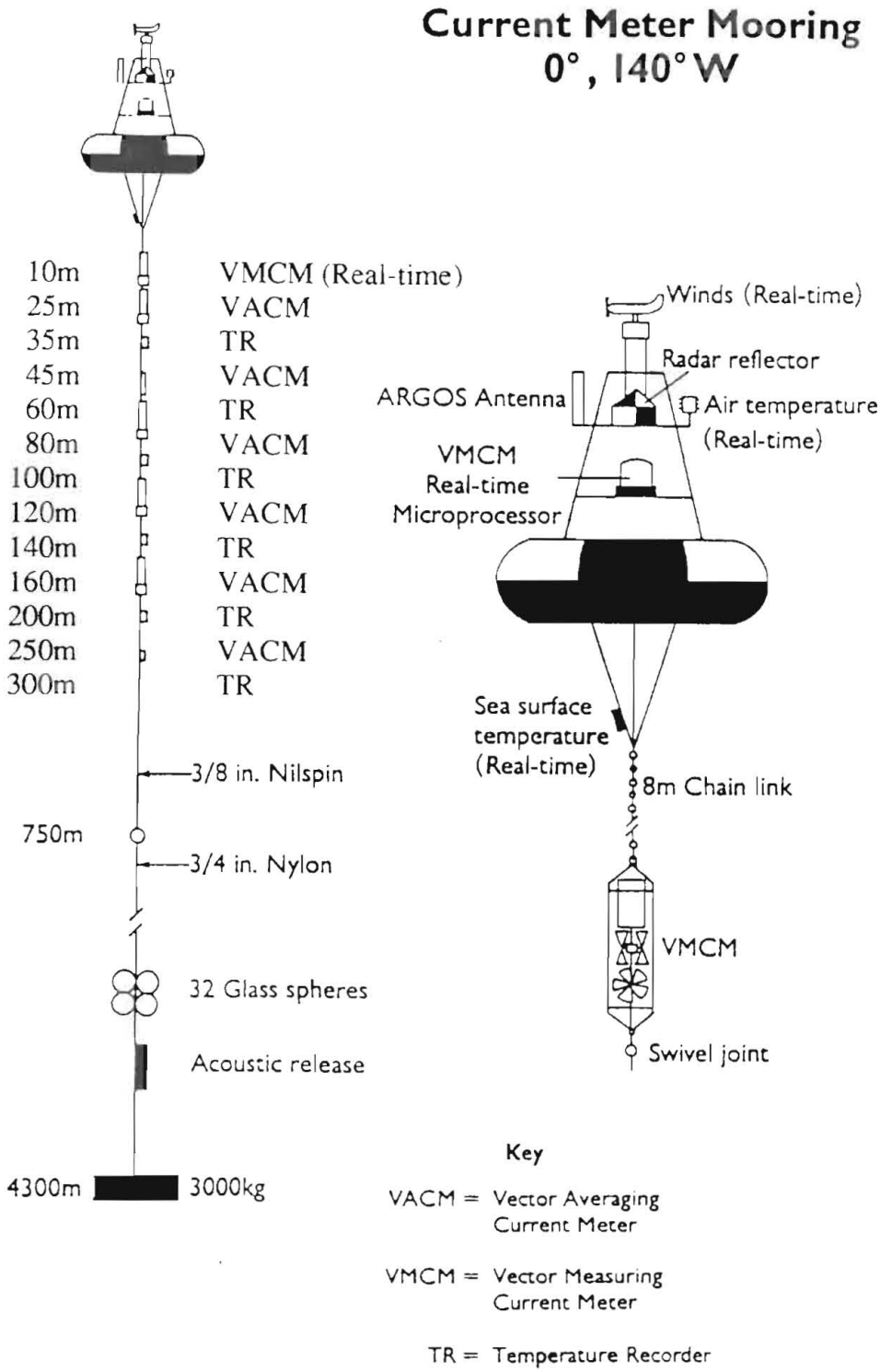

Figure 3.1. Schematic of typical moored buoy at 0°, 140°W during the period November 1983 -October 1987.

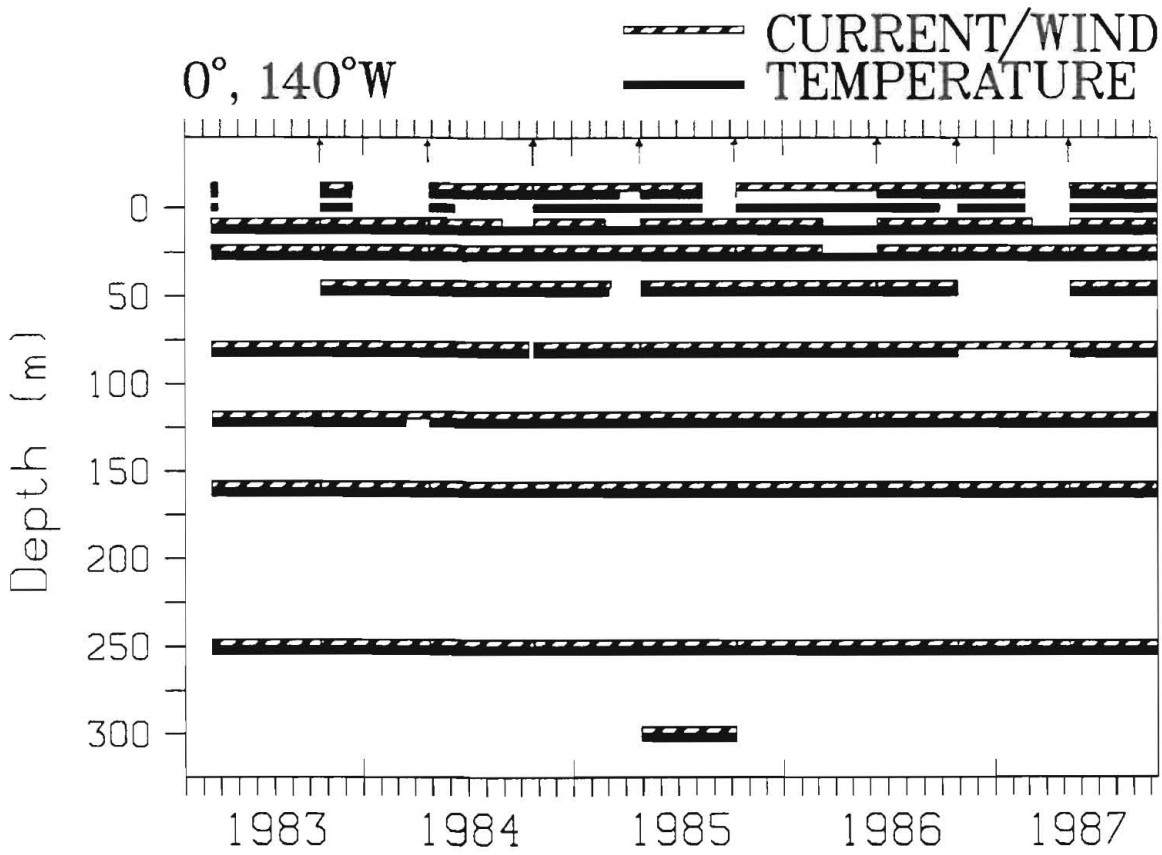

Table 3.1. Bar chart showing velocity and temperature data available from current meters and from wind recorders as a function of depth at 0°, 140°W during the period 1983-1987. Arrows indicate times of mooring deployments and recoveries and times when CTD casts were conducted.

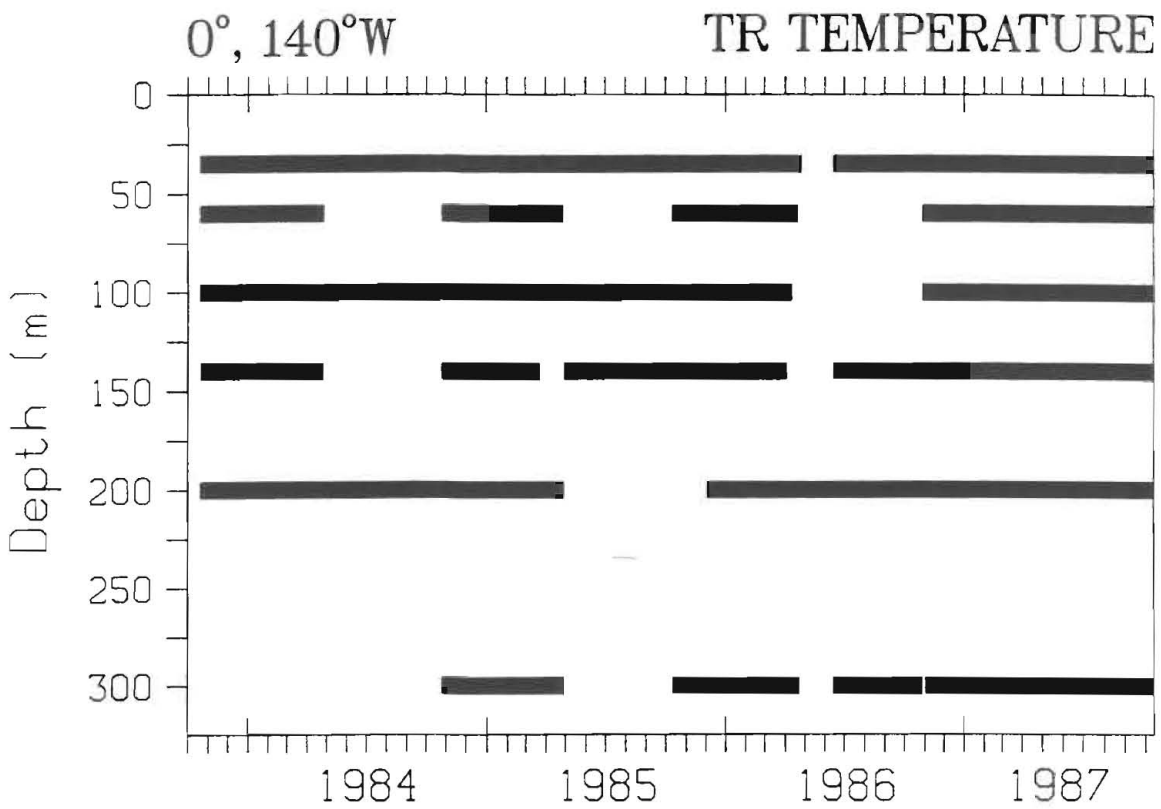

Table 3.2. Bar chart showing availability of data from temperature recorders (TRs) at 0°, 140°W during the period 1983-1987.

In addition to these standard equatorial mooring measurements, two of the moorings were instrumented with a vertical array of fast-sampling 1-minute TRs designed to resolve high-frequency internal wave variations. The duration of these data are typically days to weeks. The first, in May-June 1987, had fast-sampling TRs at 30 m, 34 m, 36 m, 40 m, 46 m, 59 m, 61 m, and 101 m. Processing of these data is summarized in Freitag and McPhaden (1988). Using this data, McPhaden and Peters (1992) reported a diurnal cycle in IDV that was most pronounced at frequencies of 10-30 cph that was coherent between 30 m and 61 m. The second mooring was equipped with fast-sampling TRs at 17 m, 24 m, 30 m, 36 m, 47 m, 59 m, 70 m, 82 m, 101 m, 121 m, 160 m, 199 m, and 250 m, an acoustic Doppler current profiler (ADCP) with 8 m vertical resolution between 10-250 m, and a shortwave radiometer. This unique 30 day data set was obtained in conjunction with microstructure measurements of the Tropical Instability Wave Experiment (TIWE) conducted in November/December 1991. Although this dissertation is not directly concerned with the analysis of this second fast-sampling data set, some of the results of that analysis are discussed here to assist in the analysis of the 15-minute time series data.

2. Climatological Data

In addition to using the moored buoy data to characterize the high-frequency temperature variability, several climatological data sets are utilized to provide additional information about surface forcing parameters. The International Satellite Cloud Climatology Project (ISCCP) data were used to compute monthly mean surface irradiance values for 0°, 140°W for the 4-year observation period. ISCCP data were also used to compute monthly mean estimates of surface out-going longwave radiation. The ISCCP data contains information on cloud cover, cloud type, and cloud heights, as well as information about some of the atmospheric composition and surface conditions (Rossow et al., 1988; Rossow and Schiffer, 1991). These data are resolved globally at 2.5° x 2.5° resolution every three hours. The Comprehensive Ocean-Atmosphere Data Set (COADS), Esbensen and Kushnir (1981), Oberhuber (1988), Dorman and Bourke (1976), and Global Precipitation Climatology Project (GPCP) climatologies were also used to compute surfaces fluxes.

B. DATA PROCESSING

Preliminary post-processing of the raw mooring data was performed at NOAA's Pacific Marine Environmental Laboratory following Freitag et al. (1991). This included converting the data to engineering units using empirically-derived calibration coefficients and performing internal quality checks and windowing to remove obviously bad data points. Since this investigation focuses on high-frequency variations, the resulting 15-minute data were visually examined to further verify the quality. Questionable data were eliminated and flagged.

With the objective of characterizing the diurnal cycle of high-frequency temperature variability over seasonal and interannual time scales, subsurface temperature and velocity data over the 4-year period from November 1983 through October 1987 were examined. To investigate the variability of the diurnal cycle over these longer time scales, the data were segmented by calendar month and then into six-hour time bins. The local time bins, 2200-0400 (night), 0400-1000 (morning), 1000-1600 (day), and 1600-2200 (evening), were selected to correspond with observations of the diurnal cycle of turbulent dissipation, and to the observations by McPhaden and Peters (1992) of the diurnal cycle of high-frequency internal waves. The TROPIC HEAT observations showed maximum rates of turbulent dissipation and high-frequency internal wave activity in the stratified region during the morning hours near sunrise, corresponding to the 0400-1000 time bin in this study. Minimum values of dissipation typically occurred during the evening, or the 1600-2200 time bin. In discussing diurnal variations, the first two time bins (night and morning) will be collectively referred to as nighttime and the remaining two time bins (day and evening) will be collectively referred to as daytime.

In addition to allowing a comparison of different six-hour bins, and thus an indication of the mean diurnal cycle, segmenting the data into six-hour segments effectively acts as a high-pass filter to reduce the effects of the semi-diurnal and diurnal tides. Additional measures taken in computing IDV to filter the tides are discussed in greater detail in the next section.

In examining statistical relationships throughout this analysis, the standard error of the mean and 95% confidence intervals are often used as indicators of the level of

statistical significance. The standard error of the mean was computed as $\frac{\sigma}{\sqrt{n-1}}$,

where σ is the standard deviation of the population of n observations (Crowe et al., 1960). The 95% confidence intervals were computed based on the integral times scale between of the respective time series using the method of Davis (1976). The integral time scale: $\tau_n = \sum_{i=-\infty}^{\infty} C_0(i\Delta t)C_n(i\Delta t)\Delta t$, determines the time period required to gain a new "degree of freedom" in computing correlations. The use of the integral time scale in determining significance levels is particularly important due to the strong seasonal cycles of the surface forcing and background conditions observed in the equatorial Pacific Ocean.

1. Isotherm Displacement Variance

As an indicator of the seasonal and interannual variability of the high-frequency temperature variability, monthly mean values of IDV were computed for the 48 months of the record. IDV was computed at each of six depths instrumented with 15-minute spot-sampled temperature recorders (TRs); 35 m, 60 m, 100 m, 140 m, 200 m, and 300 m. Although temperatures were recorded at 15-minute intervals at the each of the VACM depths, 1 m, 10 m, 25 m, 45 m, 80 m, 120 m, 160 m, 250 m, these temperature values represented 15-minute averaged temperature, rather than instantaneous temperature. The 15-minute averaging operator effectively removed the higher-frequency waves of interest here. It is important that even the 15-minute spot-sampled TR data, with a Nyquist frequency of 2 cph, is too coarse to resolve the high-frequency internal waves (10-30 cph) observed by McPhaden and Peters (1992) using 1-minute spot-sampled TR data. Nevertheless, with sufficient averaging, over about 30 days, McPhaden and Peters (1992) reported a diurnal cycle of IDV using 15-minute TR data.

Prior to computing variances for each of the six-hour records, each six-hour segment was fitted to a cubic polynomial to remove the mean, trend and curvature of the temperature signal. The purpose of this operation was to remove the lower frequencies, particularly the tidal frequencies. Figure 3.2 illustrates the simple method used to remove the dominant tidal effects. The advantages of this method are that it is simple and local

because it was applied only to six-hour segments; hence, non-stationarity of the data does not present a serious problem. Similar analyses using a 32-term tidal harmonic analysis routine and an ideal (cosine taper) high-pass filter to the monthly data sets resulted in undesirable effects that were attributed to the non-stationarity of the data over monthly time scales. An examination of the four-year records of raw temperature and velocity data clearly shows the non-stationary character of the data.

After fitting with cubic polynomials, variances of the residuals were computed for each six-hour segment for each day of each month for all six TR depths. IDV was then computed by normalizing these variances by the mean temperature gradient for the same six-hour period. The mean temperature gradient, $\partial T/\partial z$, was computed from the six-hour mean temperatures at each depth using centered differencing, except at the surface and at 300 m, where first differences were used. A sensitivity study was performed to evaluate the differences between normalizing by the mean $\partial T/\partial z$ for the six-hour segment averaged over the typical 30-day month (which was more stable, but subject to non-stationarity errors) or normalizing by the mean $\partial T/\partial z$ for the individual six-hour segments, subject to noise due to small instrumental errors. The results showed that the possible error due to instrument error was much less than that due to non-stationarity of the gradient over 30 days (Figure 3.3). Thus, if a computed gradient was less than the minimum resolvable gradient computed assuming a maximum instrument error of 0.05 C, then that observation was not used in computing IDV. The minimum resolvable gradient, *graderr* was computed as $\textit{graderr} = \frac{0.05^{o}C\sqrt{2}}{\Delta z}$, where Δz is the instrument spacing. To greatly improve the high-frequency signal-to-noise ratio, the six-hourly IDV's for each of the four time bins were ensemble-averaged over all days of each month.

Since IDV was computed by dividing the six-hour temperature variance by the six-hour mean vertical temperature gradient, this calculation was extremely sensitive to small temperature gradients, such as those occurring in the surface mixed-layer. Therefore, it was important to distinguish between periods when the instruments were in the mixed layer and periods when the instruments were below the mixed layer. When the 35 m and 60 m TRs were in the mixed-layer, gradients were small and IDV would be

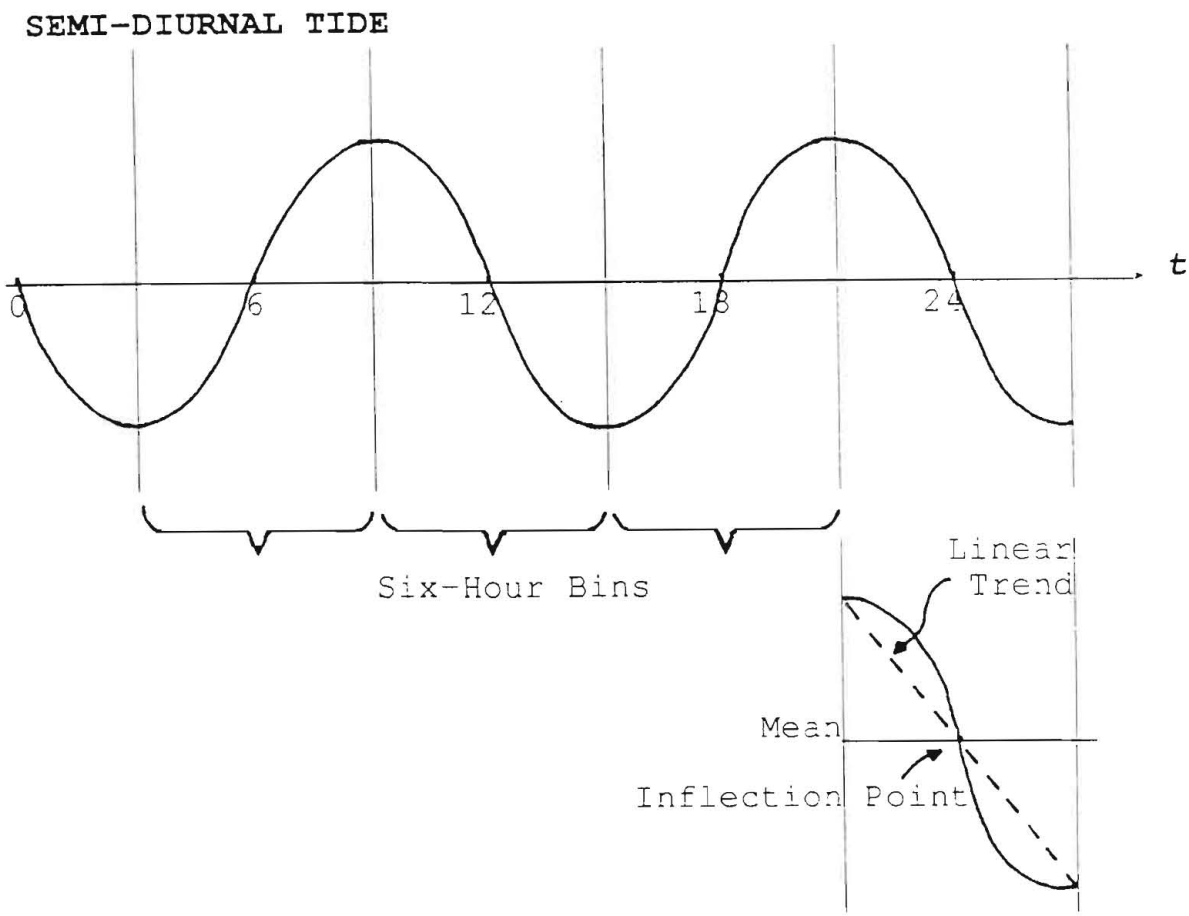

Figure 3.2. Illustration of procedure used to high-pass filter the temperature data to reduce principal tidal constituents. Data were segmented into six-hour time bins and fit with a cubic polynomial. Illustration shows that the polynomial removes the local mean, six-hour trend, and the curvature and inflection point associated with the semi-diurnal tide.

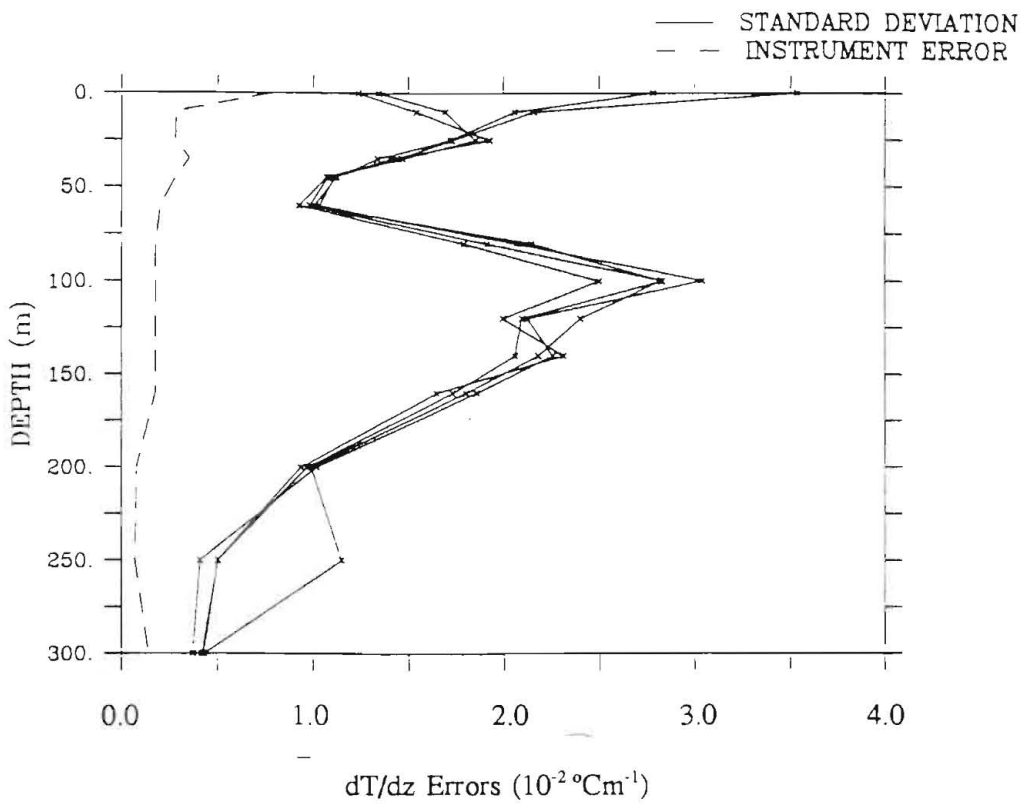

Temperature Gradient Error at 0°,140°W (Nov 84)

Figure 3.3. Temperature gradient error analysis used to determine the preferred temperature gradient (dT/dz), which was used to normalize temperature variances in computing isotherm displacement variance (IDV). The dashed line represents the maximum error in dT/dz associated with the instrument errors. Maximum instrument errors were assumed to be 0.05 C. The four solid lines are standard deviations of dT/dz over the month of November 1984. These results show that the non-stationarity of dT/dz over the month is greater than the possible error in dT/dz due to instrument error.

expected to become large and meaningless. Eliminating six-hourly segments having vertical temperature gradients less than 0.004 Cm^{-1} at 35 m and 0.002 Cm^{-1} at 60 m served to filter out time periods when the TRs were in the mixed-layer. In addition to the temperature gradient tests, six-hourly values of IDV were subjectively edited to remove unrealistically high IDV values before computing monthly means. Over the four-year record, six-hourly values of IDV at 35 m were eliminated by these two tests 14.7%, 15.1%, 15.1%, and 9.9% of the time for the night, morning, day, and evening time bins, respectively. Six-hourly values of IDV at 60 m were eliminated 4.1%, 2.9%, 2.6%, and 2.6% of the time for the night, morning, day, and evening time bins, respectively.

2. Buoyancy Frequency

The static and dynamic stability of the upper ocean, as well as the corresponding generation and decay of internal waves and turbulent mixing are fundamentally related to the density stratification of the water column. Therefore, estimates of the buoyancy frequency,

$$N = \left(\frac{-g}{\rho_o}\frac{\partial \rho}{\partial z}\right)^{1/2} ,$$

were computed for the 48-month analysis period. The lack of a moored salinity time series at 0°,140°W precluded the inclusion of high-frequency salinity fluctuations in the computation of N. Conductivity, temperature, and depth casts (CTDs) were conducted at about six-month intervals during each mooring deployment and recovery (Table 3.1). Examination of the salinity profiles from these CTD casts suggests that although salinity does change with time, particularly during the migration of a salinity front during the passage of tropical instability waves, the vertical gradient of salinity appears to be relatively constant compared with changes in vertical temperature gradients. Using the available salinity profiles, estimates of monthly salinity profiles were computed by linear interpolation. Actual monthly salinities may have varied substantially from these estimates. In addition to these monthly salinity profile estimates, six-hourly mean temperature profiles were computed using both VACM and TR temperatures at 14 depths. Using the monthly salinity values and the six-hourly mean temperature values, six-hourly

mean densities were computed at each of the 14 depths. These density profiles were then fit with a cubic spline (Akima, 1970) designed so that the shape of the curve matches the shape of the data while minimizing oscillations. The vertical density gradient, $\partial\rho/\partial z$, was computed from the spline fit of the density profile. In this manner, N was computed at each of the 14 instrument depths for each six-hour period.

3. Velocity Shear

Dynamic stability is determined in part by the velocity structure of the water column, particularly the vertical velocity shear. Therefore, six-hourly values of vertical velocity shear were computed from six-hourly mean velocity profiles computed from the 15-minute averaged VACM velocity data at 10 m, 25 m, 45 m, 80 m, 120 m, 160 m, and 250 m. Six-hour mean zonal and meridional velocity components, u and v, were fit with a cubic spline (Akima, 1970), as described in the previous section. Vertical shear of the zonal and meridional components, $\partial u/\partial z$ and $\partial v/\partial z$, respectively, were computed from the spline fit. In a comparison study using 8-meter vertical resolution acoustic Doppler current profiler (ADCP) data from 1991, the Akima spline provided a more realistic shear profile than that computed by linear interpolation from centered differencing (Figure 3.4). Shear squared values in the high-shear region below the EUC core are underestimated due to the greater vertical separation of current meters below 120 m. Although these shear estimates are far from ideal, they are reasonable and likely the best available for the time and location of this study. Vector shear and shear squared were computed from the component shears.

4. Richardson Number

Gradient Richardson number, Ri, an indicator of the dynamic stability of the water column, is defined as the ratio between the density stratification, N^2, and the velocity shear squared, S^2. Generally, the small-scale, or local, instantaneous Ri is desired, but is often not available due to limited vertical and temporal resolution. Clearly, the resolution of these time series measurements do not satisfy the local and instantaneous conditions. Nevertheless, for the objectives defined here, i.e. to characterize the seasonal and interannual variability of the diurnal cycle of high-frequency temperature

variability, or internal waves, mean Ri provides a useful indicator of mean processes occurring on these longer time scales.

Six-hourly averaged Ri was computed from the ratio of the six-hourly N^2 to six-hourly S^2. This ratio is likely to differ from the mean of the ratio of 15-minute N^2 to the 15-minute S^2. Monthly mean values of Ri were computed for each of the four six-hour time bins. Since S^2 is sometimes vanishingly small, some values of Ri, which has S^2 in the denominator, become quite large. To prevent these occasional large values from significantly weighting the monthly means, values exceeding 150 were truncated and the remaining values were smoothed with a 1-2-1 running mean filter. Due to the averaging operators used and the coarse vertical resolution of the data, particularly velocity, the numerical values of mean Ri are expected to be somewhat higher than those measured on smaller scales using microstructure measurements.

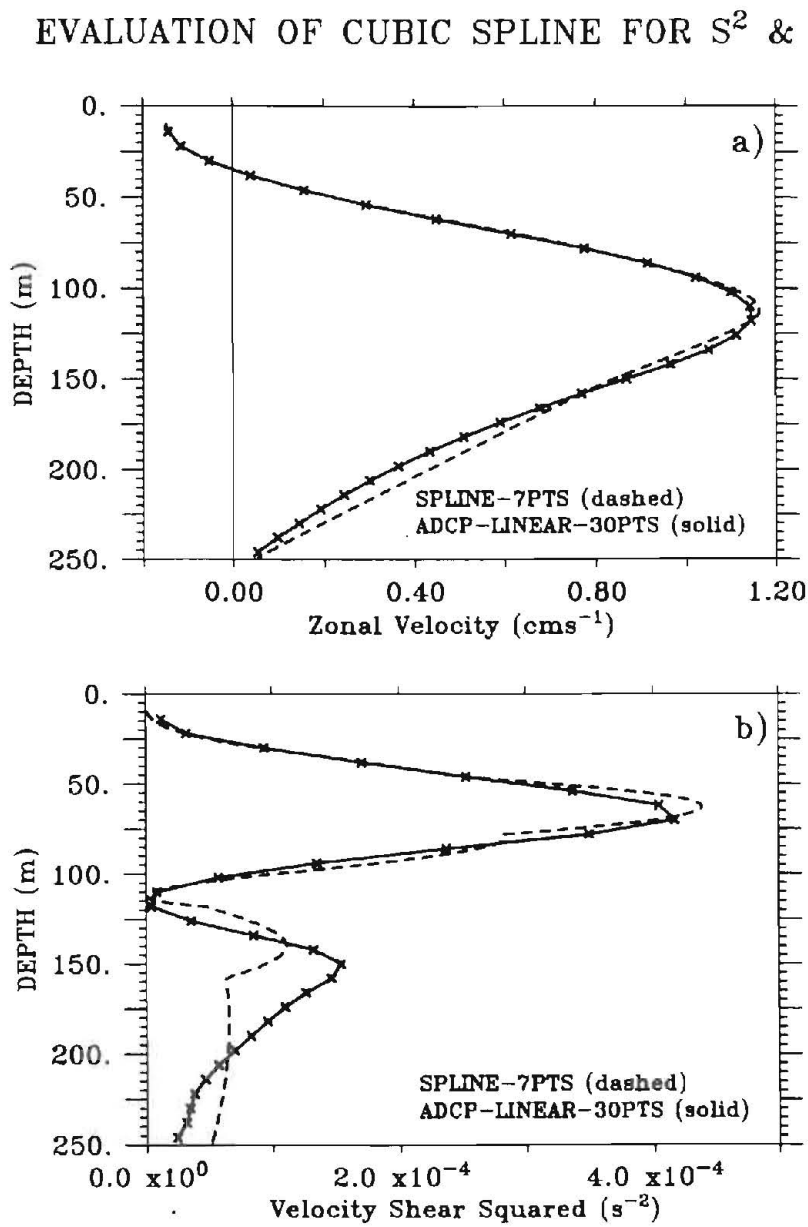

Figure 3.4. Comparison of vertical profiles of a) zonal velocity and b) velocity shear squared computed from 8 m vertical resolution ADCP data at 0°, 140°W (solid) and cubic spline fit to 7 ADCP depths corresponding to current meter depths (dashed).

5. Mixed-Layer Depth

The thickness of the mixed layer determines both the thermal and the mechanical inertia of the layer in direct contact with the atmosphere and influences the fluxes at the base of the layer. The study of mixed-layer depth and its variability is of fundamental importance for the understanding and interpretation of thermal and velocity fields of the upper ocean, for parameterizing mixed-layer processes, and for determining air-sea fluxes (Schneider and Muller, 1990). Numerous definitions for mixed-layer depth have been described in the literature. Gradients or differences from the surface of either temperature, salinity, or density have been specified that cannot be exceeded within the mixed layer. Wyrtki (1964) used a temperature difference of 0.5 C. Lukas and Lindstrom (1987) employed critical gradients of temperature (0.05 Cm^{-1}, 0.025 Cm^{-1}), salinity (0.02 m^{-1}, 0.01 m^{-1}),and potential density σ_θ (0.01 kgm^{-3}). Peters et al. (1989) used a difference of σ_θ of 0.01 kgm^{-3}. McPhaden and Peters (1992) used a temperature gradient of $0.01Cm^{-1}$. None of these definitions may be ideal for every situation, and it is advisable to examine individual data sets prior to defining the requisite criterion. After examining individual and monthly mean profiles of temperature and temperature gradient, the definition of mixed-layer depth based on the depth where the gradient first reaches $0.01Cm^{-1}$ was chosen. Using this criterion, mixed-layer depth was computed for each six-hour time bin by linearly interpolating the six-hour mean temperature profiles. Monthly mean mixed-layer depths were then calculated for each of the four time bins.

As an indicator of the diurnal variability of surface layer mixing, daily maximum ranges were computed from the four daily six-hour values of mixed-layer depth, i.e. the difference between each daily maximum mixed-layer depth and each daily minimum mixed-layer depth. Monthly mean diurnal ranges of mixed-layer depth were computed from the daily values.

In this study, both mixed-layer depth and diurnal range of mixed-layer depth are used as measures of the net amount of surface layer mixing. Since high-frequency temperature fluctuations in the thermocline are likely to be related to surface layer mixing and the processes which generate surface layer mixing, relationships between these measures of surface layer mixing and IDV and the diurnal cycle of IDV are

examined.

6. Surface Heat and Buoyancy Fluxes

Diurnal modulations of the upper ocean mixing processes observed at 0°,140°W are driven from the surface by either mechanical forcing of surface wind stress or thermodynamic forcing of surface buoyancy flux. Diurnal variations in mechanical forcing are possible since there are small but significant diurnal variations in wind speed (Deser, 1994). These diurnal variations are likely to be smaller than the pronounced diurnal variation of the surface buoyancy flux. The surface buoyancy flux determines the amount and intensity of convective mixing. The ocean moves because of buoyancy contrasts due to differences of both temperature and salinity. These differences are created by the fluxes of heat and water at the ocean surface, whose combined effect on buoyancy, $-g\rho$, is called the buoyancy flux, B, which is given by:

$$B = \frac{g\alpha}{c_w} Q_{net} + g\beta(E-P)s ,$$

where $E = \rho_a c_e (q_s - q_a) U$ is the evaporation rate, P is the precipitation rate, c_w is the specific heat of water (3998 $Jkg^{-1}K^{-1}$), s is the surface salinity (35.0), $\alpha = -\rho^{-1}\partial\rho/\partial T$ is the thermal expansion coefficient of seawater at the surface (2970 x 10-7 K^{-1}), $\beta = \rho^{-1}\partial\rho/\partial s$ is the corresponding coefficient for salinity (-7.39 x 10^{-4}), g is the acceleration of gravity (9.7976 ms^{-2}), U is the surface wind speed, q_a is the specific humidity, q_s is the saturated specific humidity, and Q_{net} is the net surface heat flux (Gill, 1982). Buoyancy flux is a measure of the input of mean potential energy at the ocean surface (Oberhuber, 1988).

Surface heat flux is governed by the balance between shortwave solar irradiance, Q_s, latent or evaporative flux, Q_e, sensible or conductive flux, Q_h, and longwave back radiation, Q_b:

$$Q_{net} = Q_s + Q_e + Q_b + Q_h .$$

Monthly mean values of Q_{net} and B were computed from monthly mean values of Q_s, Q_b, Q_e, Q_h, E, and P. The methods and data sets used in computing these terms are given

in the following several sections.

Since it has been hypothesized that the diurnal cycle of the surface buoyancy flux is related to the diurnal cycle of turbulent mixing in the equatorial thermocline (Moum and Caldwell, 1985; Moum et al., 1989), surface buoyancy and heat fluxes, as well as the individual terms comprising them, are examined over seasonal and interannual time scales. Relationships between these terms and surface layer mixing, IDV and the diurnal cycle of IDV are determined.

Although there is evidence of a diurnal cycle of precipitation over the tropical oceans (Gray and Jacobson, 1977; Dorman and Bourke, 1979; Meisner and Arkin, 1987), observations of the diurnal cycle of turbulent mixing in the equatorial Pacific were observed during times when precipitation was not observed and the surface buoyancy flux was controlled by the surface heat flux (Peters et al., 1988; Moum et al., 1989). Therefore, it is not unreasonable to assume that the surface heat flux, which changes diurnally with the rising and setting of the sun, dominates the diurnal cycle of the surface buoyancy flux at 0°, 140°W.

7. Surface Solar Irradiance

Bond and McPhaden (1994) and Imawaki et al. (1988) found that the day-to-night difference of the sea surface cooling, which they define as the sum of the net Q_e, Q_h, and Q_b, is negligible compared with the net solar irradiance. As expected, they found large day-to-night differences in Q_s. Additionally, Bishop and Rossow (1991) described significant variability of Q_s over time scales varying from daily to interannual. They attribute this variability to changes in cloud fraction and atmospheric composition.

For the four-year period examined here, direct observations of solar irradiance were not available in the central equatorial Pacific. However, monthly mean estimates of surface solar irradiance have been computed for the entire time series using ISCCP cloud data. The computationally fast radiative transfer model of Bishop and Rossow (1991) for surface solar irradiance utilizes the following ISCCP data: solar zenith angle ($æ_o$), atmospheric water vapor profile and ozone column abundance, cloud fraction, cloud optical thickness, visible surface reflectance, and surface pressure. This algorithm uses the Frouin et al. (1989) formula for the solar irradiance at the surface under clear sky

conditions. The cloudy sky component utilizes spherical and directional albedos derived using optical thickness from tables. These tables, which allow a major improvement in computation speed, are obtained from full Mie calculations (Hansen and Travis, 1974) and provide a physical link between the observed cloudy scene reflectance and the total cloud transmission that is the basis for all methods for calculating surface solar irradiances (Tarpley, 1979; Gautier et al., 1980; Darnell et al., 1988; Bishop and Rossow, 1991). The total incident solar irradiance is the sum of the clear and cloudy sky components.

Monthly mean surface solar irradiance values for the period November 1983 through October 1987 were provided by Dr. J. Beauchamp at Goddard Institute for Space Studies. These monthly means were computed from 3-hourly 2.5° x 2.5° ISCCP data. In addition to the surface solar irradiance values computed using the radiative transfer model, monthly mean values of surface solar irradiance were computed from bulk formalae, $Q_s/Q_0 = 1 - 0.76C + 0.0019\alpha$, where Q_s is the insolation under cloudy conditions, Q_0 the insolation under clear skies from the Smithsonian formula, C cloud fraction from ISCCP data, and α is noon solar altitude (Reed, 1977; Weare et al., 1981; Seager et al., 1988; Blumenthal and Cane, 1989).

8. Longwave Radiation

Although the diurnal cycle of longwave radiation has been reported to be small (Imawaki et al., 1988; Bond and McPhaden, 1994) the concern here is with the effect of seasonal and interannual variations of longwave radiation on the diurnal cycle of upper ocean mixing and high-frequency temperature variability. During this four-year study period, however, no direct measurements of net longwave radiation were made. In fact, due to the difficulty of making direct radiation measurements at sea, there are few long-term observations of longwave radiation over the oceans at any location. Data acquired during the GARP Atlantic Tropical Experiment (GATE) revealed spatial and temporal variability of longwave radiation of about 30 Wm^{-2}, presumably due to mesoscale and small-scale variations in cloudiness and other meteorological parameters (Fung et al., 1984). Surface longwave radiation depends on the integrated results of absorption, emission, and scattering in the entire inhomogeneous atmospheric column. Due to the scarcity of direct observations, empirically derived bulk formulae are

traditionally used to estimate monthly mean net longwave radiation at the ocean surface (Clark et al., 1974; Bunker, 1976; Wyrtki, 1965; Hastenrath and Lamb, 1978). Although these methods do not adequately account for the dependence on the concentrations of atmospheric constituents and on the vertical distribution of temperature, humidity, and cloud properties, they are generally the best available estimates. The various bulk formulae, which use marine observations of SST, near-surface air temperature, humidity, and cloudiness, often give dissimilar results for given parameters (Fung et al., 1984).

Monthly mean net longwave radiation was computed following the procedure given in the Ocean Observing System Development Panel's Background Report on Surface Conditions and Air-Sea Fluxes (Weller and Taylor, 1993), which uses the clear sky formula of Clark et al., (1974),

$$LW_{cs}\uparrow\downarrow = \epsilon\sigma T_s^4(0.39-0.05(e_a)^{1/2}) + 4\epsilon\sigma T_s^3(T_s - T_a) \quad .$$

The emissivity, ε, is taken to be 0.98; $\sigma = 5.67 \times 10^{-8}$ $Wm^{-2}K^{-4}$ is the Stefan-Boltzmann constant, and near-surface air temperature (T_a) and SST (T_s) are in degrees Kelvin. Input data were gathered from the following sources in order of preference: mooring data for T_a and T_s, when available; COADS monthly means of T_a, T_s, specific humidity (q), and sea level pressure (p), when available; and the Esbensen and Kushnir (1981) climatology for T_a, T_s, q, and p. Vapor pressure (e) was computed as:

$$e = \frac{qp}{(q + \epsilon - (\epsilon q))},$$

where $\varepsilon = 0.622$ (Gill, 1982). The cloud correction of the longwave radiation was made using the cloud correction factor recommended by Clark et al. (1974),

$$LW\uparrow\downarrow = LW_{cs}\uparrow\downarrow(1 - bC^2),$$

where $b = 0.62$ and C is the cloud fraction obtained from the ISCCP data. Upward and downward arrows indicate the net of the upward and downward components of longwave radiation. Using this procedure monthly mean values of net surface longwave radiation were computed for the 48-month observation period.

9. Latent Heat Flux

Of the four terms in the surface heat flux in the central equatorial Pacific, the latent heat flux, Q_e, is typically the largest source of heat loss from the ocean surface

to the atmosphere. Climatological values of Q_e at 0°, 140°W computed using bulk formulae range between about -75 and -110 Wm^{-2}. Using available data from several sources, Q_e was computed as:

$$Q_e = -\rho_a l_v C_e (q_s - q_a) U = l_v E$$

where ρ_a is the density of air (1.225 kg m^{-3}), l_v is the latent heat of vaporization, C_e is the transfer coefficient for latent heat or Dalton number (1.15 x 10^{-3}), q_s is the saturation specific humidity, q_a is the specific humidity measured near the sea surface, and U is the surface wind speed (Large and Pond, 1982; Weller and Taylor, 1993). The latent heat of vaporization was computed as:

$$l_v = [2.501 - 0.00237 \times T_a] \times 10^6 \quad Jkg^{-1}$$

where T_a is the air temperature. The saturation specific humidity was computed using Tetens' formula (Buck, 1981):

$$P_v = (1.007 + 3.46 \times 10^{-6} \times P) \times 6.1121 \times \exp\left(\frac{17.502 \times T_a}{240.97 + T_a}\right)$$

$$q_s = 0.62197 \times \frac{P_v}{(P - 0.378 \times P_v)}$$

where P_v is the vapor pressure and P is the atmospheric pressure. Depending on data availability, U and T_a were measured from the moored buoys, and q_a and P were taken from the COADS climatology. When buoy observations of U or T_a were unavailable, the climatology of McPhaden and McCarty (1992) was used. When COADS observations of q_a or P were unavailable, the Esbensen and Kushnir (1981) climatology was used.

Since observations of q_a were available for only 19 of the 48 months of this study, the sensitivity of the calculation of Q_e to q_a was examined by comparing values of Q_e computed using COADS observations of q_a to values of Q_e computed using the Esbensen and Kushnir climatological values of q_a (Figure 3.5). The root-mean square (rms) difference was 21.31 Wm^{-2}, or more than 25% of the mean Q_e for the COADS data, -77.4 Wm^{-2}. Despite the large rms difference, the correlation between these fields

is 0.67.

10. Sensible Heat Flux

Sensible heat flux, Q_h, is typically the smallest term of the surface heat flux, with climatological values of about -2 to -5 Wm^{-2}. Monthly means of sensible heat flux were computed as:

$$Q_h = \rho_a c_p C_s (T_s - T_a) U$$

where c_p is the specific heat of dry air (1004.67 $m^2 s^{-2} K^{-1}$), C_s is the transfer coefficient for sensible heat or Stanton number, and T_s is the sea surface temperature. A Stanton number of 1.15×10^{-3} was used for unstable conditions ($T_s > T_a$) and 0.75×10^{-3} was used for stable conditions ($T_s < T_a$) (Large and Pond, 1982; Weller and Taylor, 1993). Based on monthly mean T_s-T_a differences, stable conditions occurred during 48% of the months.

11. Precipitation

Unlike the situation over land, direct measurements of precipitation over the oceans are rare, particularly over the central equatorial Pacific. Three atlases of precipitation have been used to provide a range of estimates of monthly mean precipitation near 0°, 140°W (Table 3.3). Dorman and Bourke (1979) derived estimates of precipitation for 2° latitude by 5° longitude rectangles over the Pacific using present weather observations taken by ships. Using the method of Tucker (1961), measured rainfall amounts at land stations were related to the present weather reported in the synoptic observations. Corrections related to local temperature biases were also applied. Over the 1952-1979 period of their study, only about 500 observations were reported for each of the 2° x 5° rectangles surrounding 0°, 140°W. They reported that this is the minimum number of observations for reliable estimates. Their analysis indicated annual precipitation of about 800 mm (Figure 3.6). Seasonally, their estimates showed increased precipitation during the boreal spring and decreased precipitation during the fall and winter.

Shea (1986) produced a global precipitation atlas based on objective analysis of shore station data. Oberhuber (1988) used this atlas and an analysis of the surface salinity field of Levitus (1982) to produce a precipitation climatology. In the

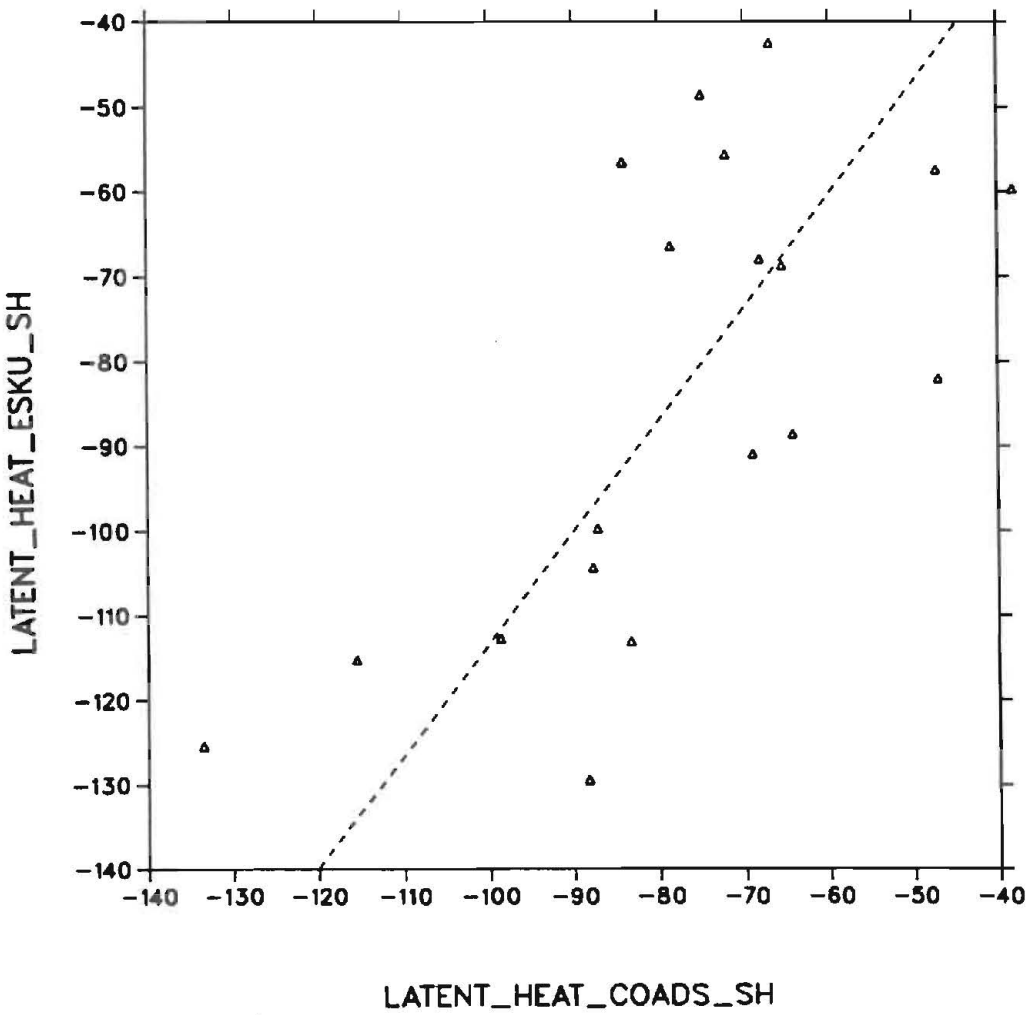

Figure 3.5. Comparison between monthly mean values of latent heat flux computed using specific heat acquired from monthly COADS observations and latent heat computed using specific heat acquired from the Esbensen and Kushnir (1981) climatology.

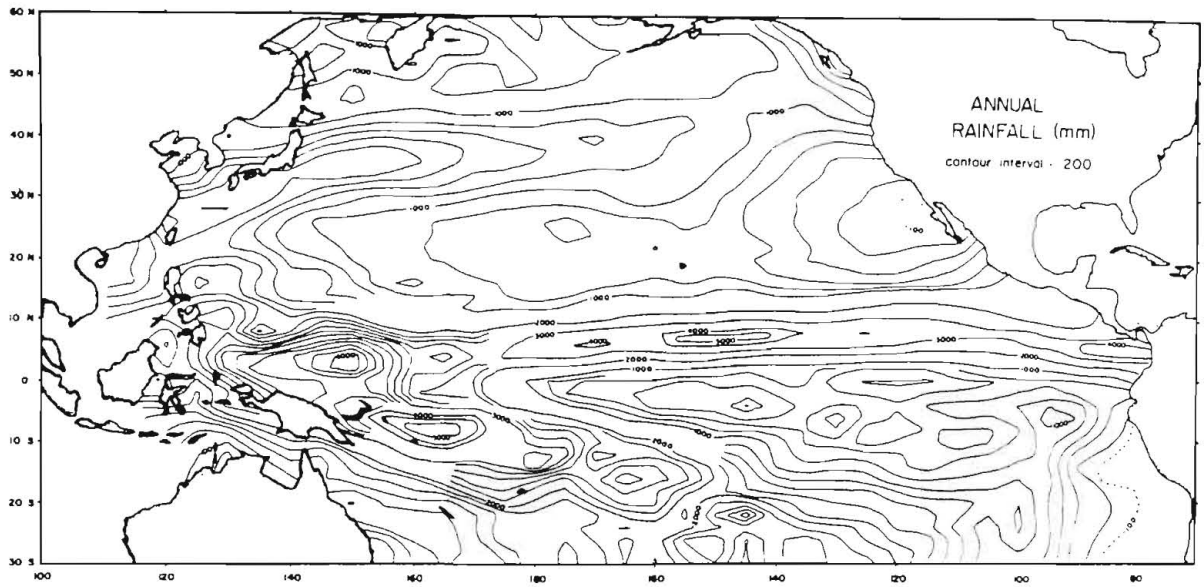

Figure 3.6. Mean annual precipitation over the Pacific Ocean between 30°S and 60°N from Dorman and Bourke (1979).

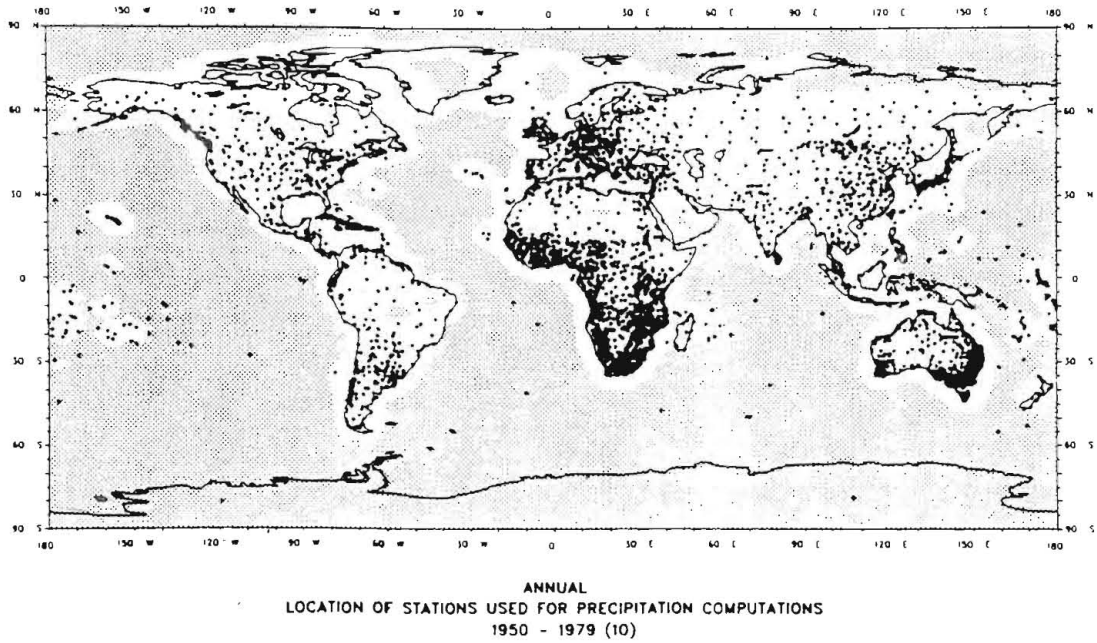

Figure 3.7. Locations of stations used for precipitation atlases of Shea (1986) and Oberhuber (1988) for the period 1950-1979.

vicinity of 0°, 140°W, these analyses are based on widely-spaced distant island stations (Figure 3.7). The Oberhuber climatology indicates annual precipitation amounts of about 1000 mm. The annual cycle is characterized by precipitation rates of about 130 mm mth^{-1} in the boreal spring and about 35 mm mth^{-1} in the boreal fall (Table 3.3, Figure 3.8). Considering the scarcity of observations in both climatologies, the agreement is good. Both atlases indicate a strong precipitation gradient north of the equator associated with the inter-tropical convergence zone (ITCZ). This strong gradient suggests the possibility of significant variability of precipitation as the ITCZ varies seasonally and interannually.

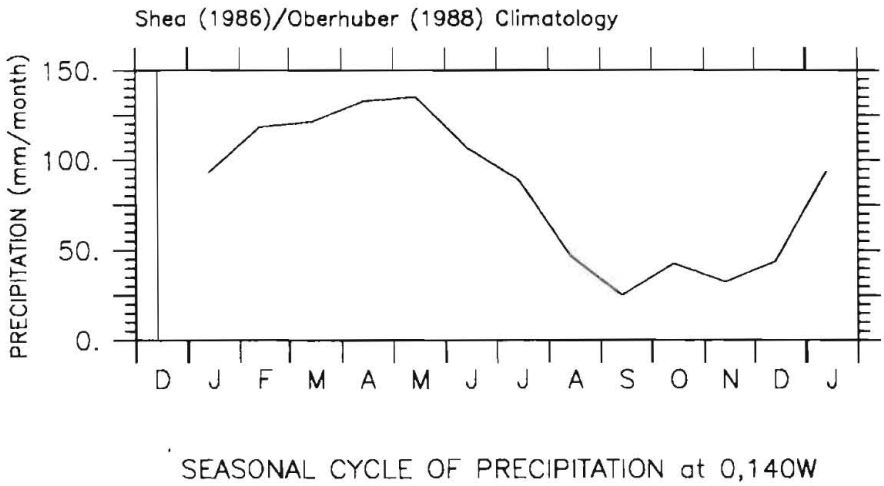

Figure 3.8. Seasonal cycle of precipitation at 0°, 140°W from Shea (1986)/Oberhuber (1988).

Table 3.3. Climatological values of precipitation at 0°, 140°W from Dorman and Bourke (1979), Shea(1986)/Oberhuber (1988), and Janowiak and Arkin (1991). Units are *mm* mth^{-1}.

PERIOD	Dorman & Bourke	Shea/Oberhuber	GPCP
JANUARY	50-100	93.3	14.9
FEBRUARY		118.2	39.3
MARCH		121.3	53.0
APRIL	200	132.8	65.1
MAY		135.1	61.4
JUNE		106.6	8.1
JULY	100	88.8	3.7
AUGUST		46.9	2.2
SEPTEMBER		25.1	1.2
OCTOBER	50-100	42.6	0.9
NOVEMBER		32.5	3.9
DECEMBER		43.9	3.4
ANNUAL MEAN	800	987.1	257.0

Another indication of the magnitudes of precipitation and the seasonal and interannual variability of precipitation at 0°, 140°W is provided by the satellite-derived precipitation estimates from the Global Precipitation Climatology Project (GPCP). Using infrared (IR) data from geostationary and polar-orbiting satellites, Janowiak and Arkin (1991) derived pentad (5-day) and monthly rainfall estimates in the tropics during 1986-1989 using a simple cloud-top temperature-thresholding algorithm. Dr. Janowiak kindly provided an updated time series of precipitation estimates computed by the same method for the period January 1986 through December 1993 (Figure 3.9a). These data show high precipitation rates during the 1986/1987 and 1991/1992 ENSO warm episodes and precipitation rates considerably lower than the Dorman and Bourke (1976) and Shea(1986)/Oberhuber (1988) climatologies during non-ENSO years. The eight-year

GPCP time series of monthly mean precipitation estimates was used to calculate the GPCP climatology shown in Table 3.3. This climatology indicates annual precipitation at 0°, 140°W of about 257 mm, considerably less than the two other climatological estimates.

Using the GPCP climatology for the period November 1983 - December 1985 and the GPCP monthly mean observations for the period January 1986 - October 1987, a composite time series of precipitation estimates for the study period was derived. The composite GPCP time series and the Shea (1986)/Oberhuber (1988) climatological time series are compared in Figure 3.9b. Except for a sharp peak in precipitation during the spring of 1987, the GPCP precipitation estimates are consistently much smaller than the precipitation estimates given by the Shea/Oberhuber climatologies. Since both the Shea/Oberhuber and Dorman and Bourke climatologies were based on scarce data, greater confidence is given to the GPCP data. Unfortunately, these data have not been validated with reliable surface measurements in the central equatorial Pacific , so uncertainty remains. Therefore, buoyancy flux calculations were performed using precipitation estimates from both the GPCP time series and the Shea/Oberhuber climatology.

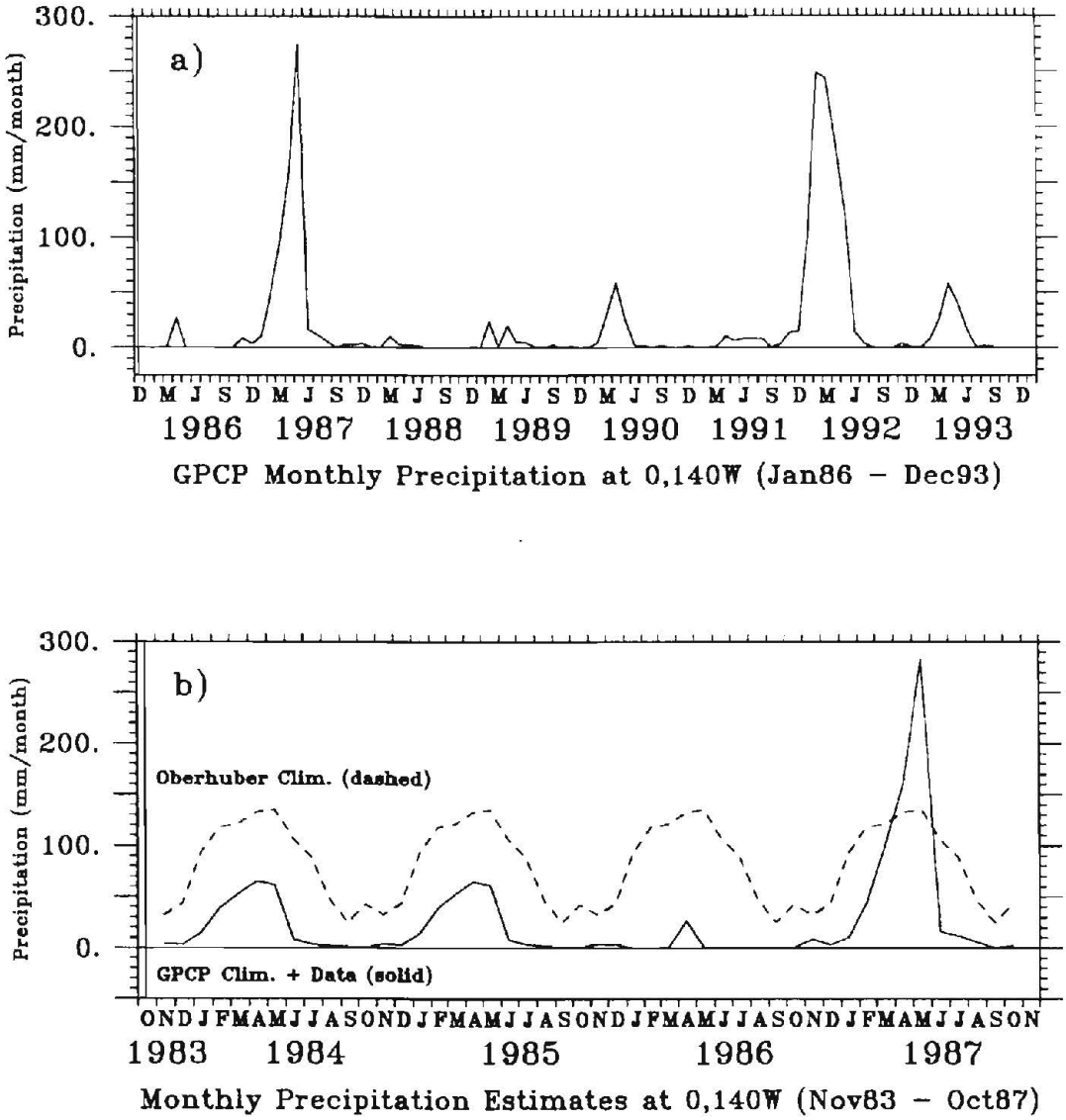

Figure 3.9. a) Time series of satellite-derived monthly mean GPCP precipitation estimates for the period January 1986 through December 1993 averaged between 2.5°N and 2.5°S and 138.75°W and 141.25°W (from Dr. J. Janowiak). b) Comparison between time series of monthly mean precipitation estimates based on a composite of GPCP climatology and observations and on the Shea/Oberhuber climatology for the period November 1983-October 1987. Units are mm mth^{-1}.

12. Wave Momentum Flux

As discussed in the introduction, one of the concerns here is the diurnal modulation of the wave induced zonal momentum flux. The Skyllingstad and Denbo (1994) model results showed that internal waves can provide an efficient mechanism for the vertical transport of horizontal momentum. In their modeled surface mixed layer, the internal waves gained eastward momentum at the expense of the background flow. In some cases, this momentum was transferred back to the mean flow at a critical level resulting in a deceleration below the undercurrent core. Otherwise, the waves tended to decrease the current velocity above the EUC core. In an effort to compare their model results to observations, wave momentum flux, $u'w'$, shear production of turbulent kinetic energy, $(u'w')\partial u/\partial z$, and wave stress divergence, $\partial/\partial z(u'w')$, were computed using the moored buoy data. As with IDV calculations, the temperature and velocity data were effectively high-pass filtered to remove the dominant tidal effects by segmenting the data into 6-hour time bins and fitting each to a cubic polynomial. The residuals, u' and T', were then used to compute the above variables as follows:

$$u_n' = \frac{(u_{n+1}' + u_n')}{2}, \qquad n = 1,23$$

$$w_n' = \frac{(\zeta_{n+1} - \zeta_n)}{\Delta t}, \qquad where \quad \zeta_n = \frac{T_n'}{\partial T/\partial z}.$$

$$\overline{\frac{\partial u'w'}{\partial z}} = \overline{\frac{u_n'w_n'(z_1) - u_n'w_n'(z_2)}{\Delta z}}.$$

As before, the Δt for all of the observations was 15 minutes, however, the individual observations of velocity represent 15-minute averaged quantities, whereas some of the temperatures are 15-minute averages and some are 15-minute spot samples. The 15-minute averaged temperatures and velocities have had the higher frequencies effectively removed by averaging. In the calculation of w', the mean vertical temperature gradient, $\partial T/\partial z$, was computed using centered differencing. In the calculation of the shear production of TKE, the vertical velocity shear was computed as described previously.

C. SENSITIVITY STUDY OF COMPUTED IDV

Since the primary focus of this investigation is an examination of the diurnal cycle of high-frequency temperature variability, the following sensitivity studies were performed to verify the suitability of the method of computing monthly mean IDV. Since the sampling period of 15 minutes is insufficient to resolve all of the high-frequency waves of interest, it was necessary to rely on statistical methods to examine the character of these high-frequency waves. It was hypothesized that with sufficient averaging of the variances of the 15-minute spot sampled temperatures it would be possible to enhance the diurnal signal of the high-frequency waves. To examine this hypothesis, two simple studies comparing the computations of IDV using the 15-minute temperatures to two high-frequency data sets were performed.

1. Comparison With TROPIC HEAT I Results

Values of IDV were computed for the month of November 1984 and for the week of November 25 -December 1, 1984 (Figure 3.10). This latter period was chosen to coincide with the TROPIC HEAT 1 observation period when Wijesekera and Dillon (1991) presented isopycnal displacement variance as a function of time of day (Figure 3.10a). Their calculations of isopycnal displacement variance were computed from microstructure profiles obtained using the rapid sampling vertical profiler (RSVP) (Caldwell et al., 1985). Measured variables were depth, temperature, salinity, potential density, and turbulent kinetic energy (TKE) dissipation rate. The high vertical and temporal resolution of their data allowed isopycnal displacements to be computed directly from individual Thorpe-ordered density profiles (Thorpe, 1977). After removing the 0.1 running mean from these profiles, they computed IDV. Comparison between their isopycnal displacement variances (Figure 3.9a) and IDV computed here (Figure 3.10b) shows reasonable agreement, particularly with regard to the vertical structure of the diurnal variations. Generally, the vertical structure is similar, but the magnitudes of their displacement variances are larger by about a factor of two. The reason for the difference in magnitudes remains unclear, but could be partially due to the higher vertical resolution of their data, the inclusion of salinity in their observations, and their shorter sampling interval of 7.5 minutes, as opposed to the 15-minute sampling interval used here. The

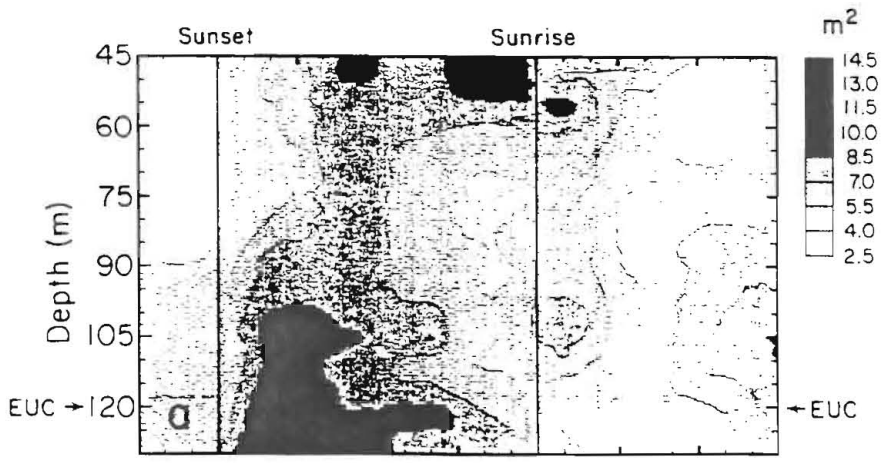

Isopycnal Displacement Variance (m^2)

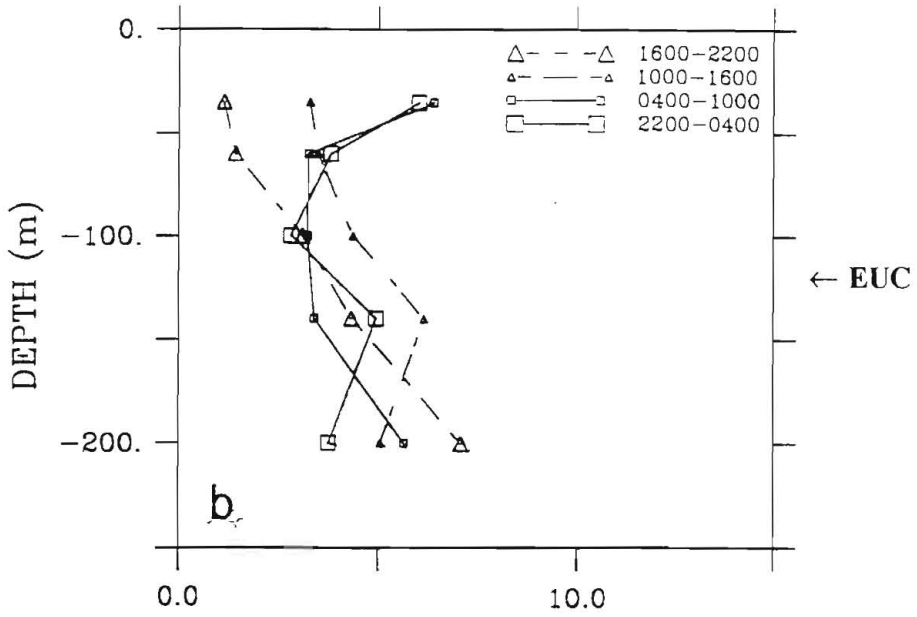

Isotherm Displacement Variance (m^2)

IDV at 0°, 140°W (Nov 25 - Dec 1, 1984)

Figure 3.10. Comparison between a) mean isopycnal displacement variance from TROPIC HEAT microstructure measurements by Wijesekera and Dillon (1991) during November 25-December 1, 1984 at 0°, 140°W, and b) mean isotherm displacement variance (IDV) for four six-hour time bins using moored buoy data from the same time period and location.

magnitudes show a pronounced diurnal cycle of isopycnal displacement variance between 105 m and 130 m that is not evident in the IDV results computed from the mooring data. Given the resolution differences, and the fact that in this case the mooring data were averaged only over seven days, the correspondence between IDV results is noteworthy.

2. Comparison With 1-Minute TR Data

Although the comparison with Wijesekera and Dillon showed reasonable agreement, differences are apparent and the results are not conclusive. Therefore, 1-minute spot-sampled temperature data at 40 m depth for the period, May 12 - June 11, 1987, were used to further validate our methodology. This is a subset of the data examined by McPhaden and Peters (1992), who showed a diurnal cycle of IDV at frequencies near N (10-30 cph). The identical procedure for calculating IDV with the 15-minute data was used to calculate IDV with the 1-minute data, including segmenting the data into six-hour bins and fitting the data in each bin with a cubic polynomial. Temperature variances were then computed from the 6-hour residuals, which in this case were composed of 360 data points. These variances were then normalized by the vertical temperature gradient to compute IDV. Thus, 30 daily IDVs were computed for each of the four 6-hour time bins. Using these 1-minute IDVs as a standard, this procedure was then repeated after subsampling the 1-minute data in two ways. First, for each 15-minute period, the 1-minute temperatures were randomly subsampled. Values of IDV were then computed from the resulting unevenly spaced time series using the above procedure. The resulting 30 IDV values for each time bin were then correlated with the 1-minute IDV values (Table 3.4). Correlations were strong with values ranging between 0.9173 and 0.9867. Next, the 1-minute temperatures were subsampled every 15 minutes and the IDVs and correlations with the 1-minute IDVs were computed (Table 3.4). Again, correlations were strong with values ranging between 0.9100 and 0.9858. Both sets of correlation coefficients indicate strong agreement between the 1-minute IDVs and the 15-minute IDVs, indicating that the methodology is suitable for characterizing the variability of high-frequency internal waves.

Table 3.4. Correlation coefficients between 30 day time series measurements of 1-minute temperature data at 40 m depth and 15-minute randomly subsampled and periodically subsampled temperatures for the four local time bins listed.

LOCAL TIME BIN	15-minute RANDOM	15-Minute PERIODIC
2200 - 0400	0.9173	0.9100
0400 - 1000	0.9472	0.9535
1000 - 1600	0.9867	0.9858
1600 - 2200	0.9843	0.9168

IV. BACKGROUND CONDITIONS

A. INTERANNUAL VARIABILITY: ENSO

Oceanic and atmospheric conditions in the central equatorial Pacific exhibit significant temporal variability over scales ranging from diurnal to interannual. The ENSO phenomenon is the most notable and pronounced example of interannual global climate variability. A major ENSO warm episode, such as that which occurred during 1982/1983, leads to massive dislocations of tropical rainfall regimes, bringing drought to vast areas and torrential rains to otherwise arid regions. The related atmospheric circulation anomalies extend deep into the extratropics, where they are associated with unusual and sometimes severe climatic conditions over a variety of regions around the globe.

Although each ENSO warm episode has unique characteristics, with episodes differing in strength, phase, and behavior, it is useful to describe a composite evolution over a period of 18-24 months. The anomalous ocean warming in the Pacific often begins near the Ecuador-Peru coast early in the calendar year, then spreads westward into the central equatorial Pacific. The coastal warming often peaks during April-June, but the warming in the central equatorial Pacific normally continues for several more months, as the high SSTs of the western Pacific spread eastward. The global atmospheric climate anomalies are most widespread and intense near the end of the first year and during the early months of the second year of the episode, i.e., during the boreal winter. This period, approximately one year following the initial appearance of warm water in the eastern Pacific, is often referred to as the mature phase of the episode. Following the mature phase, the anomaly patterns enter a period of slow decay that spans several months.

In November 1983, the beginning of our study period, the monthly Climate Diagnostics Bulletin, reported that the global 1982/1983 ENSO warm event had ended. From November 1983 through early 1985, conditions of the tropical Pacific were indicative of ENSO cold conditions. During this period, satellite-sensed outgoing

longwave radiation (OLR) was anomalously positive, indicating relatively dry conditions. In tropical regions, OLR provides an indication of the intensity of atmospheric convection and the related precipitation. Lower level winds were anomalously easterly in the central equatorial Pacific. The Southern Oscillation Index (SOI), computed from differences of sea level pressure anomalies at Tahiti and Darwin, was near normal over much of this period. Temperature measurements at 0°, 140°W revealed anomalously low SSTs and shallow thermocline depths throughout this period. Progressing through 1985, conditions across the tropical Pacific suggested a trend toward the build-up phase of ENSO that often precedes ENSO warm episodes (Climate Diagnostic Bulletins, 1985). This phase was characterized by slowly increasing SOI, anomalous low level easterlies, below normal equatorial SST, high sea level in the western Pacific, low sea level in the eastern Pacific, low convective activity in the central Pacific, and high convective activity in the western Pacific. In early 1986, several of the ENSO indices suggested the possible development of an ENSO warm episode, but by May 1986 conditions across the tropical Pacific had returned to near normal, where they remained through the boreal summer. During the fall of 1986, most of the atmospheric and oceanic indices indicated the development of the 1986/1987 ENSO warm episode. By October 1986, positive SST anomalies were observed across much of the equatorial Pacific, weak westerly wind anomalies were observed in the central and eastern equatorial Pacific, and negative OLR anomalies were found near the date line at the equator. By November 1987, most of the indices had started a slow return to normal conditions across the equatorial Pacific.

B. INTERANNUAL VARIABILITY: LOCAL CONDITIONS

In this section, local surface forcing and oceanic conditions observed during the four-year period chronicled in the previous section on large-scale interannual ENSO variability are presented. Monthly mean time series of the following observed or computed variables for the 48-month record are presented: zonal and meridional winds, wind speed, shortwave radiation, longwave radiation, sensible heat flux, latent heat flux, net surface heat flux, surface buoyancy flux, subsurface temperature (0-250 m), subsurface zonal and meridional velocity (10-250 m), buoyancy frequency (10-250 m), velocity shear

(10-250 m), gradient Richardson number (10-250 m), mixed-layer depth, diurnal range of mixed-layer depth, and isotherm displacement variance (35 m, 60 m, 100 m, 140 m, and 200 m).

1. Surface Forcing

Monthly mean winds from the mooring at 0°, 140°W are shown in Figure 4.1. The solid curves are monthly means of the observed winds and dotted lines represent the climatological mean annual cycle computed from mooring data during 1983-1991 (McPhaden and McCarty, 1992). Monthly mean winds were anomalously weak (westerly) during the period following the 1982/1983 ENSO warm event through September 1984 and again starting in the fall 1986/winter 1987 and lasting through the 1986/1987 warm episode. Anomalous easterlies prevailed during the later stages of the 1984 cool episode and through the 1985/1986 ENSO build-up phase. Near normal zonal winds during the 1986/1987 winter were followed by a collapse of the zonal winds during the mature phase of the 1986/1987 ENSO warming. Since weak local winds were observed during both the 1984 cold episode and the mature phase of the 1986/1987 warm episode, correlation between local surface winds and the larger scale ENSO conditions did not appear strong, suggesting non-local forcing of ENSO events.

Monthly mean estimates of Q_b, Q_h, Q_e, Q_s, and Q_{net} are presented in Figures 4.2 and 4.3. In Figure 4.2, solid curves represent computed monthly mean estimates and dotted lines represent climatological values. Values of Q_h and Q_e (Figure 4.2b,c) with closed circle symbols were based on COADS monthly means or climatological values of air temperature and specific humidity, respectively. The climatological values of Q_b, Q_h, and Q_e are from the Oberhuber (1988) climatology, which is based on the 2° x 2° COADS data set for the period 1950-1979. The climatology of Q_s was computed following Reed (1977) using COADS cloud data and buoy data for the remaining terms. The climatology of Q_{net} was computed from the climatologies of the four terms.

Net longwave radiation was negative throughout the study period, with a mean net loss of 50.2 Wm^{-2} from the ocean to the atmosphere (Figure 4.2a). Comparison with Figure 4.4a shows the dependence of estimated longwave radiation on SST, and

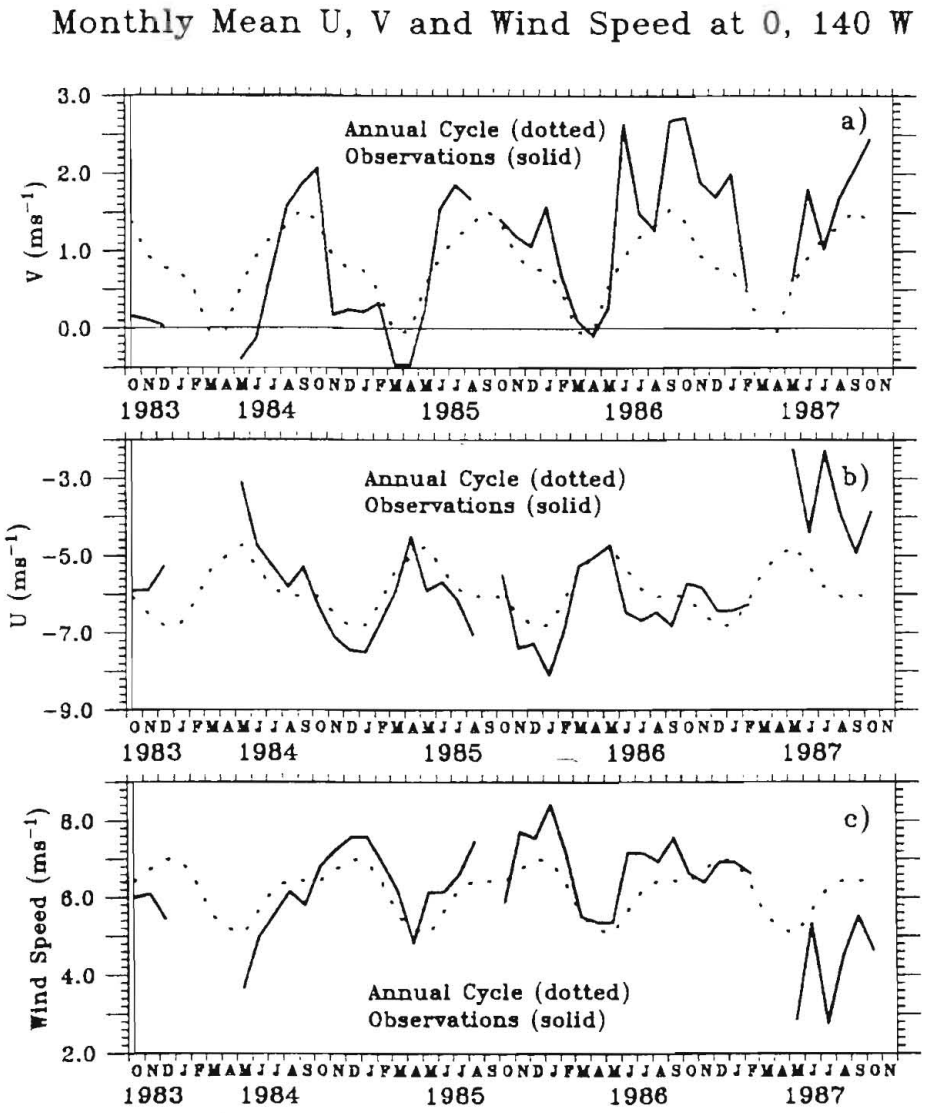

Figure 4.1. Time series of monthly mean values of a) meridional wind, b) zonal wind and c) wind speed at 0°, 140°W during the period November 1983 - October 1987. Solid lines indicate monthly mean observations. Dotted lines indicate climatological means from McPhaden and McCarty (1992).

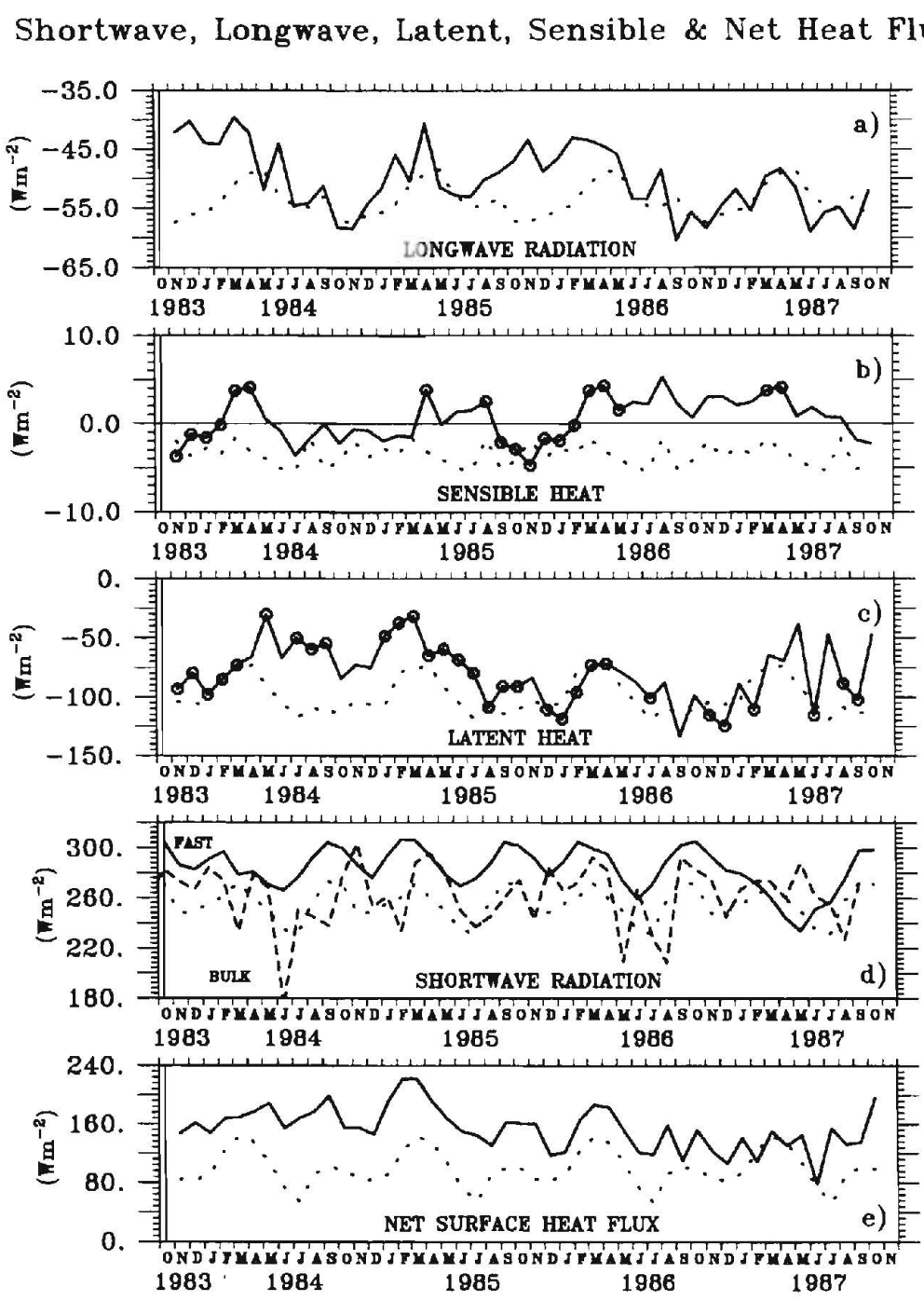

Figure 4.2. Monthly mean surface heat flux terms at 0°, 140°W for the period November 1983 -October 1987: a) longwave radiation, Q_b b) sensible heat flux, Q_h , c) latent heat flux, Q_e, d) shortwave radiation, Q_s, by FAST radiative scheme (solid line) and BULK formula (dashed line), and e) net surface heat flux, Q_{net}. Climatological values are given by dotted lines. Downward fluxes are positive.

therefore the ENSO-related interannual variability of SST. During the 1984 ENSO cold episode net outgoing longwave radiation was reduced to about -40 to -45 Wm^{-2}. Low values of longwave radiation were during the build-up phase of the 1986/1987 ENSO warming. During the mature phase of the warm episode, net outgoing longwave radiation was increased to about -55 to -60 Wm^{-2}.

Sensible heat flux estimates varied between +5 and -5 Wm^{-2} (Figure 4.2b). These estimates were typically about 2-7 Wm^{-2} greater than the climatological estimates of Oberhuber (1988), which were always negative between about -2 and -5 Wm^{-2}. The small relative magnitudes suggest that sensible heat flux had only minor relative significance to the generation of strong convection by diurnal changes in sensible heat (Figure 4.3). Generally, sensible heat flux was negative during the cold episode and positive during the warm episode. Unfortunately, air temperature measurements were available for only 23 of the 48 months of the study, so climatological values of T_a from McPhaden and McCarty (1992) were necessary for much of the time series. Although not shown, time series of 15-minute SST-T_a values show significant variations at periods from hours to weeks.

Latent heat flux represents the largest of the surface heat loss terms (Figure 4.3), with an average monthly mean value of -79.5 Wm^{-2}. With a standard deviation of 25.0 Wm^{-2}, the variability of Q_e, is the largest of the four heat flux terms. Latent heat flux estimates range between about -30 and -135 Wm^{-2} (Figure 4.2c). From March 1984 through March 1985, latent heat flux loss estimates of -25 to -70 Wm^{-2} were about 20-50 Wm^{-2} less than climatological values. From about May 1985 through April 1987, latent heat estimates were near climatological values of about -75 to -120 Wm^{-2}. Latent heat flux estimates varied widely between about -35 and -115 Wm^{-2} during the mature phase of the 1986/1987 warm episode.

Shortwave radiation is the largest term of the surface heat balance with average values of 283.7 Wm^{-2} (Figure 4.3). Shortwave radiation computed from both bulk formulae (dashed line, BULK) and the radiative transfer scheme (solid line, FAST) of Bishop and Rossow (1991) are presented in Figure 4.2d. Both BULK and FAST estimates were consistently greater that the Oberhuber (1988) climatological values (not

shown), by 71.8 and 49.8 Wm^{-2}, respectively. The BULK estimates were lower than the FAST estimates by about 20 Wm^{-2}. The shortwave radiation values computed using the bulk formulae were erratic and cannot be simply related to seasonal or ENSO interannual variability. The FAST shortwave radiation estimates show a well-defined seasonal cycle with a semi-annual period and interannual characteristics apparently related to ENSO. The seasonal cycle appeared greatly diminished during the 1984 cool episode, and there was a significant reduction in downward shortwave radiation during the 1986/1987 warm episode. Since this reduction in incoming shortwave radiation during the warm event did not appear in the simpler bulk formula, which takes into account cloud fraction but not cloud type or vertical structure in the atmospheric column, it appears that their inclusion in the radiative transfer model provides important improvements.

The monthly mean net surface heat flux, Q_{net}, was computed from the monthly mean heat flux terms described above (Figures 4.2e and 4.3). The average net surface heat flux into the ocean was 154.5 Wm^{-2}, with monthly mean values ranging between 223 Wm^{-2} and 78 Wm^{-2}. The standard deviation of the monthly mean heat flux was 29.7Wm^{-2}, indicating large month to month variability. Figure 4.3 shows the relative contribution of the separate terms to the net surface heat flux. As mentioned for the individual terms, Q_s is the dominate surface heat source and Q_e and Q_b are the dominate heat loss terms. The high variability of Q_{net} is largely determined by the variability of Q_e, and to a lesser extent Q_s. Interannually, Q_{net} was relatively high during the 1984 cold episode, with values averaging about 170 Wm^{-2}, and relatively low during the 1986/1987 warm episode, with values averaging about 130 Wm^{-2}.

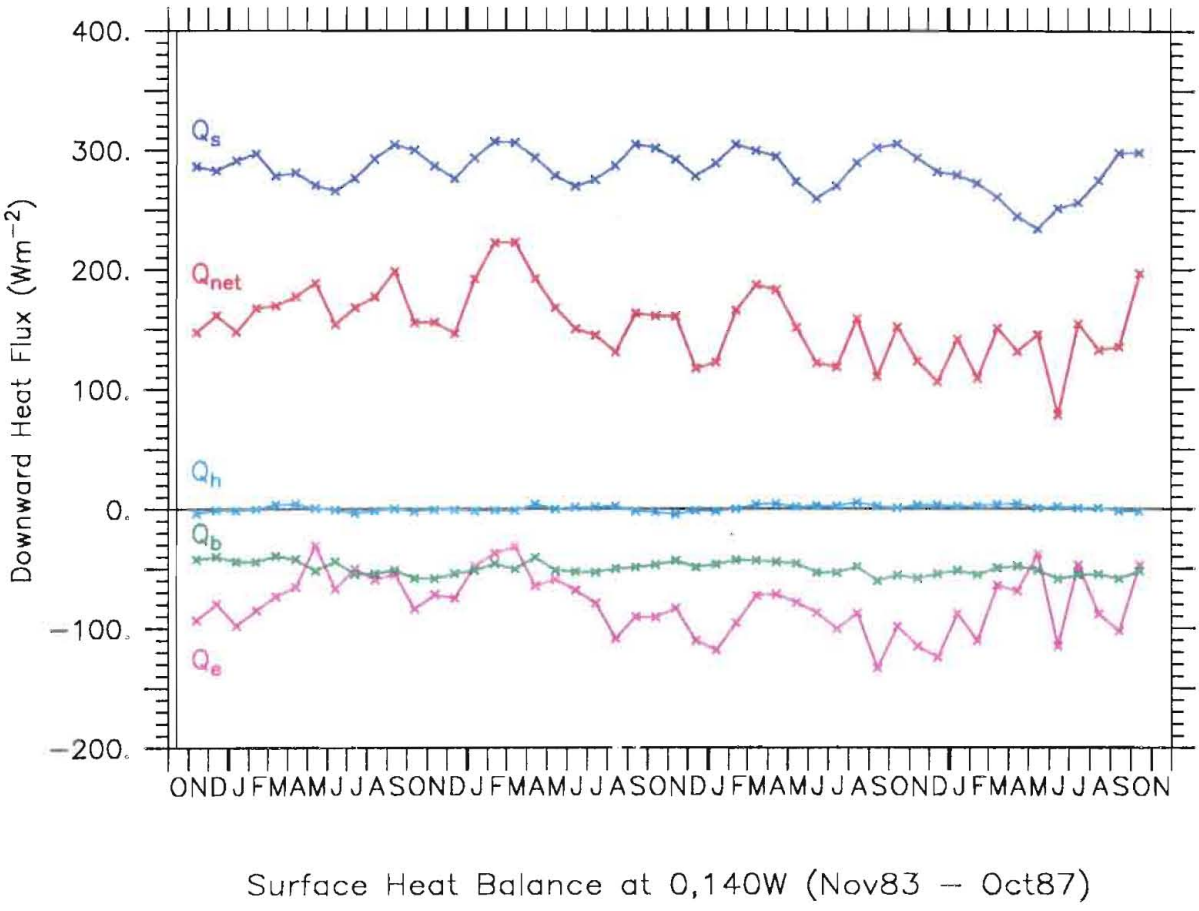

Figure 4.3. Monthly mean values of the terms of the surface heat balance at 0°, 140°W during November 1983-October 1987. Terms include shortwave radiation, Q_s, longwave radiation, Q_b, sensible heat flux, Q_h, latent heat flux, Q_e, and net surface heat flux, Q_{net}. Downward fluxes are positive.

The surface buoyancy flux determines the turbulent vertical motion and amount of convective mixing in the upper ocean. Figure 4.4 shows monthly mean estimates of the net surface buoyancy flux, B_{net}, and the heat and moisture components of the buoyancy flux, B_{heat}, and $B_{moisture}$, respectively. These estimates were based on the above estimates of the net surface heat flux, Q_{net}, and calculations of the surface moisture flux. Surface moisture flux was computed using both the composite of GPCP observations and climatology and the Shea/Oberhuber climatology of monthly mean precipitation, as described in section 3.2.11. Although $B_{moisture}$ values computed using the different precipitation estimates were quantitatively different, the magnitudes in each case were approximately an order of magnitude less than B_{heat}. Even during the large precipitation event during the spring of 1987, B_{net} was largely dominated by B_{heat}.

The average value of B_{net} was -1.155×10^{-7} Wkg^{-1}. These estimates are in rough agreement with the observed daytime and nighttime values of surface buoyancy flux during the TROPIC HEAT experiment, -6×10^{-7} Wkg^{-1} and $+1.5 \times 10^{-7}$ Wkg^{-1}, respectively (Moum et al., 1989). The standard deviation of monthly mean B_{net} was 1.965×10^{-8} Wkg^{-1}. Since B_{net} was determined almost entirely by the surface heat flux, the seasonal and interannual variability of B_{net} was almost identical to that described for Q_{net}. The downward buoyancy flux was greater than average during 1984 and early 1985 and less than average during the 1986/1987 warm episode.

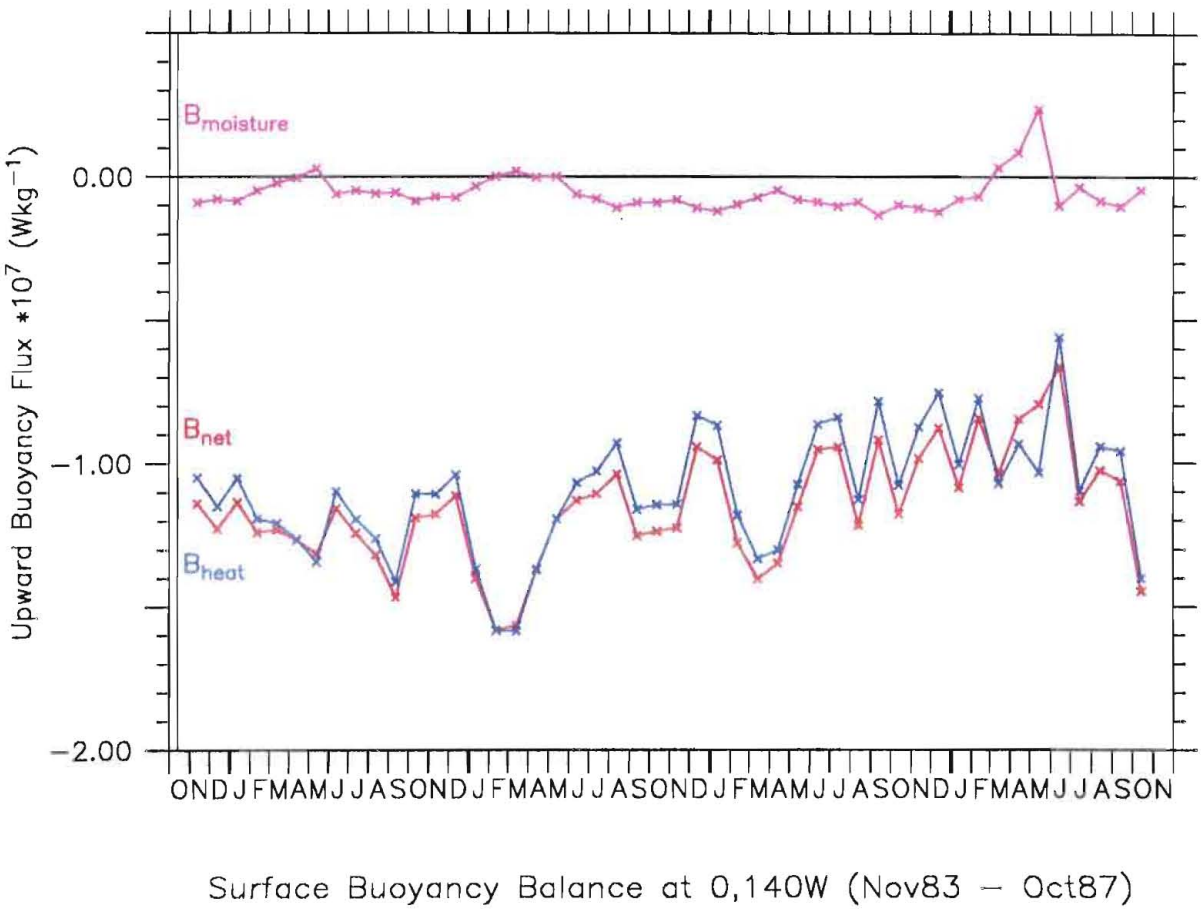

Figure 4.4. Monthly mean values of the terms of the surface buoyancy balance at 0°, 140°W during November 1983-October 1987. Terms include contribution to buoyancy flux by moisture flux, $B_{moisture}$, heat flux, B_{heat}, and net buoyancy flux, B_{net}. Upward buoyancy fluxes are positive.

2. Subsurface Temperature

The subsurface thermal field from the surface to 250 m for the four-year study period is presented in Figure 4.5a. The data were smoothed with a 17-day triangular low-pass filter (20- day half-power point) to remove higher frequency oscillations and to emphasize seasonal and interannual variability. The subsurface temperatures show a progression from cool conditions in 1984, as indicated by cool SSTs and a shallow thermocline, followed by the build-up phase, which was characterized by a steadily deepening thermocline, and ending with the moderate 1986/1987 ENSO warm episode, which was characterized by warm SSTs and a deep thermocline. The depth of the thermocline is often described by the depth of the 20 C isotherm, which is shown to follow the center of the thermocline in Figure 4.5a.

In addition to the interannual variations, the thermocline underwent depth-coherent 60-90 day oscillations that were particularly apparent during the boreal winters of 1984 and 1986. These 60-90 day oscillations were reported by McPhaden and Taft (1988) and ascribed to eastward propagating equatorial Kelvin waves. Kessler et al. (1994), in analyzing data for the period 1983-1993 at 0°, 140°W, report that these intraseasonal waves are typically more prevalent during the boreal winter months and that interannual variability of these waves is not uncommon.

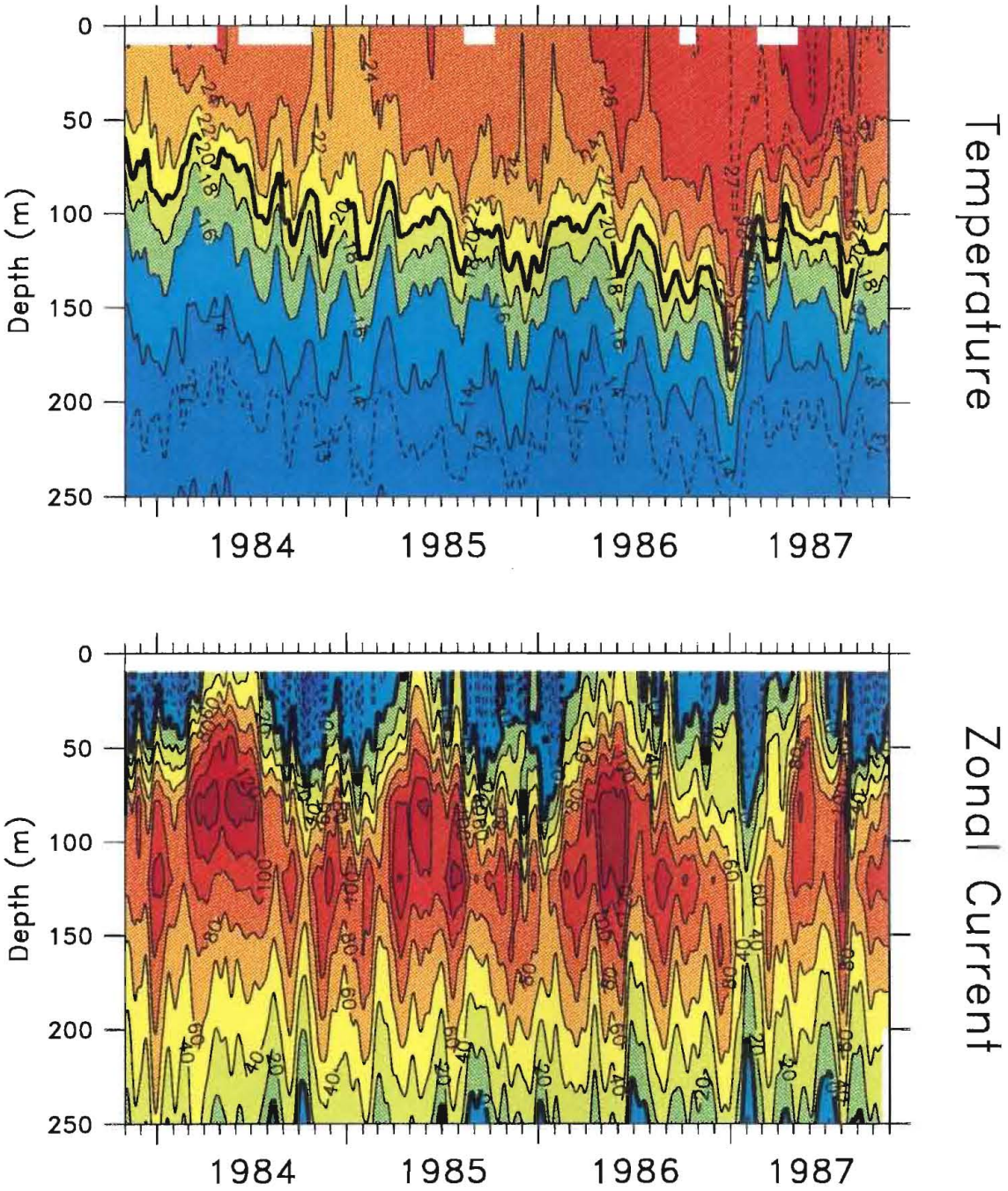

Figure 4.5. Time series measurements of a) temperature and b) zonal current velocity at 0°, 140°W for the period November 1983 - October 1987. These plots were computed from daily mean values which were then smoothed using a 17-day triangular low-pass filter.

3. Subsurface Velocity

The subsurface zonal velocity field from 10 m to 250 m for the four-year study period is presented in Figure 4.5b. As with the subsurface temperature field, the data were smoothed with a 17-day triangular low-pass filter. The annual vertical migration of the EUC core, ranging from about 75 m during the boreal spring and summer months to about 120 m during fall and winter months, was observed to vary interannually as well. This annual cycle was also accompanied by an intensification during the spring/summer shoaling. During the 1984 cold episode, the spring/summer shoaling of the EUC core was more pronounced than during the other years. During the 1986/1987 ENSO warm episode, the usual fall/winter relaxation and deepening of the EUC core were particularly pronounced, with the EUC velocity reduced to as low as 25 cms^{-1} during January/February 1987. As observed in the subsurface temperature data, the zonal velocity experienced pronounced fluctuations at periods of 60-90 days, with peak amplitudes of about 20 cms^{-1}.

4. Buoyancy Frequency

Monthly mean fields of buoyancy frequency (N), velocity shear (S) and gradient Richardson Number (Ri) during November 1983 through October 1987 are contoured in Figures 4.6a-c. As with subsurface temperatures, N showed significant interannual variability associated with ENSO. A core of high N ($N > 0.014$ s^{-1}) was observed to follow the depths of the thermocline shown in Figure 4.5a. The core of high N, indicating strong stratification, was shallow (O(50 m)) during the 1984 cold event. During the ENSO build-up phase from late 1984 until early 1986, the high-N core slowly and steadily deepened from about 90 m to about 110 m, with monthly maxima ranging between 0.016 s^{-1} and 0.018 s^{-1}. During the 1986/1987 ENSO warm episode, the high-N core increased in magnitude to 0.022 s^{-1} and deepened abruptly in December 1986/January 1987 to about 150 m, apparently related to the passage of an intense equatorial Kelvin wave. Since these data consist of monthly means, 60-90 day intraseasonal fluctuations are not as readily apparent as in the subsurface temperature figure (Figure 4.5a). In addition to this progression of the high-N core, it is useful to examine the temporal variability of

the low-N, weakly stratified upper 50 m. At times when N was relatively high in the surface layer, indicating strong stratification, vertical turbulent mixing is expected to have been low. In early 1984, the upper ocean was well-stratified up to at least 10 m, and mixing rates would be expected to have been low. When N was low in the upper layer, such as during the 1986/1987 ENSO warm episode, increased vertical mixing is expected to have occurred.

5. Velocity Shear

The monthly mean values of the total vertical velocity shear contoured in Figures 4.4a-c include both zonal and meridional velocity components. As with zonal velocity (Figure 4.3b), velocity shear underwent significant interannual variability associated with ENSO. During early 1984, velocity shears in the upper 10-40 m associated with the shoaling of the EUC during the 1984 cold episode exceeded 0.03 s^{-1}. By June of 1984 the core of high velocity shear had weakened and deepened to about 0.02 s^{-1} and about 60 m, respectively. From November 1985 through January 1986 a pronounced peak in S was observed at 35 m, with a maximum S exceeding 0.03 s^{-1}. The November 1985 and January 1986 zonal velocity profiles show an unusual eastward acceleration of the flow at 45 m. During the 1986/1987 ENSO warm episode, the weakening of the EUC resulted in significant deepening and reduction in strength of the high-S core. The differences between S during the ENSO cold and warm episodes were large.

6. Richardson Number

As discussed in Chapter II, the gradient Richardson Number, Ri, is defined as the ratio of N^2 to S^2. Ri provides a measure of the dynamic stability of the water column. Figure 4.6c shows contours of the monthly mean values of $\log_{10}(Ri)$ over the four-year period of study. Since these values are 30-day averages of Ri's computed from 6-hour mean temperature and velocity profiles based on limited vertical resolution observations, it is expected that computed monthly mean Ri will be higher than that observed on microstructure scales. Each of the operations performed in computing these Ri values tends to smooth low Ri values. It is not unreasonable to assume that values of

Ri less than unity might represent conditions of marginal stability in a monthly mean sense (as opposed to a critical $Ri_{cr} = 0.25$ in a local sense). The heavy black contour line indicating a $\log_{10}(Ri) = 0.0$ corresponds to Ri equal to unity. The darker regions inside the $Ri = 1.0$ contour therefore represent regions having $Ri < 1$ and a possibility of marginal dynamic stability. The dashed contours inside the darkly shaded region represent Ri contours of 0.63, 0.40, and 0.25, respectively.

As one would expect, Ri contours exhibit a pattern of ENSO interannual variability similar to that observed for N and S. Since this study is concerned with relationships between the diurnal variability of high-frequency waves and turbulent mixing by dynamic instabilities, increased attention is given to low-Ri regions above the EUC. The low-Ri region underwent an annual deepening during the boreal winter months down to about 100 m and a shoaling during the boreal summer months. The low-Ri core appeared to shoal to depths above 40 m during the 1984 cold episode, or about 35 m shallower than usual. During the 1986/1987 warm episode, the low-Ri region disappeared as the weakening of the EUC decreased the S to small values.

Each of the Figures 4.6a-c has the symbols TH1 and TH2 along the upper time axis to indicate the times of the TROPIC HEAT 1 and TROPIC HEAT 2 microstructure measurements. It is noteworthy that the two sampling periods were characterized by largely different oceanic conditions, as represented by N, S, and Ri. Furthermore, these figures indicate that considerable oceanic variability occurs at 0°, 140°W, and it is not unreasonable to expect corresponding variability of the diurnal cycle of high-frequency temperature variability.

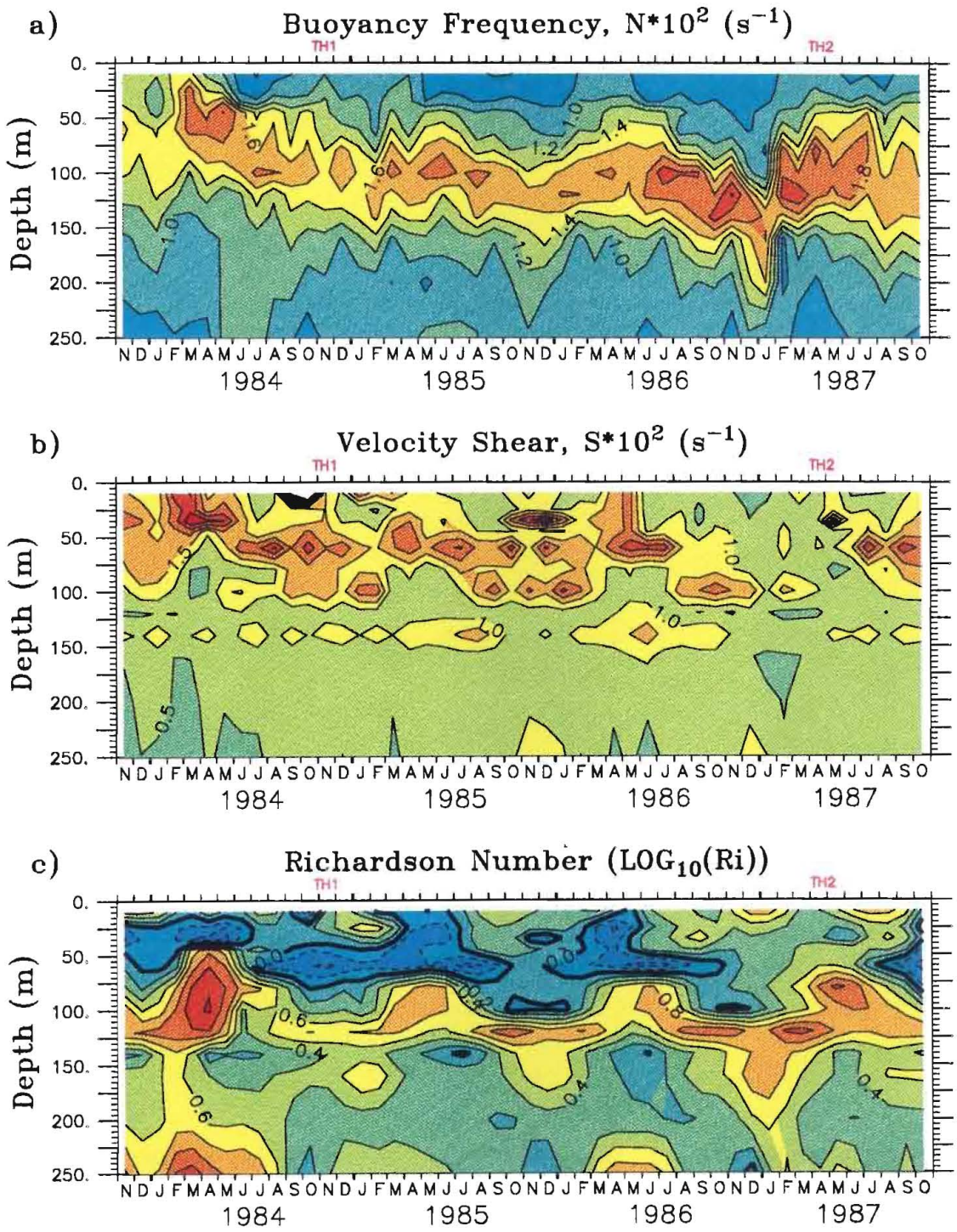

Figures 4.6a-c. Time-depth contour plots of monthly mean values of a) buoyancy frequency, *N* b) velocity shear, *S* and c) gradient Richardson number, *Ri*, from 10 m to 250 m over the period November 1983 - October 1987. TH1 and TH2 at the top of each plot indicate the approximate time of the TROPIC HEAT experiment microstructure measurements.

7. Mixed Layer

Mixed-layer depth is related, directly or indirectly, to each of the observed forcing or background conditions discussed above. Monthly mean estimates of mixed-layer depth for each of the four six-hour time bins are presented in Figure 4.7a. These mixed-layer depths were computed as the depth where the vertical temperature gradient first reached $0.01 Cm^{-1}$. Although the 10-15 m vertical instrument spacing limits the accuracy of these estimates, the diurnal variations were consistent throughout the record and agree with diurnal variations of mixed-layer depth computed using higher resolution data. Monthly means of the maximum diurnal ranges in mixed-layer depth, i.e., difference between daily maximum and minimum mixed-layer depths among the four time bins, are presented in Figure 4.7b. These figures show considerable interannual variability in both mixed-layer depth and the diurnal range of mixed-layer depth superimposed over the annual cycle. The nighttime mixed-layer depth had a mean of 31.8 m and a standard deviation of 15.1 m. The daytime mixed-layer depth had a mean of 23.1 m and a standard deviation of 13.7 m.

During the 1984 ENSO cold episode, mixed-layer depth was shallow, averaging about 20 m for the period November 1983 through May 1984. During this period, the diurnal range in mixed-layer depth was similarly very small (O(5 m)). Following this cold episode, mixed-layer depths and diurnal ranges of mixed-layer depths progressively increased through the ENSO build-up phase. After a period of shoaling between February 1986 and April 1986, mixed-layer depths deepened significantly during the 1986/1987 ENSO warm episode. The diurnal range of mixed-layer depths followed a similar progression.

Since surface layer mixing processes are possibly related to high-frequency temperature variability in the thermocline, statistical relationships between the monthly mean surface forcing and background oceanic conditions and mixed-layer depths are examined. Of the fourteen surface forcing variables examined, monthly mean mixed-layer depths were significantly correlated at the 95% confidence level only with wind speed, zonal wind, meridional wind (for day and evening time bins only), latent heat flux (evaporation), net surface heat flux, and net surface buoyancy flux (Table 4.1). For these

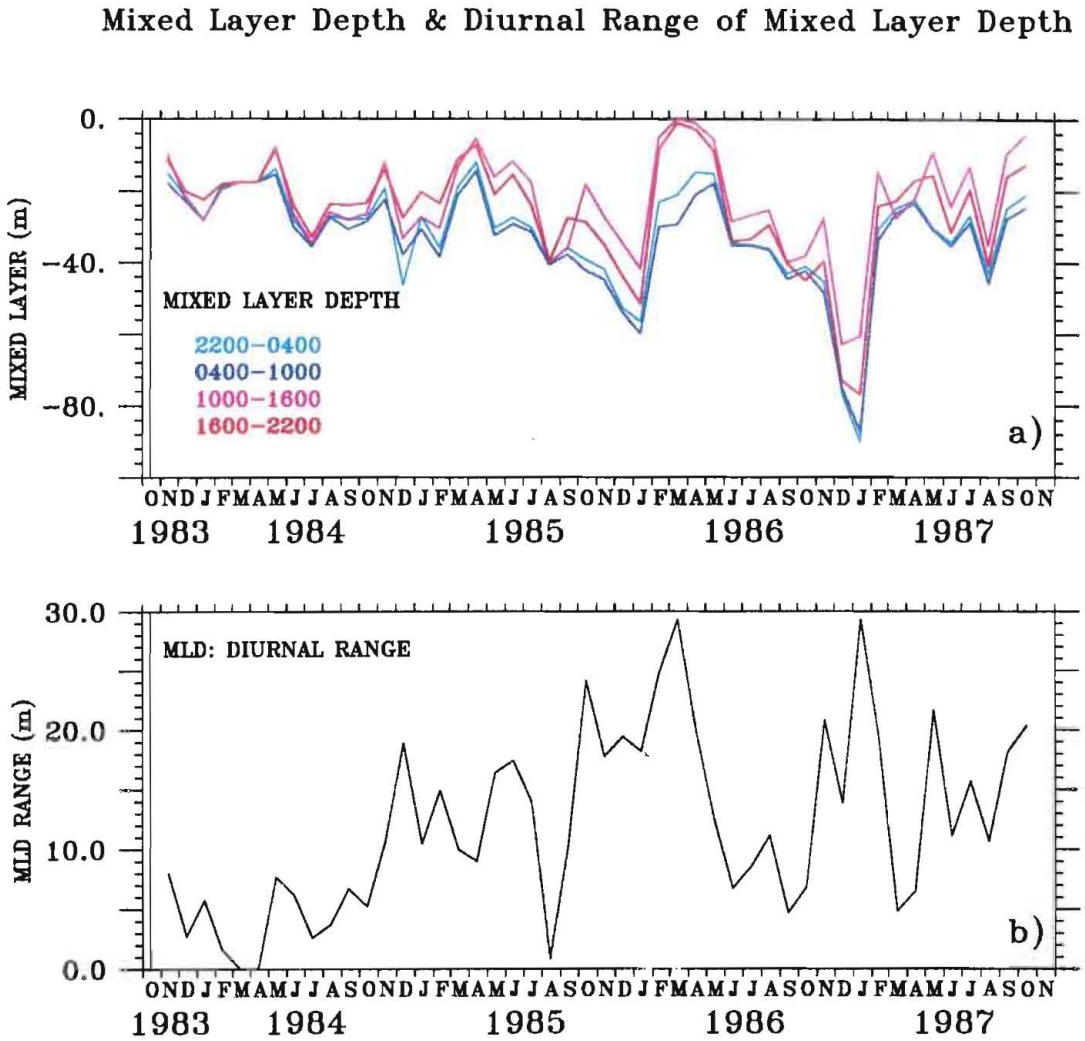

Figure 4.7. Time series of monthly mean values of a) mixed-layer depth and b) diurnal range of mixed-layer depth over the period November 1983 - October 1987. Mixed-layer depths are given for each of the four 6-hour time bins: 2200-0400, 0400-1000, 1000-1600, and 1600-2200.

calculations, mixed-layer depths were negative.

The strong correlations with wind speed and zonal wind, about -0.51 and 0.51, respectively, indicate that mechanical energy input into the mixed layer by wind forcing plays a significant role in mixing the surface layer at 0°, 140°W. The sign of the correlations indicate that increased local wind stress deepened the mixed layer. It is interesting to point out that over larger spatial scales, increased easterlies along the equator drive Ekman pumping, which would raise the thermocline and result in shallower mixed-layer depths. Meridional winds, which were typically weaker than the zonal winds (Figure 4.1), were significantly correlated with the day and evening mixed-layer depths, but were not significantly correlated with the night and morning mixed-layer depths. This diurnal difference of the correlations could be explained by the diurnal cycle of meridional winds reported by Deser (1994). Her analysis of the diurnal cycle of winds over the equatorial Pacific indicated diurnal meridional wind variations of about 0.6-0.8 ms^{-1} at most locations, with southward anomalies of the flow at night. Since the meridional winds at 0°, 140°W were usually northward during this four-year period of study, southward anomalies of the flow at night indicate a deceleration, which could translate into decreased nighttime input of mechanical energy by the meridional wind. An alternative, or perhaps complementary, explanation for the decreased correlation between the meridional winds and the nighttime mixed-layer depth could be that the weaker nighttime meridional winds do not penetrate to the deeper nighttime mixed-layer depth. By this hypothesis, the daytime mixed layer was sufficiently shallow to be affected by the stronger daytime meridional winds.

Of the terms of the surface heat flux, only latent heat flux, Q_e, and the net surface heat flux, Q_{net}, were significantly correlated with the monthly mean mixed-layer depths. The positive correlations with Q_{net} and Q_e indicate that the mixed-layer deepened during periods with increased net and latent heat loss from the ocean surface. In both cases, surface heat loss drives convective mixing and mixed layer deepening. On these monthly time scales, Q_s, Q_h, and Q_b were not well correlated with mixed-layer depths. It is noteworthy that the largest term of the surface heat flux, Q_s, was not well

correlated with mixed-layer depth on monthly time scales. In section 4.3.2, on the other hand, good correspondence between mixed-layer depth and Q_s are observed on seasonal time scales.

Table 4.1. Correlation coefficients, r, between monthly mean mixed-layer depths for each of the four 6-hour time bins and surface forcing variables during November 1983 - October 1987. Statistical significance at the 95% confidence level was calculated using computed integral time scales between time series to determine independence of data points (Davis, 1976). Statistically significant correlations are indicated by **Bold** type.

VARIABLE	2200-0400		0400-1000		1000-1600		1600-2200	
	95%c.i.	r	95%c.i.	r	95%c.i.	r	95%c.i.	r
Wind Speed	**.411**	**-.511**	**.424**	**-.524**	**.389**	**-.511**	**.416**	**-.510**
Zonal Wind	**.421**	**.508**	**.436**	**.525**	**.396**	**.487**	**.425**	**.486**
Merid. Wind	.486	-.377	.501	-.360	**.457**	**-.508**	**.484**	**-.505**
Wind Dir.	.467	-.237	.484	-.226	.438	-.365	.461	-.352
Q_s	.485	-.100	.491	-.177	.448	-.060	.482	-.057
Q_e/E	**.369**	**.438**	**.384**	**.454**	**.361**	**.440**	**.373**	**.513**
Q_h	.419	.156	.429	.184	.412	.078	.420	.098
Q_b	.398	.202	.405	.158	.405	.274	.406	.251
Q_{net}	.389	.388	.386	.349	**.362**	**.420**	**.389**	**.486**
P	.315	.060	.316	.066	.308	-.078	.316	.027
$E - P$	.330	-.244	.339	-.262	.322	-.224	.333	-.318
$B_{moisture}$	.320	.134	.330	.158	.315	.005	.318	.106
B_{net}	.319	.275	.317	.272	.314	.286	**.322**	**.331**

Comparison between monthly mean mixed-layer depth (Figure 4.7a) and monthly mean buoyancy frequency (Figure 4.6a) shows considerable correspondence. When the high-N core was shallow, such as during the 1984 cold episode, the mixed layer was likewise shallow. Similarly, when the high-N core was deep, the mixed layer was deep. In other words, the correspondence between monthly mean mixed-layer depths and N largely reflects the fact that large-scale vertical displacements of the thermocline lead to changes in mixed-layer depth, as defined here, through mass conservation, an adiabatic process that requires no mixing.

The correlation between monthly mean mixed-layer depths and N in the upper 100 m for each of the four six-hour time bins are given in Table 4.2. Statistically significant positive correlation was observed between mixed-layer depth and N at the depths between 35 m and 80 m for all four time bins, and at 25 m and 100 m during the night time bin. As described above, the positive correlations indicate that on monthly time scales the mixed-layer depth shallowed when the stratification increased. It is noteworthy that correlations were consistently stronger during the night and morning time bins, perhaps suggesting a more direct relationship between mixing and stratification at times when active convective mixing was occurring than during times of restratification.

Significant positive correlations were observed between monthly mean mixed-layer depth and velocity shear at 25 m and 45 m during all four time bins, and velocity shear at 35 m during the day time bin (Table 4.3 and Figure 4.8). This depth range of significant correlations coincides with the typical depth of the mixed layer. The positive sign of the correlations indicates that increased shear was observed during times when the mixed-layer was relatively shallow and vice versa. Furthermore, correlations in this depth range increased during the day time bin, when the mixed layer was diurnally-shallowest and generally above this depth range. These results imply increased shear at the base of the mixed layer. when the mixed layer was deep, momentum in the mixed-layer was well-mixed and shear was reduced. When the mixed layer was shallow, momentum was not well-mixed, and shear was high. On these monthly and diurnal time scales, mixing apparently worked to deepen the mixed layer and decrease the shear.

Table 4.2. Correlations coefficients, r, between monthly mean mixed-layer depths for the four 6-hour time bins and buoyancy frequency in the upper 100 m during November 1983-October 1987. Statistical significance at the 95% confidence level was determined based on integral time scales between time series (Davis, 1976). Statistically significant correlations are indicated by **Bold** type.

VARIABLE	2200-0400		0400-1000		1000-1600		1600-2200	
	95%c.i.	r	95%c.i.	r	95%c.i.	r	95%c.i.	r
N at 010m	.425	.339	.430	.312	.414	.348	.449	.344
N at 025m	**.412**	**.417**	.415	.410	.365	.320	.400	.352
***N* at 035m**	**.388**	**.526**	**.397**	**.545**	**.355**	**.439**	**.380**	**.432**
***N* at 045m**	**.429**	**.505**	**.463**	**.559**	**.415**	**.429**	.431	.427
***N* at 060m**	**.445**	**.562**	**.480**	**.620**	**.429**	**.466**	**.446**	**.480**
***N* at 080m**	**.417**	**.641**	**.464**	**.688**	**.420**	**.560**	**.408**	**.619**
***N* at 100m**	**.379**	**.422**	.392	.390	.348	.316	**.363**	**.401**

Table 4.3. Correlations coefficients, r, between monthly mean mixed-layer depths for the four 6-hour time bins and velocity shear in the upper 100 m during November 1983-October 1987. Statistical significance at the 95% confidence level was determined based on integral time scales between time series (Davis, 1976). Statistically significant correlations are indicated by **Bold** type.

VARIABLE	2200-0400		0400-1000		1000-1600		1600-2200	
	95%c.i.	r	95%c.i.	r	95%c.i.	r	95%c.i.	r
S at 010m	.356	.209	.344	.181	.337	.105	.347	.167
***S* at 025m**	**.398**	**.549**	**.410**	**.546**	**.404**	**.618**	**.397**	**.478**
***S* at 035m**	.357	.269	.346	.255	**.372**	**.439**	.371	.256
***S* at 045m**	**.400**	**.663**	**.418**	**.669**	**.402**	**.686**	**.396**	**.634**
S at 060m	.400	.210	.423	.237	.407	.272	.410	.263
S at 080m	.450	.059	.457	.064	.419	.089	.432	.122
S at 100m	.480	-.334	.500	-.411	.450	-.387	.480	-.330

Correlations between monthly mean mixed-layer depths and Richardson number in the upper 100 m were generally weak (Table 4.4 and Figure 4.8). Statistically significant correlations were found only with *Ri* in the upper 45 m, and only for specific time periods. At 10 m, significant correlation was observed only during the night time bin, when the mixed layer was deep. At 25 m, significant correlations were observed during the night, morning, and evening time bins, with the largest correlation, -0.595, occurring during the evening time. At 45 m, significant correlation was observed only for the evening time bin. The sign of each of the significant correlations was negative indicating that the mixed layer was relatively deep during times when *Ri* in the upper 45 m was high, and vice versa. This reflects the fact that when the mixed layer was deep, mixing of momentum, and to a lesser extent heat, resulted in increased *Ri*.

Table 4.4. Correlations coefficients, r, between monthly mean mixed-layer depths for the four 6-hour time bins and gradient Richardson Number in the upper 100 m during November 1983-October 1987. Statistical significance at the 95% confidence level was determined based on integral time scales between time series (Davis, 1976). Statistically significant correlations are indicated by **Bold** type.

VARIABLE	2200-0400 95%c.i.	r	0400-1000 95%c.i.	r	1000-1600 95%c.i.	r	1600-2200 95%c.i.	r
***Ri* at 10m**	**.334**	**-.369**	.320	-.317	.317	-.133	.298	-.181
***Ri* at 25m**	**.391**	**-.447**	**.403**	**-.499**	**.399**	**-.595**	.396	-.343
***Ri* at 35m**	.347	-.216	.362	-.243	**.377**	**-.461**	.353	-.243
***Ri* at 45m**	.308	-.254	.346	-.336	**.318**	**-.379**	.287	-.164
Ri at 60m	.381	.070	.398	-.062	.372	-.047	.398	-.037
Ri at 80m	.489	.269	.496	.270	.461	.199	.468	.199
Ri at 100m	.528	.490	.542	.523	.499	.445	.526	.413

The above relationships between monthly mean mixed-layer depths and N, S, and Ri in the upper 100 m are summarized in Figure 4.8. In these figures, the heavy green dashed lines represent the four-year mean nighttime and daytime mixed-layer depths. The green dotted lines represent the uppermost and lowermost standard deviations about the respective mean mixed-layer depths. Figure 4.8a graphically shows that mixed-layer depths are significantly correlated with N at depths well below the mixed layer. These correlations below the base of the mixed layer and the comparison between monthly mean N (Figure 4.6a) and mixed-layer depths (Figure 4.7a) suggest that these correlations are probably more related to the large-scale dynamics responsible for the vertical migrations of the thermal structure than by local mixing processes. The relationships with S and Ri, on the other hand, are strong only near the base of the mixed-layer, suggesting the possibility of local forcing.

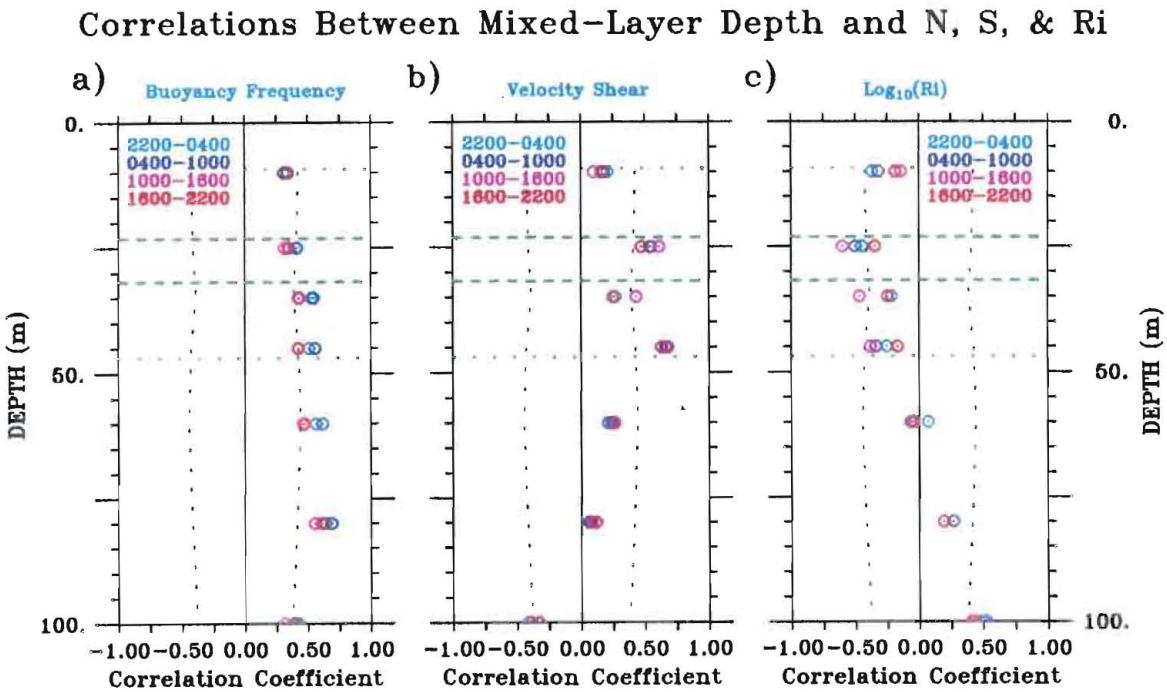

Figure 4.8. Correlation coefficients, r, between monthly mean mixed-layer depths and buoyancy frequency, *N*, velocity shear, *S*, and gradient Richardson number, *Ri*, in the upper 100 m during November 1983-October 1987. Dotted black vertical lines represent 95% confidence intervals determined using an integral time scale between time series (Davis, 1976). Dashed heavy green lines indicate four-year mean daytime (upper) and nighttime (lower) mixed-layer depths. Dotted green lines indicate upper and lower bounds of the standard deviations about the respective mean mixed-layer depths.

C. SEASONAL CYCLES

In the previous section, monthly mean time series of several surface forcing and oceanic background condition variables were presented and discussed in terms of their interannual variability. In several of those discussions, annual cycles were observed and in some instances briefly mentioned. In this section, seasonal cycles of many of these variables are examined. Generally, seasonal cycles were computed as means of monthly means for each calendar month from all of the months with available data during the period November 1983 through October 1987.

1. Surface Forcing

Climatological seasonal cycles of wind speed, zonal wind, and meridional wind are shown as dotted lines in Figure 4.1. These were computed from all of the available buoy data during 1983-1991 (McPhaden and McCarty, 1992). The seasonal cycle of the relatively weak meridional winds varied from a minimum near zero during February and March to a maximum of about 1.5 ms^{-1} during August and September. The seasonal cycle of zonal winds ranges from a minimum easterly of about -4.8 ms^{-1} in May to a maximum easterly of about -6.8 ms^{-1} in December and January. The seasonal cycle of wind speed is dominated by the zonal component with minima during the boreal spring between March and June and maxima during the boreal winter between October and February. Each of the wind components and wind speed show a weak semi-annual cycle indicated by a weak maximum or leveling-off of wind speed during the boreal summer months August through October.

Climatological seasonal cycles of the surface heat flux terms are presented as dotted lines in Figures 4.2a-e. The Oberhuber (1988) climatology was used for the seasonal cycles of Q_b, Q_h, and Q_e. Longwave radiation has a annual maximum magnitude of about -58 Wm^{-2} during the boreal fall between October through December and a minimum magnitude of about -48 Wm^{-2} during the boreal spring between March and May. The climatological seasonal cycle of the sensible heat flux varies by only about 3-4 Wm^{-2}. The estimates of Q_h show an annual minimum of about -5 Wm^{-2} during the winter and a maximum of about +4 Wm^{-2} during the spring and summer. These seasonal cycles of Q_h are probably too small and variable to play a significant role in modulating the

seasonal cycles of convective mixing or high-frequency temperature variability in the thermocline. The seasonal cycle of latent heat flux, on the other hand, shows a pronounced annual cycle with a broad maxima of about -115 Wm^{-2} during the boreal summer and fall and a minimum of about -75 Wm^{-2} from February through April.

The seasonal cycle of shortwave radiation is presented as the dotted line in Figure 4.2d. This was computed using the formula of Reed (1977) and COADS cloud data and buoy data for the period 1983-1992. A pronounced semi-annual cycle was observed in response to the semi-annual cycle of the ecliptic. Asymmetric shortwave radiation minima occur about the time of the solstices in June/July and November/December and maxima occur during the equinoxes in March and September. The minimum in June/July is about 232 Wm^{-2} compared with the November/December minimum of about 248 Wm^{-2}. The September maximum reaches about 273 Wm^{-2} compared to the March maximum of about 272 Wm^{-2}. The seasonal cycle of the data during the four-year study period had a similar pattern, but the magnitudes were about 30 Wm^{-2} greater.

The seasonal cycle of the net surface heat flux was computed from the seasonal cycles of the four component terms and is presented as the dotted line in Figure 4.2e. The seasonal cycle of Q_{net} is characterized by an asymmetric semi-annual cycle with minimum values of 54.1 and 83.3 Wm^{-2} occurring in July and December, respectively, and maximum values of 143.7 and 100.8 Wm^{-2} occurring in March and September, respectively. The annual climatological mean is 99.1 Wm^{-2} and the standard deviation is 25.6 Wm^{-2}. The estimated Q_{net} had a significantly greater mean of 154.5 Wm^{-2} and a standard deviation of 29.7 Wm^{-2}.

The seasonal cycle of the moisture flux (Figure 4.4) is characterized by a pronounced annual cycle with a maximum during February and March and a minimum during July through September. This annual cycle is closely related to the seasonal cycle of precipitation presented in Figure 3.8. Since the net surface buoyancy flux was strongly dominated by the net surface heat flux, the seasonal cycle of B_{net} is almost identical to that described for Q_{net}.

2. Mixed Layer

The seasonal cycles of mixed-layer depth for each of the four six-hour time bins and the diurnal range of mixed-layer depth are shown in Figure 4.9. As with surface winds and shortwave radiation, both mixed-layer depth and the diurnal range of mixed-layer depth exhibited a weak semi-annual cycle and a pronounced annual cycle. Mixed-layer depths were deepest during the boreal winter months December and January, when the nighttime mixed layer deepened to about 50 m. Mixed-layer depths were shallowest during the boreal spring months March through May, when the nighttime mixed layer penetrated to a depth of only about 20 m. For the period between June and November, nighttime mixed-layer depths remained relatively stable at about 35 m. The seasonal cycles of mixed-layer depth and surface wind speed were in close agreement, with deep mixed layers occurring during the boreal winter months when wind speeds reached their annual peak. This strong relationship between increased mixing during periods of increased wind speed are not unique to this region and have been observed and modelled frequently. The semi-annual period of the mixed layer corresponds with the semi-annual period of Q_s, with a shallow mixed layer during the boreal spring and fall when Q_s reached semi-annual maximum values. This relationship implies that increased shortwave radiation increases the stratification and reduces convective mixing. Since Q_{net} and B_{net} include this semi-annual cycle of Q_s, their seasonal cycles also correspond with the seasonal cycle of the mixed layer.

The seasonal cycle of the diurnal range of mixed-layer depth was also characterized by a semi-annual cycle. Maximum diurnal ranges of 14-16 m occurred during the boreal winter months October through February and again during May. Minimum diurnal ranges of 7-11 m occurred during March and April and again during July through September. The large diurnal ranges observed during the winter corresponds with higher winter winds. The semi-annual cycle was not clearly related to the semi-annual cycle of Q_s.

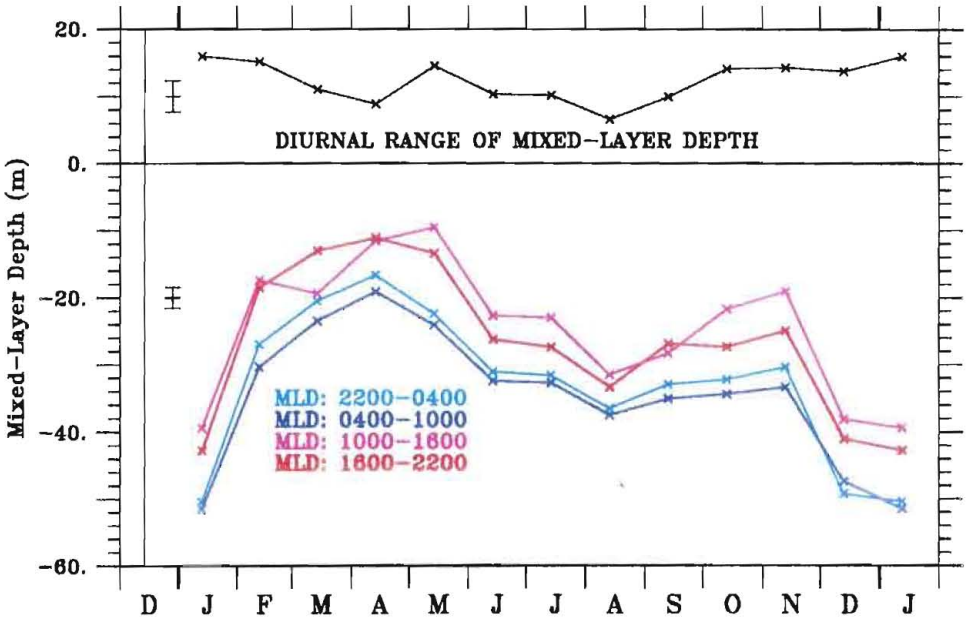

Figure 4.9. Seasonal cycles of mixed-layer depth for four six-hour time bins and diurnal range of mixed-layer depth. Computed from monthly means during the period November 1983-October 1987. Black vertical lines represent ±one mean standard error of the mean computed from 48 monthly standard errors for the mixed-layer depth and 12 standard errors for the diurnal range of mixed-layer depth.

3. Buoyancy Frequency

The seasonal cycles of buoyancy frequency, N, zonal velocity, U, velocity shear, S, and Richardson number, Ri, over the depth range 10-250 m are contoured in Figure 4.10. The seasonal cycle of N in the upper 50 m (Figure 4.10a) reflected a relation to the seasonal cycle of the mixed-layer depth (Figure 4.9). During the boreal spring, when the mixed layer was shallow, N increased to above 0.01 s^{-1} in the upper 25 m and above 0.012 s^{-1} between 25 m and 50 m. For the remainder of the year, when the nighttime mixed layer extended down to at least 35 m, N in the upper 35 m or so remained less than 0.01 s^{-1} and between May and September N was less than 0.008 s^{-1} in the upper 25 m.

The high-N core associated with the depth of the thermocline migrated vertically during the year from a maximum depth during the boreal winter of about 125 m to a minimum depth of about 100 m during the boreal spring. The magnitude of the high-N core varied during the year from about 0.015 s^{-1} in January to over 0.018 s^{-1} from June through September. The vertical gradient of N underwent noteworthy seasonal variations with strong gradients observed between the mixed layer and thermocline core (25-75 m) during the period May through September and weak vertical gradients during the boreal winter. These weaker vertical gradients of N during the winter correspond with the deepening of the mixed layer.

4. Zonal Velocity

The seasonal cycle of zonal velocity, U, over the depth range 10-250 m is contoured in Figure 4.10b. The most striking feature of the seasonal cycle of U is the annual vertical migration and intensification of the EUC. During boreal spring and early summer, the eastward EUC core intensified in strength to over 1.2 ms^{-1} and shoaled to typical depths of about 85 m. This shoaling of the EUC often extended to the surface, where weak eastward currents existed during May and June. By July, the EUC began to deepen and reduce in strength. During the boreal winter, the EUC core was generally centered at a depth of about 125 m and had a reduced strength of less than 1.0 ms^{-1}. From July through March, the surface velocities were westward at mean speeds between 0.2 and

0.4 ms^{-1}. This westward surface flow was part of the large-scale SEC driven by the easterly winds at the surface.

5. Velocity Shear

The seasonal cycle of velocity shear over the depth range 10-250 m is contoured in Figure 4.10c. This figure shows correspondence with the zonal velocity contour plot, eventhough shear is based on both zonal and meridional velocity. As observed for zonal velocity, shear underwent noteworthy seasonal variations. The high-shear core migrated vertically from about 80-90 m during the boreal fall and winter months to about 35-45 m during the boreal spring. While shear between the surface and the EUC core was always relatively strong with values exceeding -0.012 s^{-1} throughout the year, maximum shears exceeding -0.020 s^{-1} occurred during the boreal summer months when the EUC core was shallow, but beginning to deepen, and the strength was intensified. In April and May, when the EUC was strongest and extended to the surface, maximum shears of -0.020 s^{-1} occurred at about 35 m. During June through August, when the EUC had begun to deepen and the SEC surface westward flow had returned, maximum shears of -0.024 s^{-1} occurred at about 60 m. During the boreal winter months, when easterly winds were strongest, the mixed layer was deepest, and the EUC was weaker and deeper, the shear was about -0.012 s^{-1} from about 30 m to about 100 m.

Below the EUC core, maximum shears of over 0.012 occurred from May through October at a depth of about 140 m. During the boreal winter months, the shear below the EUC was reduced to values near 0.004 s^{-1}.

The relatively weak shear observed below the EUC core might have been partially reduced by the poor vertical resolution of current meters at these depths. The comparison between shears computed from ADCP measurements with 8 m vertical resolution and those used here which was discussed in section 3.2.3 showed considerable underestimates of shear at depths between 140 m and 180 m.

6. Richardson Number

The seasonal cycle of *Ri* over the depth range 10-250 m is contoured in Figure 4.10d. As discussed in section 4.1.2, the averaging operators used in computing monthly mean *Ri* have the effect of increasing low-*Ri* values. In computing seasonal

cycles of *Ri*, this effective smoothing was repeated and mean seasonal values in low-*Ri* regions were increased. The seasonal cycle of *Ri* shows the expected similarity with the seasonal cycle of shear. Minimum values of *Ri* coincided with maximum values of shear. During the period March through June, when the mixed-layer was shallow, mean *Ri* at 35 m was less than unity, with minimum values near 0.5. This low-*Ri* region deepened to about 60 m from July through October with mean values of 0.5 for much of this time. This deepening coincided with a deepening of the seasonal mixed-layer of about 20 m. During the periods when *Ri* was near 0.5, the vertical extent of the low-*Ri* core was noticeably reduced, typically to depth ranges of about 25 m. During the boreal winter months, when mean *Ri* in the low-*Ri* core was typically slightly greater than unity, the vertical extent of the low-*Ri* core appeared greater. The high-*Ri* core appeared to follow the low-shear contour of Figure 4.10c. The low-*Ri* core below the EUC core had a minimum of about 2.0 centered at about 140 m during the months April through July. These relatively high values of *Ri* in the low-*Ri* core were probably overestimates due to the likely underestimates of shear at these depths.

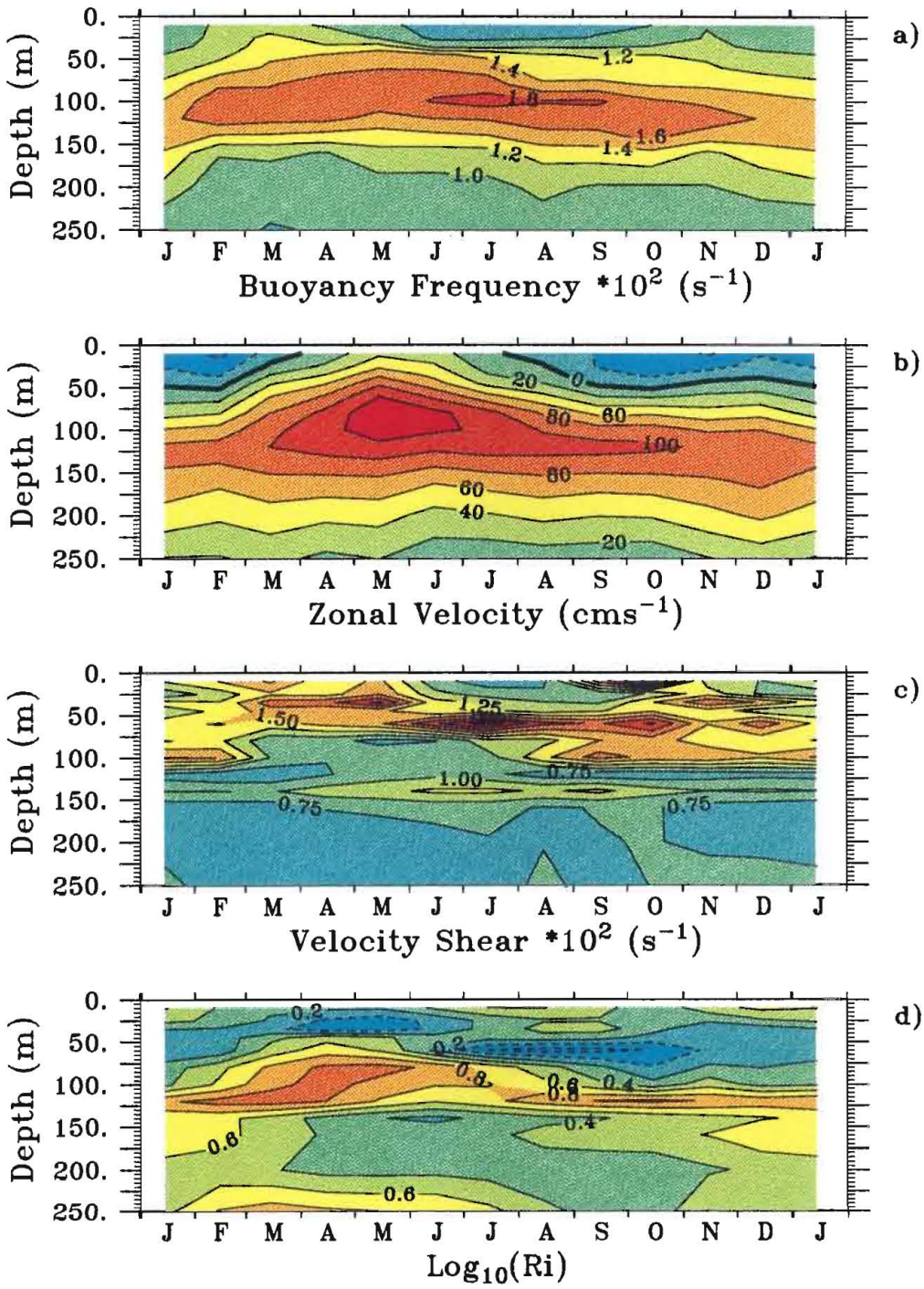

Figures 4.10. Time-depth contour plots of seasonal cycles of a) buoyancy frequency, N, b) zonal velocity, U, c) velocity shear, S, and d) Richardson number, Ri, at 0°, 140°W over the depth range 10-250 m. Computed from monthly mean values during November 1983-October 1987. Contour intervals are a) 0.2 x 10^{-2} s^{-1}, b) 20 cms^{-1}, c) 0.25 x 10^{-2} s^{-1}, and d) 0.2.

V. ISOTHERM DISPLACEMENT VARIANCE

A. ISOTHERM DISPLACEMENT VARIANCE

The primary objective of this study is to characterize the diurnal variability of high-frequency wavelike motions. The indicator high-frequency motions used in this investigation is isotherm displacement variance (IDV), which is interpreted as some combination of high-frequency internal waves, local Kelvin-Helmholtz shear instabilities, and local turbulence. In the following five sections, IDV will be discussed in terms of its interannual and seasonal variability, and the relationships with the observed surface forcing and dynamic stability.

B. INTERANNUAL VARIABILITY OF IDV

This section focuses on the interannual variability of IDV during the period November 1983 through October 1987. Monthly mean values of IDV at the depths 35 m, 60 m, 100 m, 140 m and 200 m for each of the four six-hour time bins are presented in Figures 5.1a-e. IDV at 35 m varied substantially over interannual time scales (Figure 5.1a). During the 1984 ENSO cold episode, IDV at 35 m was low, with values averaging about 2-3 m^2, corresponding to vertical isotherm displacements of about 1.5 m. Beginning in the fall of 1984, a trend of increasing IDV at 35 m was observed, which was particularly apparent during the night and morning time bins. By the winter of 1985/1986, typical values of IDV at 35 m averaged about 7-8 m^2, corresponding to vertical isotherm displacements of about 2.5 m. This trend was superimposed over an annual cycle with minima typically occurring during the boreal spring. Following the annual minimum in the spring of 1986, IDV at 35 m increased sharply to values as high as 17 m^2 during the boreal winter months, corresponding to vertical isotherm displacements exceeding 4 m. The nighttime increases of IDV at 35 m were particularly pronounced during periods of relatively high IDV and diminished during periods of low IDV. It is noteworthy that

periods of low IDV at 35 m occurred when stratification at 35 m was strong, and vice versa.

Due to three large data gaps of 5-6 months, the time series of IDV at 60 m is not ideally suited to investigating interannual or seasonal variability (Figure 5.1b). Nevertheless, significant variations on these time scales were apparent. Typical values of IDV at 60 m were about 4 m^2, with vertical isotherm displacements of about 2 m. There was a noteworthy reduction in IDV at 60 m during the later half of the 1986/1987 ENSO warm episode. Between February and October 1987, IDV at 60 m averaged less than 2 m^2. During this period and during the winter of 1984 diurnal variations of IDV at 60 m were not observed.

At 100 m, which was typically near the high-N core of the thermocline, IDV amplitudes were greater than at 35 m, 60 m, 140 m, and 200 m (Figure 5.1c). Only at 300 m was IDV greater than at 100 m, possibly due to the required use of first differences, rather than centered differences, in computing the vertical temperature gradient used to normalize the temperature variances. Interannual variations of IDV at 100 m are apparent. During the 1984 cold episode, IDV at 100 m was high, with an average of about 10 m^2. During this period, IDV at 100 m exhibited strong oscillations having a period of about 4 months and an amplitude of about 5 m^2. Throughout 1985 and into the spring of 1986, the average IDV decreased to about 5-6 m^2, with oscillations having a period of about 5-7 months and weaker amplitudes of about 2 m^2. During the boreal winter of 1986/1987, IDV at 100 m increased to about 10 m^2. Generally, diurnal variations of IDV at 100 m were less apparent.

At 140 m, which was typically below the high-velocity core of the EUC and below the high-N core of the thermocline, magnitudes of IDV were less than at 100 m, with values averaging about 6 m^2 (Figure 5.1d). An exception occurred during the 1984 ENSO cold episode, when IDV at 140 m averaged only 1.5 m^2. Aside from this period of low IDV, interannual variations of IDV at 140 m were not pronounced. No consistent pattern of diurnal variations of IDV at 140 m were observed.

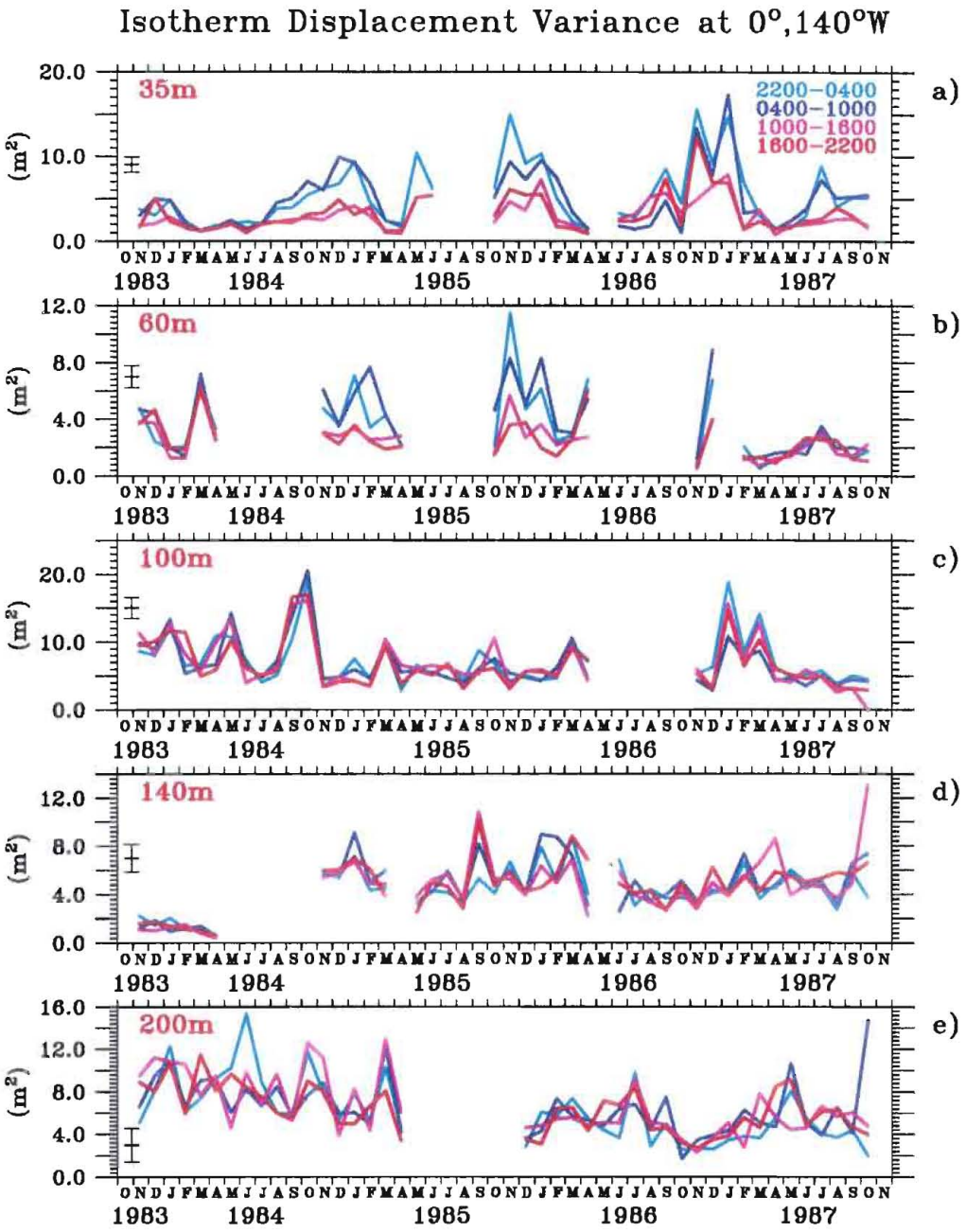

Figure 5.1a-e. Monthly mean isotherm displacement variance (IDV) at 5 depths for the period November 1983-October 1987 at 0°, 140°W: a) 35 m, b) 60 m, c) 100 m, d) 140 m, and e) 200 m. Gaps in each record are periods of no data or data of questionable quality. Error bars indicate the mean standard error of the mean for all time bins over the entire record length. Units are m^2.

At 200 m, where both the strength of S and N were typically weak (Figure 5.1e), IDV exhibited subtle variability on interannual time scales not easily identified as ENSO-related. For the first 18 months of the record, IDV at 200 m displayed a weak downward trend with an average IDV of about 8 m^2. Following a seven-month data gap, the final two years of data reveal a noteworthy oscillation of IDV at 200 m with an annual period. The average values of IDV during this period varied between about 4 m^2 during the boreal winters and about 6 m^2 during the boreal springs. No consistent pattern of diurnal variability of IDV at 200 m was observed.

Although IDV was computed at 300 m, lack of confidence in the vertical temperature gradient calculation and the strong sensitivity of IDV to this calculation rendered it questionable. Weak temperature gradients produced large monthly mean IDV values in the range 15-40 m^2. These large IDV values were accompanied by large standard errors. No consistent pattern of diurnal variability of IDV at 300 m was observed.

To summarize the vertical structure of IDV over the four-year study period, Figure 5.2 shows the mean vertical profiles of IDV for each of the four six-hour time bins computed from the monthly mean IDV values during November 1983 through October 1987. The mean IDV at 35 m and 60 m is highest during the morning time bin. The mean IDV at 35 m is lowest during the evening time bin and the mean IDV at 60 m is lowest during the day time bin. Generally, IDV in the upper 60 m is higher during the nighttime and lower during the daytime. A striking feature of the mean vertical structure of IDV is the high variability of the mean at 35 m and 60 m compared with the low variability of the mean IDV at 100 m, 140 m, and 200 m.

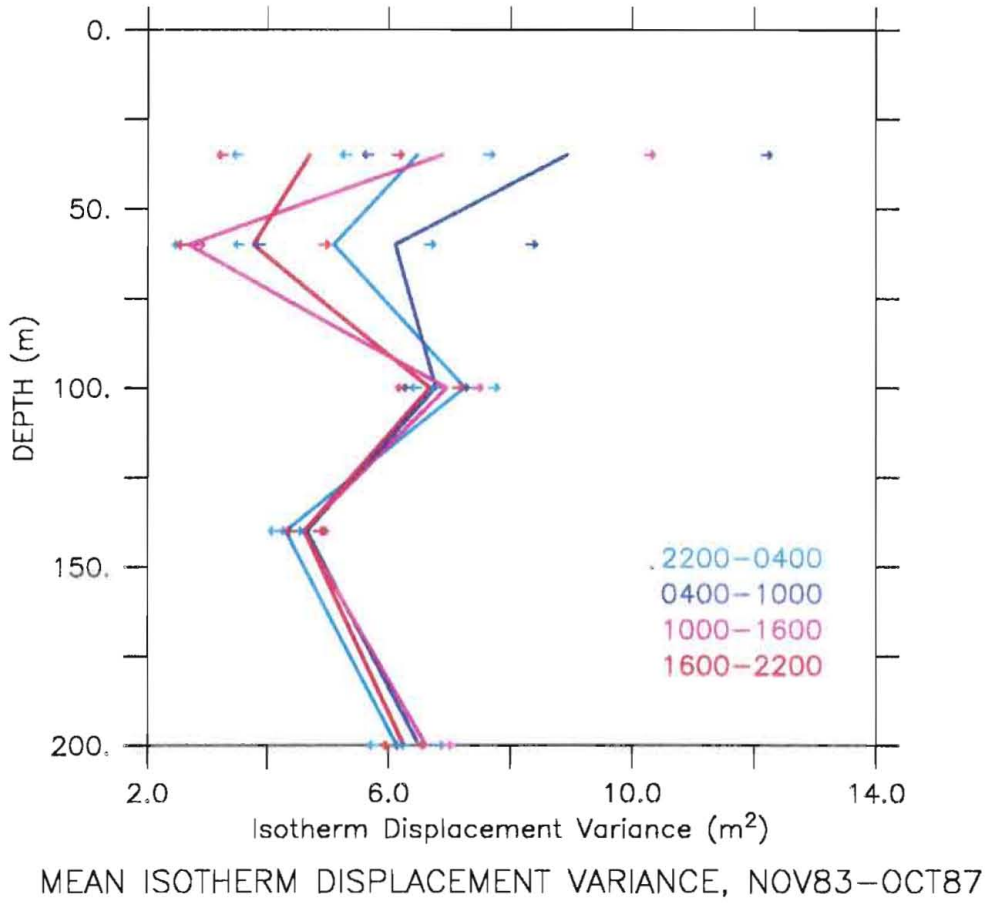

Figure 5.2. Mean vertical profiles of isotherm displacement variance (IDV) for four six-hour time bins over the depth range 35-200 m. Mean profiles computed from monthly means of IDV during November 1983 - October 1987. Small arrows indicate ±one standard error of the mean.

C. SEASONAL CYCLE OF IDV

The seasonal cycles of IDV at 35 m, 60 m, 100 m, 140 m, and 200 m for each of the four six-hour time bins are presented in Figures 5.3a-e. These seasonal cycles were computed from the monthly mean values of IDV presented in Figures 5.1a-e. The seasonal cycle of IDV at 35 m shows a pronounced annual cycle with nighttime maxima of about 10 m^2 occurring during the boreal winter months November through January and nighttime minima of about 2 m^2 occurring during the boreal spring months March and April (Figure 5.3a). A pronounced seasonal cycle of the diurnal cycle of IDV, ΔIDV, at 35 m was well correlated with the seasonal cycle of IDV. Maxima of ΔIDV at 35 m of about 6 m^2 occurred during the months November through January and minima near zero occurred during the months March and April.

The seasonal cycle of IDV at 60 m had a pronounced annual cycle of the nighttime IDV with maxima of about 5.2 m^2 occurring during the boreal winter months November through January and minima of less than 2.0 m^2 during May and June (Figure 5.3b). The pattern was similar to that described for IDV at 35 m except the magnitudes were reduced and there appears to have been a higher frequency seasonal oscillation with a period of 3-4 months. The seasonal cycle of ΔIDV at 60 m was also similar to that at 35 m with maxima of about 2.5 m^2 occurring from November through January and minima near zero in May and June.

The seasonal cycle of IDV at 100 m underwent apparent annual and bi-monthly variations (Figure 5.3c). Annual maxima exceeding 10 m^2 occurred in October and January and an annual minimum of about 4.5 m^2 occurred in August. There does not appear to have been a significant seasonal cycle of ΔIDV at 100 m. There was, however, a significant seasonal peak in ΔIDV during the month of October. The seasonal cycles of IDV and ΔIDV at 140 m and 200 m were not significant (Figures 5.3d,e).

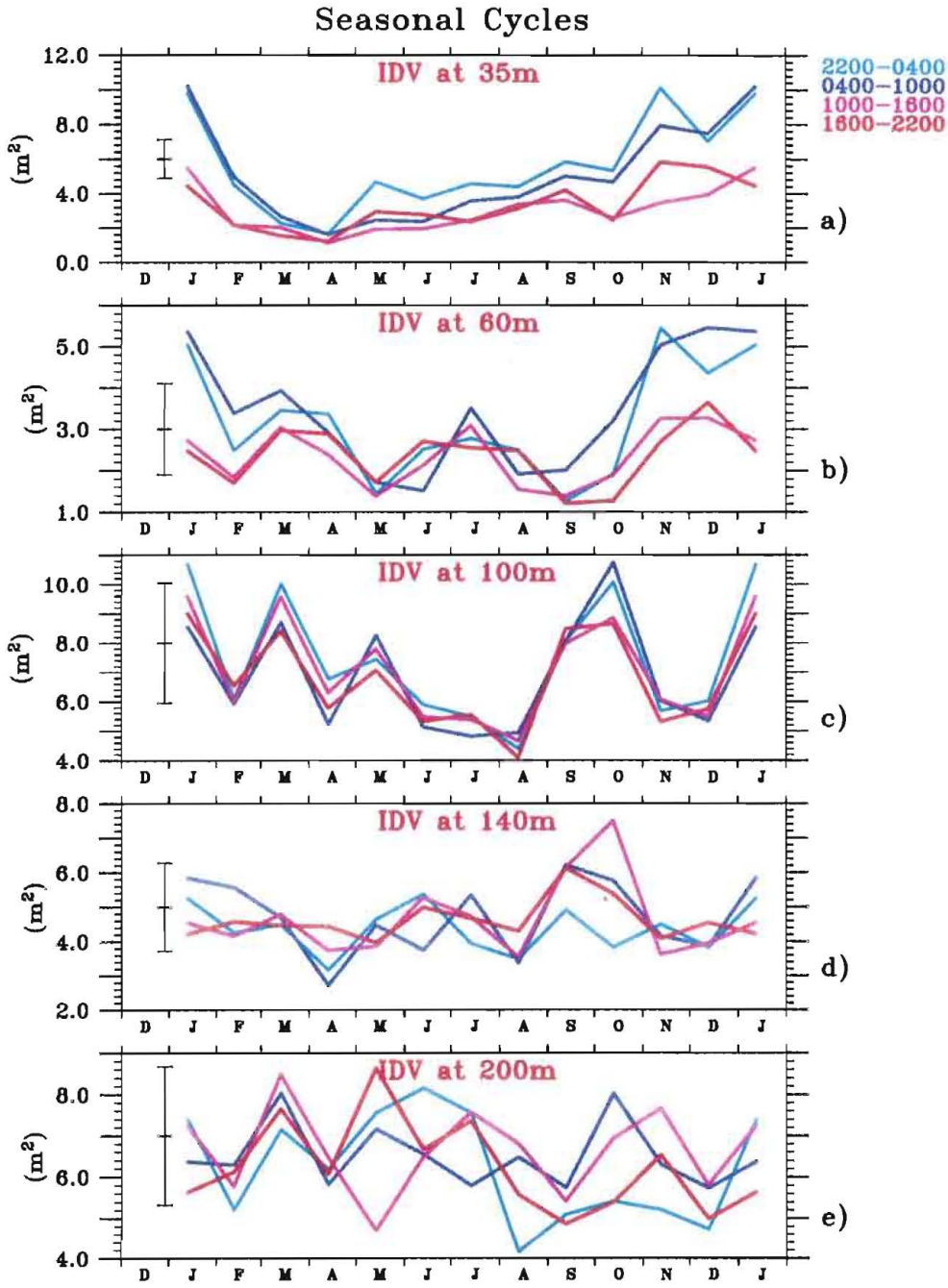

Figure 5.3a-e. Seasonal cycles of isotherm displacement variance (IDV) for the four six-hour time bins at five depths: a) 35 m, b) 60 m, c) 100 m, d) 140 m, and e) 200 m. Seasonal cycles are computed from monthly mean values of IDV during the period November 1983-October 1987. Error bars indicate the mean standard error of the mean for all time bins over the twelve calendar months. Units are m^2.

D. RELATIONSHIPS BETWEEN IDV AND SURFACE FORCING

In this section, statistical relationships between monthly means of surface forcing conditions and monthly means of IDV at 35 m, 60 m, 100 m, 140 m, 200 m, and 300 m are examined. Table 5.1 shows correlation coefficients computed between IDV at these six depths and surface winds. Wind speed and zonal wind were significantly correlated, at the 95% confidence level, with IDV at 35 m during the evening and night time bins and with IDV at 60 m during the night and morning time bins. These time differences of the significant correlations suggest a possible phase lag with depth of about 6 hours that is consistent with phase lags of turbulent dissipation observed during TROPIC HEAT (Peters et al., 1988; Moum et al., 1989) and modelled numerically (Garwood et al., 1989; Schudlich and Price, 1992; Skyllingstad and Denbo, 1994). The lower correlations occurred after sunrise, when the surface layer underwent restratification. The significant correlations at 35 m and 60 m were positive for wind speed and negative for the easterly (negative) zonal wind. In each case, IDV increased with increased mechanical energy input by the wind. Surface winds were not generally well correlated with IDV at 100 m, 140 m, 200 m, and 300 m, with two exceptions. Significant correlations were observed between both wind speed and zonal wind and IDV at 200 m during the evening time bin and with IDV at 300 m during the morning time bin. The lack of significant correlation between surface winds and IDV at intermediate depths argues against local wind forcing and vertical wave propagation to explain the deeper correlations. More likely, they are related to larger-scale processes. Meridional winds and wind direction were not well correlated with IDV at any of the six depths examined for any of the four six-hour time bins.

Statistical relationships were examined between IDV at the six TR depths for each of the four six-hour time bins and each of the terms of the surface heat and buoyancy balances. Correlations were computed for the following terms: net surface heat flux (Q_{net}), shortwave radiation (Q_s), latent heat flux (Q_e), sensible heat flux (Q_h), longwave radiation (Q_b), net surface buoyancy flux (B_{net}), moisture flux ($B_{moisture}$), precipitation (P), and evaporation minus precipitation (E-P). Generally, the surface fluxes were not well correlated with IDV at most depths. The following terms were found to be not

Table 5.1. Correlations coefficients, r, between monthly mean isotherm displacement variances (IDV) at six depths for four 6-hour time bins and surface winds (WSPD: wind speed; U: zonal wind; V: meridional wind; WDIR: wind direction) during November 1983 - October 1987. Statistical significance at the 95% confidence level was calculated using computed integral time scales between time series (Davis, 1976). Statistically significant correlations are indicated by **Bold** type.

VARIABLES	2200-0400		0400-1000		1000-1600		1600-2200	
	95%c.i.	r	95%c.i.	r	95%c.i.	r	95%c.i.	r
WSPD/IDV 35	**.418**	**.477**	.339	.241	.309	.261	**.372**	**.409**
/IDV 60	**.311**	**.335**	**.339**	**.346**	.240	.176	.263	.145
/IDV100	.310	.009	.287	-.163	.300	-.063	.309	-.108
/IDV140	.311	.011	.418	.244	.360	.113	.388	.043
/IDV200	.399	.263	.271	-.233	.280	-.087	**.347**	**-.391**
/IDV300	.282	-.270	**.246**	**.267**	.260	.070	.283	.042
U /IDV 35	**.430**	**-.492**	.341	-.256	.308	-.263	**.379**	**-.403**
/IDV 60	**.315**	**-.346**	**.341**	**-.359**	.246	-.178	.263	-.144
/IDV100	.311	.011	.287	.189	.299	.094	.311	.136
/IDV140	.306	.015	.423	-.279	.361	-.121	.387	-.080
/IDV200	.401	-.294	.270	.226	.280	.074	**.352**	**.389**
/IDV300	.281	.263	**.236**	**-.253**	.250	-.077	.278	-.051
V /IDV 35	.486	.202	.252	.145	.258	.121	.432	.304
/IDV 60	.266	.004	.308	.073	.264	.096	.278	.114
/IDV100	.302	.155	.307	.152	.311	.181	.300	.204
/IDV140	.312	.153	.341	-.176	.247	.019	.307	-.263
/IDV200	.359	-.193	.239	-.064	.293	.022	.391	-.183
/IDV300	.344	-.185	.281	.162	.307	-.086	.302	-.042
WDIR/IDV 35	.486	.183	.260	.174	.253	.079	.425	.206
/IDV 60	.267	-.027	.300	.032	.272	.076	.278	.030
/IDV100	.302	.081	.291	.100	.295	.074	.310	.128
/IDV140	.306	.076	.341	-.144	.266	.118	.294	-.180
/IDV200	.339	-.246	.229	.005	.293	.152	.393	-.203
/IDV300	.337	-.219	.264	.093	.267	-.158	.293	.038

significantly correlated with IDV at any of the six TR depths for any of the time bins and will not be specifically discussed: Q_b, $B_{moisture}$, P, and E-P. Correlations between monthly mean IDV and remaining terms of the surface heat balance are given in Table 5.2, and the correlations between IDV and the remaining terms of the surface buoyancy balance are given in Table 5.3.

As shown in Table 5.2, correlations with the terms of the surface heat flux were generally small. The only term having statistically significant correlation at the 95% confidence level with IDV in the upper 100 m was Q_e, which had a correlation of -0.422 with IDV at 35 m during the evening time bin. The negative sign of this correlation indicates that IDV was high when heat loss from the ocean by Q_e increased. The latent heat flux was also significantly correlated with IDV at 200 m (r = 0.310). Correlations between IDV at 140 m and Q_h and Q_{net} were significant during the morning and day time bins and day and evening time bins, respectively. It does not seem likely that the small changes in Q_h could be strong enough to locally force temperature variability at 140 m, particularly since Q_h was not well correlated with IDV in the upper 100 m. Although Q_{net} could possibly generate vertically-propagating waves, the lack of correlation in the upper 100 m suggests non-local forcing.

The correlations between IDV at the six TR depths for the four six-hour time bins and B_{net} and E were also generally weak (Table 5.3). Both B_{net} and E were significantly correlated with IDV at 35 m during the evening time bin. The correlation with B_{net} was -0.374, indicating that IDV was higher when buoyancy decreased. Similarly, the correlation with E of 0.421 indicates that IDV was higher when evaporation increased.

Table 5.2. Correlation coefficients, r, between monthly mean isotherm displacement variances (IDV) at six depths for four time bins and surface heat flux terms: net surface heat flux, Q_{net}, shortwave radiation, Q_s, latent heat flux, Q_e, and sensible heat flux, Q_h. Statistical significance at the 95% confidence level was calculated based on the integral time scale between time series (Davis, 1976). Statistically significant correlations are indicated by **Bold** type.

VARIABLES	2200-0400 95%c.i.	r	0400-1000 95%c.i.	r	1000-1600 95%c.i.	r	1600-2200 95%c.i.	r
Q_{net}/IDV 35m	.372	-.195	.368	-.070	.316	-.108	.357	-.339
/IDV 60m	.300	-.003	.309	.030	.307	.004	.289	-.024
/IDV100m	.317	.027	.308	.120	.300	-.020	.303	.038
/IDV140m	.317	.027	.340	.292	**.311**	**.345**	**.306**	**.359**
/IDV200m	.321	.100	.273	.238	.279	.041	.300	-.045
/IDV300m	.255	-.038	.235	-.193	.230	-.080	.273	.121
Q_s /IDV 35m	.480	.255	.391	.058	.325	.017	.438	.173
/IDV 60m	.299	.116	.318	.174	.281	-.007	.278	-.001
/IDV100m	.327	.019	.311	.112	.315	.019	.326	.044
/IDV140m	.325	.021	.378	.330	.313	.169	.303	.242
/IDV200m	.334	.084	.228	-.051	.260	-.046	**.368**	**-.499**
/IDV300m	**.261**	**-.301**	.211	.059	.221	.013	.285	.237
Q_e/IDV 35m	.393	-.307	.337	-.056	.294	-.093	**.357**	**-.422**
/IDV 60m	.308	-.073	.337	-.071	.244	-.014	.269	-.043
/IDV100m	.326	.017	.280	.088	.284	-.037	.317	.016
/IDV140m	.317	.013	.406	.146	.370	.297	.382	.249
/IDV200m	.395	.086	**.286**	**.310**	.302	.107	.356	.270
/IDV300m	.288	.190	.250	-.245	.244	-.118	.282	-.028
Q_h/IDV 35m	.426	-.317	.328	-.186	.317	-.033	.391	-.105
/IDV 60m	.276	-.206	.304	-.224	.230	-.033	.271	.095
/IDV100m	.304	.149	.284	-.033	.288	.159	.311	.089
/IDV140m	.306	.157	**.372**	**-.432**	**.316**	**-.363**	.342	-.262
/IDV200m	.347	-.253	.263	-.196	.292	-.158	.367	.045
/IDV300m	.293	-.063	.248	-.133	.254	-.121	.290	-.273

Table 5.3. Correlation coefficients, r, between monthly mean isotherm displacement variances (IDV) at six depths for four time bins and the net surface buoyancy flux, B_{net}. Statistical significance at the 95% confidence level was calculated based on the integral time scale between the time series (Davis, 1976). Statistically significant correlations are indicated by **Bold** type.

VARIABLES	2200-0400		0400-1000		1000-1600		1600-2200	
	95%c.i.	r	95%c.i.	r	95%c.i.	r	95%c.i.	r
B_{net} /IDV35m	.280	-.123	.326	.080	.287	-.009	**.287**	**-.313**
/IDV 60m	.295	-.057	.309	-.131	.275	.108	.286	.163
/IDV100m	.329	.139	.326	.131	.321	.054	.301	.050
/IDV140m	.329	.146	.303	.079	.317	.149	.320	.220
/IDV200m	.303	-.121	.302	.086	.285	.218	.266	.023
/IDV300m	.272	-.001	.276	-.191	.291	-.191	.283	.107

E. RELATIONSHIP BETWEEN IDV AND DYNAMIC STABILITY

In this section, statistical relationships between monthly means of the dynamic stability parameters, N, S, and Ri, and IDV at 35 m, 60 m, and 100 m are discussed. Correlation coefficients for each of the above parameters and IDV at these three depths for the four six-hour time bins are presented in Table 5.4. Generally, correlations between IDV and these stability parameters were weak. Monthly mean IDV was significantly correlated at the 95% confidence level with N at 35 m during the day, evening and night time bins. These correlations were negative indicating that IDV at 35 m increased with decreasing stratification. This result is consistent with linear theory in that increased isotherm displacements are expected with reduced stratification. Correlations between IDV and N at 60 m and 100 m were not significant at the 95% confidence level. Correlations between both IDV and S and IDV and Ri were not statistically significant at 35 m, 60 m, or 100 m.

Table 5.4. Correlation coefficients, r, between monthly mean isotherm displacement variances (IDV) and buoyancy frequency (N), velocity shear (S), and Richardson number (Ri) at 35 m, 60 m, and 100 m for four six-hour time bins during November 1983 - October 1987. Statistical significance at the 95% confidence level was calculated based on the integral time scale between the time series (Davis, 1976). Statistically significant correlations are indicated by **Bold** type.

Variables	2200-0400 95%c.i.	r	0400-1000 95%c.i.	r	1000-1600 95%c.i.	r	1600-2200 95%c.i.	r
IDV/*N*_35m	**.382**	**-.444**	.358	-.356	**.321**	**-.351**	**.339**	**-.394**
60m	.323	-.194	.356	-.323	.219	-.048	.252	-.162
100m	.291	-.161	.262	-.031	.281	-.032	.306	-.046
IDV/*S*_35m	.326	-.076	.380	-.159	.326	-.155	.326	-.147
60m	.287	-.044	.287	.028	.287	-.086	.287	-.223
100m	.287	-.084	.287	.004	.287	-.137	.287	-.102
IDV/*Ri*_35m	.326	-.088	.326	-.018	.326	.000	.326	.022
60m	.323	-.075	.323	-.215	.323	.074	.323	.141
100m	.290	-.032	.290	-.107	.290	.003	.290	.015

Correlations between IDV and the dynamic stability parameters at 140 m, 200 m, and 300 m were weak and could not be simply related to the diurnal cycle of turbulence or high-frequency internal waves under investigation here.

F. RELATIONSHIP BETWEEN IDV AND MIXED-LAYER DEPTH

Mixed-layer depth and the diurnal range of mixed-layer depth provide an indication of the cumulative effects of both surface forcing and the static and dynamic stability of the upper ocean. As such, it represents an integral of the processes thought to be associated with upper ocean mixing and the generation of high-frequency temperature variability in the mixed layer and in the thermocline below the mixed layer. Correlation coefficients between monthly mean mixed-layer depths and the diurnal range of mixed-layer depth and IDV at 35 m, 60 m, 100 m, 140 m, 200 m, and 300 m for the four time bins are shown in Table 5.5.

The correlations between mixed-layer depth and IDV at 35 m were significant at the 95% confidence level during the evening, night, and morning time bins. These correlations were particularly strong, -0.583 and -0.627, during the evening and night time bins, respectively. The negative sign of the correlations indicates that IDV at 35 m increased as the mixed layer deepened, in agreement with the microstructure observations of mixing and internal waves in the upper ocean discussed in Chapter 2. Mixed-layer depth and IDV at 35 m were not well correlated during the day time bin, when the mixed layer was shallow due to daytime restratification. With the mixed layer being shallow during this day time bin, it is not unreasonable to expect a decoupling with IDV at 35 m. The strong correlation between IDV at 35 m and mixed-layer depth during the evening time bin might have been less expected since the mixed layer was typically shallow (Figures 4.9 and 4.11). Close examination of these figures shows that, except for during the boreal spring, the mixed layer was deeper during the evening time bin than during the day time bin, indicating that the active nighttime convection had begun. Significant negative correlations were likewise observed between mixed-layer depth and IDV at 60 m during the morning, day, and evening time bins (Table 5.5). The correlation between mixed-layer depth and IDV at 60 m during the night time bin was just below the 95%

confidence level. The correlations were largest during the morning and evening time bins, -0.497 and -0.471, respectively. These stronger correlations during the morning and evening time bins might signify that during those hours active changes were occurring in both mixed-layer depth and IDV at 60 m. IDV at 100 m and 140 m was not significantly correlated with the mixed-layer depth on monthly time scales. Positive correlation between IDV at 200 m and mixed-layer depth was observed during the evening and morning time bins. Also, positive correlation was observed between mixed-layer depth and IDV at 300 m during the night time bin. Although it is difficult to determine with certainty whether or not these correlations with IDV at 200 m and 300 m reflect a direct physical relationship, the lack of significant correlation at 100 m and 140 m suggests non-local, large-scale forcing.

The diurnal range of mixed-layer depth can be thought of as a measure of the intensity of mixing on diurnal time scales. The diurnal range of mixed-layer depth was significantly correlated with IDV at 35 m during the night and morning time bins, when IDV was at its diurnal high (Figures 5.1-5.3). These correlations indicate that when the monthly mean diurnal range of mixed-layer depth was large, indicating high diurnally-modulated mixing intensity, the high-frequency temperature variability at 35 m was increased. During the daytime hours, when IDV at 35 m was at its diurnal low, the correlation with diurnal range of mixed-layer depth was weak. The correlations between IDV at 60 m and 100 m and diurnal range of mixed-layer depth were not significant. Significant correlations between the diurnal range of mixed-layer depth and IDV at 140 m during the morning and evening time bins and IDV at 200 m during the night and day time bins cannot be simply related to local forcing. As with the significant correlations between mixed-layer depth and IDV at 200 m and 300 m, these relationships between the diurnal range of mixed-layer depth and IDV at 140 m and 200 m are probably related to large-scale processes.

Table 5.5. Correlation coefficients, r, between monthly mean isotherm displacement variances (IDV) at six depths for each of the four 6-hour time bins and mixed-layer depth (MLD) and diurnal range of mixed-layer depth (ΔMLD) during the period November 1983 - October 1987. Statistical significance at the 95% confidence level was calculated based on the integral time scale between the time series (Davis, 1976). Statistically significant correlations are indicated by **Bold** type.

VARIABLE	2200-0400		0400-1000		1000-1600		1600-2200	
	95%c.i.	r	95%c.i.	r	95%c.i.	r	95%c.i.	r
MLD/IDV35m	**.467**	**-.627**	**.327**	**-.438**	.314	-.227	**.433**	**-.583**
/IDV 60m	.293	-.292	**.329**	**-.471**	**.277**	**-.330**	**.287**	**-.497**
/IDV100m	.297	-.168	.304	.026	.298	-.100	.279	-.074
/IDV140m	.297	-.173	.378	-.046	.268	.090	.331	.232
/IDV200m	.381	-.043	**.256**	**.314**	.255	.130	**.343**	**.354**
/IDV300m	.282	.173	.210	-.011	.254	.037	.278	.180
ΔMLD/IDV35	**.392**	**.421**	**.329**	**.490**	.297	.233	.341	.231
/IDV 60m	.332	.146	.328	.195	.286	.170	.281	.250
/IDV100m	.322	.004	.298	.071	.298	.054	.334	.030
/IDV140m	.330	.010	**.387**	**.447**	.359	.190	**.354**	**.410**
/IDV200m	**.357**	**.470**	.288	-.045	**.273**	**-.298**	.350	-.210
/IDV300m	.316	-.066	.310	-.050	.325	.035	.318	.198

VI. DIURNAL CYCLE OF ISOTHERM DISPLACEMENT VARIANCE

In the preceding two chapters, the interannual and seasonal variability of the surface forcing, background dynamic stability, mixed-layer depth, and high-frequency IDV have been described, and statistical relationships among these fields were examined. In this chapter, the focus shifts to the diurnal cycle of the high-frequency variations of temperature, as measured by ΔIDV.

A. VERTICAL EXTENT OF DIURNAL CYCLE OF IDV

The time series of monthly mean IDV at five depths for the four six-hour time bins presented in Figure 5.1a-e showed pronounced increases of IDV during the night and morning time bins, collectively referred to as nighttime, at both 35 m and 60 m for much of the 48 month record. At 35 m, the nighttime monthly-mean IDV increase frequently exceeded 5 m^2 compared with daytime values. During a few months this nighttime increase of IDV exceeded 10 m^2. At 60 m, the nighttime monthly mean IDV values frequently exceeded daytime IDV values by about 5 m^2. At 100 m and below, these diurnal differences in monthly mean IDV were rarely observed. Similarly, examination of individual monthly mean vertical profiles of IDV (not shown) and the long-term mean vertical profile of IDV (Figure 5.2) showed that the diurnal cycle of monthly mean IDV only rarely penetrated to 100 m. Figure 5.2 also indicated high variability of monthly mean IDV at 35 m and 60 m and relatively low variability of monthly mean IDV at 100 m, 140 m, and 200 m.

Further examination of the vertical extent of the diurnal cycle of IDV was accomplished by computing monthly means of the daily differences between IDV during different six-hour time bins. Since diurnal differences of IDV appeared dependent on the magnitude of IDV, i.e. larger differences were observed when IDV was high (Figure

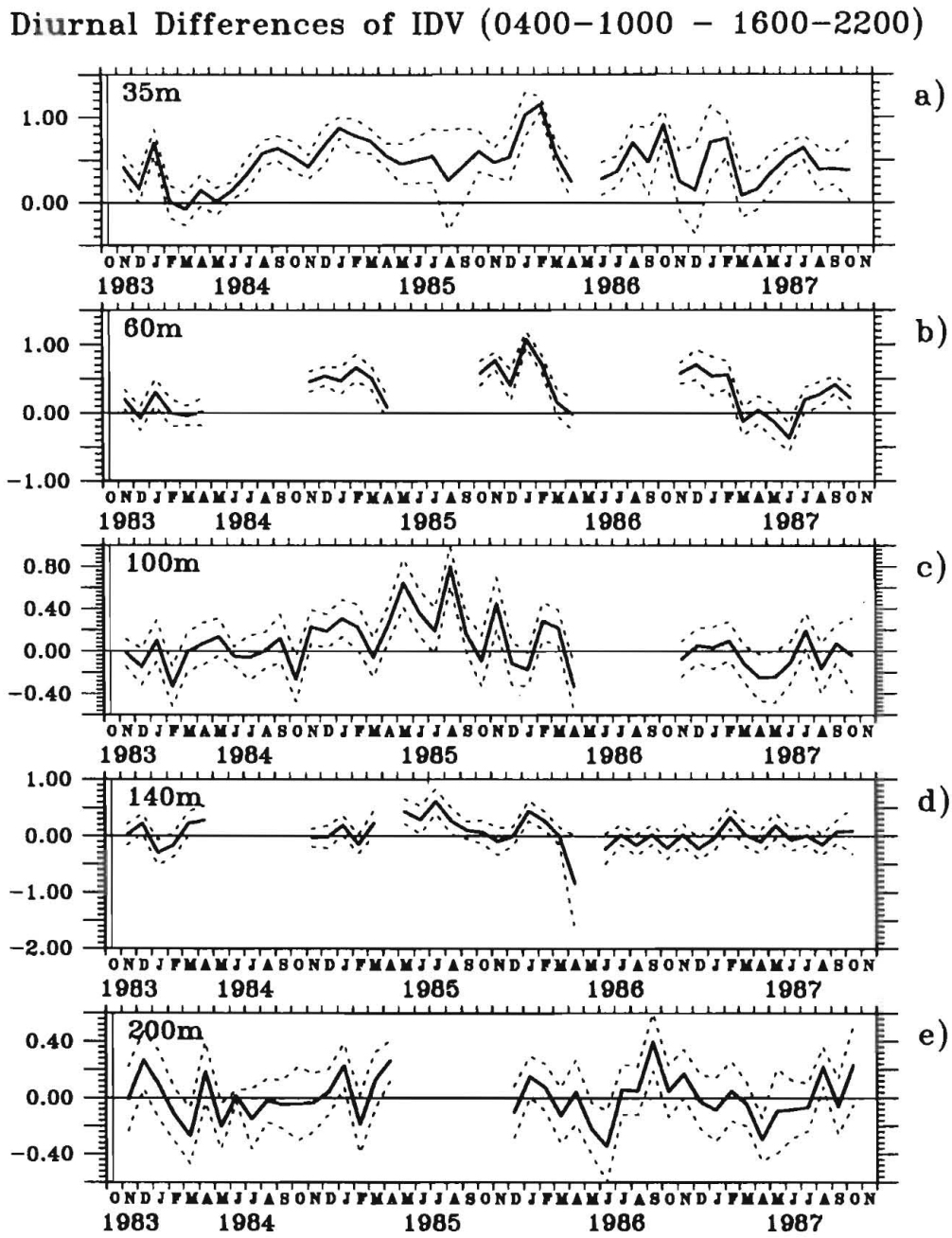

Figure 6.1. Monthly mean normalized diurnal differences of isotherm displacement variance (ΔIDV_{mc}) computed from daily values of 0400-1000 IDV minus 1600-2200 IDV at a) 35 m, b) 60 m, c) 100 m, d) 140 m, and e) 200 m. Daily diurnal differences were normalized by the mean of the morning and evening IDV values for each day. Dashed lines indicate ±one standard error of the mean.

5.1), the diurnal differences have been normalized by the mean of the daily IDV values for the two time bins. Normalization provides a relative measure of the diurnal differences of IDV, allowing more direct examination over seasonal and interannual time scales. The monthly mean normalized diurnal differences between IDV during the morning time bin and IDV during the evening time bin, ΔIDV_{me} at 35 m, 60 m, 100 m, 140 m, and 200 m are shown in Figures 6.1a-e. The morning time bin corresponds with the times when the mixed layer was deepest (Figures 4.9 and 4.11). Both microstructure measurements and numerical model results have shown the diurnal peak in turbulent dissipation in the thermocline (Moum et al., 1989; Garwood et al., 1989; Schudlich and Price, 1992). The evening time bin corresponds to the time when the mixed layer was still shallow, and microstructure measurements have shown weak turbulent dissipation in the thermocline. For comparison, the monthly mean diurnal differences between IDV during the night time bin and IDV during the day time bin, ΔIDV_{nd} are shown in Figures 6.2a-e. Examination of the IDV time series suggests that differences between ΔIDV_{me} and ΔIDV_{nd} are generally small.

The monthly means of ΔIDV_{me} at 35 m show that the morning IDV is almost always greater than the evening IDV, and that for 81% of the record this difference is significant within a standard error of the mean (Figure 6.2a). The ΔIDV_{me} at 60 m shows that for 65% of the record length the morning IDV is greater than the evening IDV by at least one standard error of the mean (Figure 6.2b). By the 100 m depth, ΔIDV_{me} is greater than one standard error of the mean only 29% of the record, a considerable decrease from that at 60 m (Figure 6.2c). At 140 m and 200 m, these percentages were reduced to 17% and 12%, respectively (Figures 6.2d,e).

Examination of ΔIDV_{nd} shows similar, though weaker, diurnal differences of IDV (Figure 6.2a). ΔIDV_{nd} at 35 m shows that the night IDV values were greater than the day IDV values by at least one standard error for 72% of the record (Figure 6.2a). At 60 m, this percentage was reduced to 48%. At 100 m, 140 m, and 200 m, these percentages were 29%, 8 %, and 12 %, respectively. Even though each of these percentages were smaller than those computed for ΔIDV_{nd}, the same general pattern of decreased diurnal differences of IDV with depth was observed.

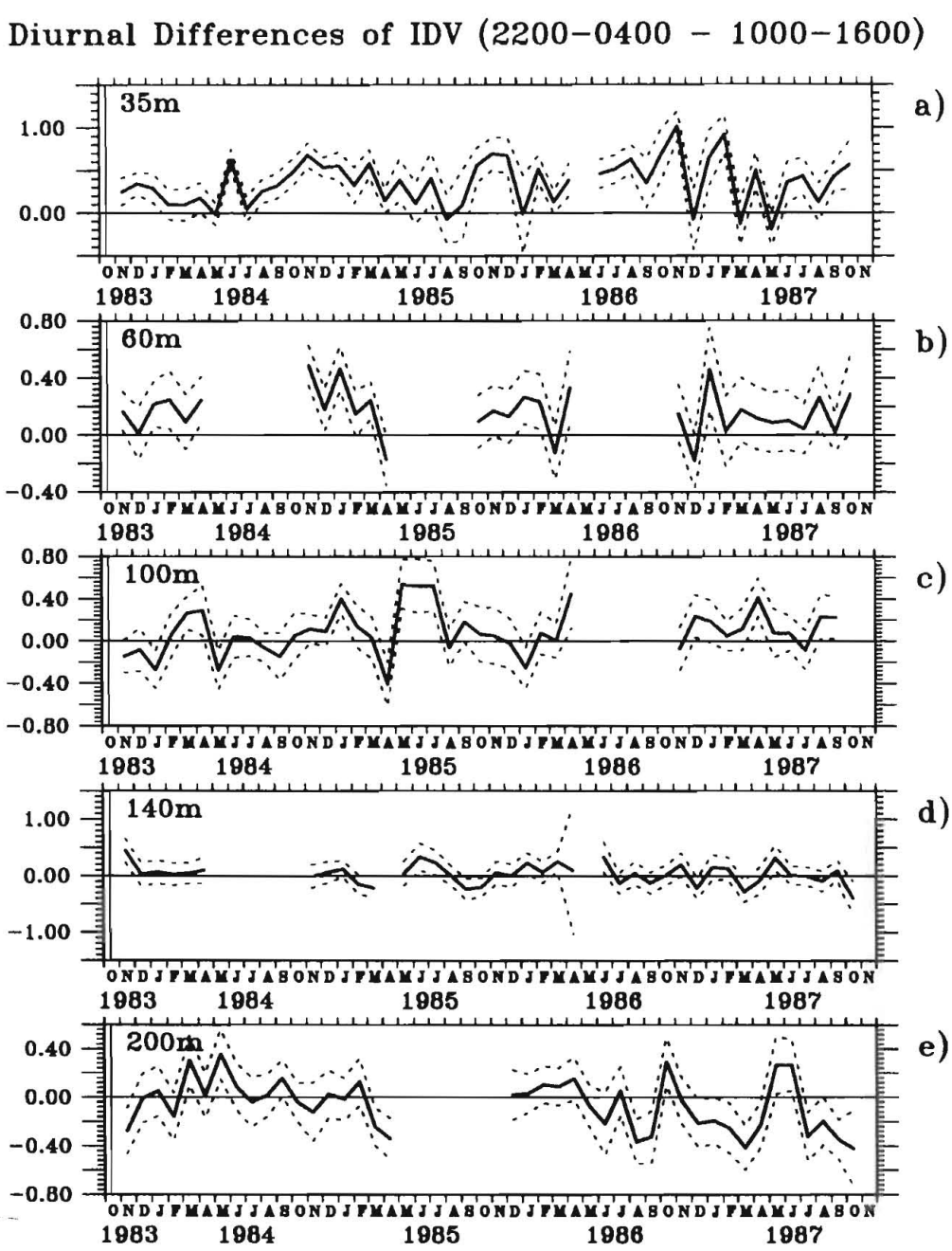

Figure 6.2. Monthly mean diurnal differences of isotherm displacement variance (ΔIDV_{nd}) computed from daily values of 2200-0400 IDV minus 1000-1600 IDV normalized by the mean of the two IDV values at a) 35 m, b) 60 m, c) 100 m, d) 140 m, and e) 200 m. Dashed lines indicate ±one standard error of the mean.

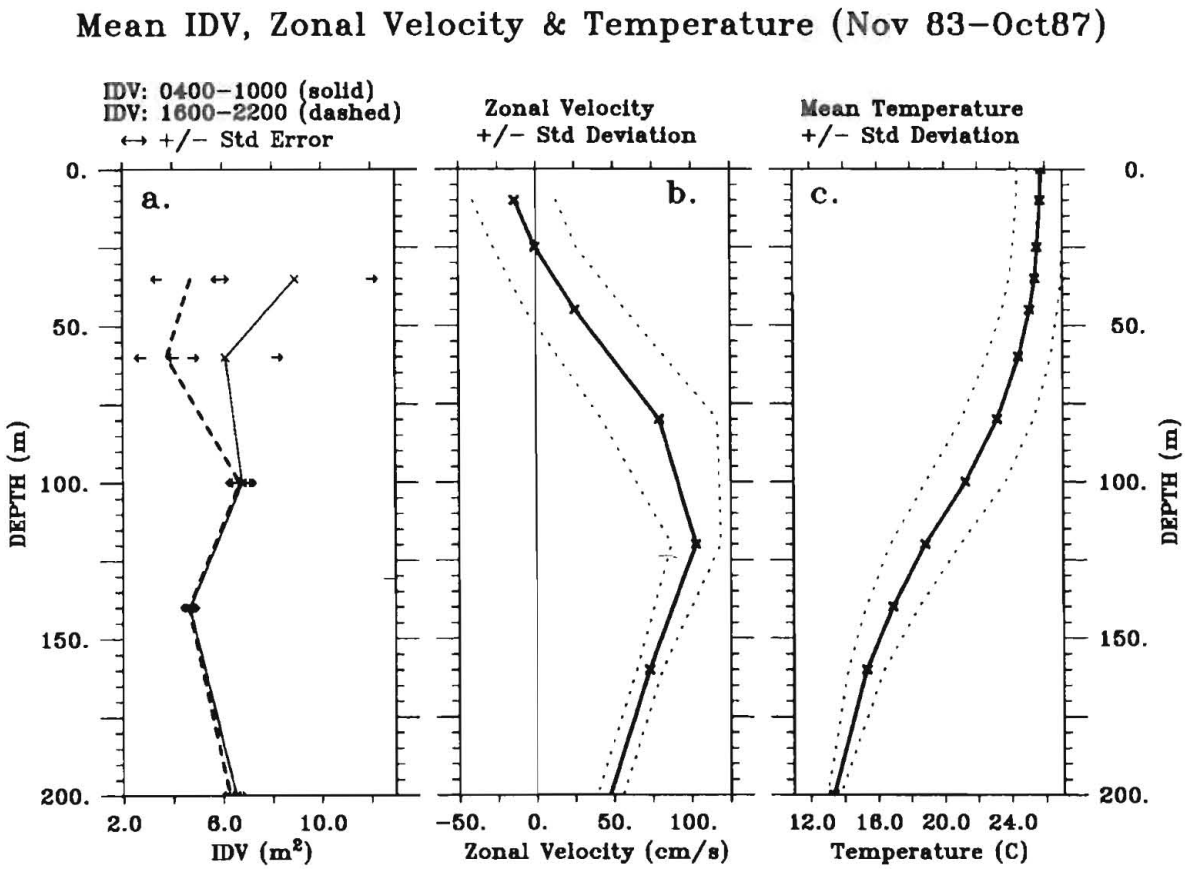

Figure 6.3. Long-term mean vertical profiles of a) Isotherm displacement variance for the 0400-1000 (solid line) and 1600-2200 (dashed line) time bins, b) zonal velocity, and c) temperature computed from all available monthly means during the period November 1983 - October 1987. Standard error of the mean is indicated by arrows in a), and standard deviations are indicated by dashed lines in b) and c).

To further evaluate the vertical structure of the diurnal cycle of high-frequency IDV and possible long-term consequences to the equatorial momentum balance, statistics of the vertical profile of IDV were computed from the 48 monthly mean values for each of the four six-hour time bins (Figure 5.2). These long-term mean IDV profiles were consistent with the above results that showed a pronounced diurnal difference of IDV at 35 m and 60 m, particularly between the morning and evening time bins. The long-term mean IDV profiles for these two time bins and the long-term mean vertical profiles of temperature and zonal velocity are shown in Figures 6.3a-c. Figure 6.3a shows pronounced diurnal differences in IDV at 35 m and 60 m, with the mean morning IDV greater than the mean evening IDV by about 4 m^2 and 2 m^2, respectively. This figure also shows a sharp decay with depth of the long-term mean diurnal cycle of high-frequency IDV. Although the time series of monthly mean diurnal differences showed occasional penetration of ΔIDV_{me} to 100 m and deeper (Figure 6.1), the long-term mean clearly shows that on average the diurnal cycle was not evident at 100 m, 140 m, or 200 m. Figure 6.3 also shows the depths of the observed ΔIDV_{me} relative to the mean EUC and thermocline. In the long-term mean, the ΔIDV_{me} did not penetrate through the EUC core or high-N region of the thermocline. As was shown in the time series (Figure 6.2), the long-term mean diurnal difference of IDV between night and day time bins is apparent, but weaker than the morning/evening difference.

Another method of examining the vertical structure of the high-frequency ΔIDV is to compute vertical correlations between the ΔIDV at different depths. The advantage of this method is that it provides an indication of the relationship between the diurnal cycle of the high-frequency variability at different depths. Strong correlations over a large vertical extent would be consistent with hypotheses suggesting vertical internal wave propagation. Correlation coefficients between the monthly mean ΔIDV_{me} at 35 m and ΔIDV_{me} at 60 m, 100 m, 140 m, 200 m, and 300 m are shown in Figure 6.4. Based on the result that the most pronounced diurnal difference in IDV occurred between the morning and evening time bins, this is the diurnal difference used in the computation of the correlation coefficients shown in Figure 6.4. Mean profiles of zonal velocity and temperature illustrate the positions of the EUC and thermocline relative to the vertical

structure of ΔIDV.

The correlation between the monthly mean ΔIDV_{me} at 35 m and ΔIDV_{me} at 60 m was strong, +0.61, indicating that when the ΔIDV_{me} at 35 m increased there was likely to be a corresponding increase of ΔIDV_{me} at 60 m, and vice versa. The correlations between ΔIDV_{me} at 35 m and ΔIDV_{me} at 100 m, 140 m, 200 m, and 300 m were not significant at the 95% confidence level.

On shorter times scales, the 15-minute temperature measurements were used to examine vertical propagation by computing correlations as a function of time lag (every 15 minutes) and depth. In addition to sharp decay with depth, in agreement with monthly mean results, those correlations indicated highest vertical correlations at zero lag, suggesting little downward phase propagation.

These combined results indicate that vertical propagation of high-frequency internal waves from the surface layer, if occurring, did not appear to propagate through the EUC core using monthly-averaged statistics. These results do not rule out the possibility that a diurnal cycle of IDV may be occasionally observed at depths greater than 60 m. For example, ΔIDV_{me} at 100 m was greater than one standard error of the mean for 29% of the months examined (Figure 6.1). However, on average the results indicate that the diurnal cycle of IDV decayed sharply below 60 m.

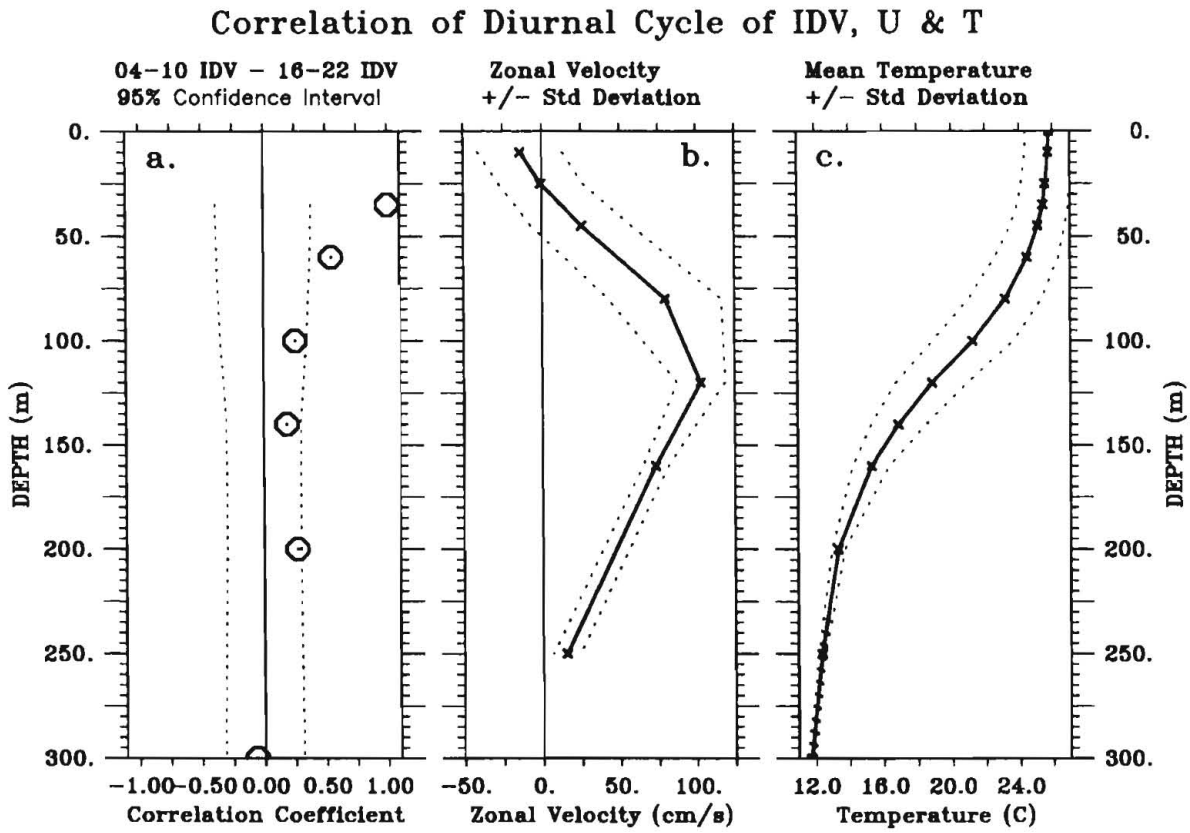

Figure 6.4. Vertical profiles of a) correlation coefficients between monthly mean diurnal differences of isotherm displacement variance (ΔIDV_{mc}) at 35 m and those at 60 m, 100 m, 140 m, 200 m, and 300 m, b) long-term mean zonal velocity, and c) long-term mean temperature. Dashed lines indicate a) 95% confidence intervals based on integral time scales between time series (Davis, 1976), and b) and c) standard deviations.

B. INTERANNUAL VARIABILITY OF THE DIURNAL CYCLE OF IDV

In discussing the interannual variability of IDV for the four six-hour time bins shown in Figures 5.1a-e, mention was made of the interannual variability of the diurnal cycle of IDV at 35 m and 60 m. Further examination of Figures 5.1a,b shows that during the 1984 ENSO cold episode, a diurnal cycle of IDV was not observed at either 35 m or 60 m. This disappearance of the diurnal cycle during the cold episode was also apparent in the time series of monthly means of ΔIDV_{me} (Figures 6.1a,b). Beginning in mid-1984, ΔIDV at 35 m reappeared and remained present during most of the next two years (Figure 6.1a). Comparison with the subsurface temperature record (Figure 4.7) shows that the reappearance coincided with the beginning of a two-year deepening of the thermocline. Although the daytime IDV values increased during this ENSO build-up phase, it appears that ΔIDV_{me} was dominated by larger increases of IDV during the nighttime hours (Figure 5.1a). During the 1986/1987 ENSO warm episode, this did not appear to be the case. Both daytime and nighttime IDV values increased above the annual boreal winter maximum (Figure 5.1a) and ΔIDV_{me} decreased (Figure 6.1a). Although the long-term mean vertical profiles of IDV did not show a diurnal cycle at 100 m (Figures 5.2 and 6.3), diurnal differences of IDV at 100 m were not uncommon during the ENSO build-up phase between November 1984 and March 1986 (Figure 6.1c).

C. SEASONAL CYCLE OF DIURNAL CYCLE OF IDV

As discussed in section 5.3, there was a pronounced seasonal cycle of IDV at 35 m and 60 m and a weaker seasonal cycle of IDV at 100 m. Examination of Figure 5.2 shows a similar seasonal cycle of the diurnal IDV signal, as indicated by the relative divergence of the nighttime and daytime IDV curves at 35 m and 60 m. As with IDV, ΔIDV was observed to be strongest during the boreal winter months and weakest during the boreal spring. Seasonal cycles of ΔIDV from the monthly mean values of ΔIDV_{me} (Figure 6.1) are shown in Figure 6.5. Figures 6.5a,b indicate a pronounced annual cycle of ΔIDV at 35 m and 60 m, with maxima occurring during the boreal winter and minima occurring during the boreal spring. Indications of an apparent semi-annual cycle of ΔIDV at 35 m were also observed. An apparent weak annual cycle of ΔIDV at 100 m was observed

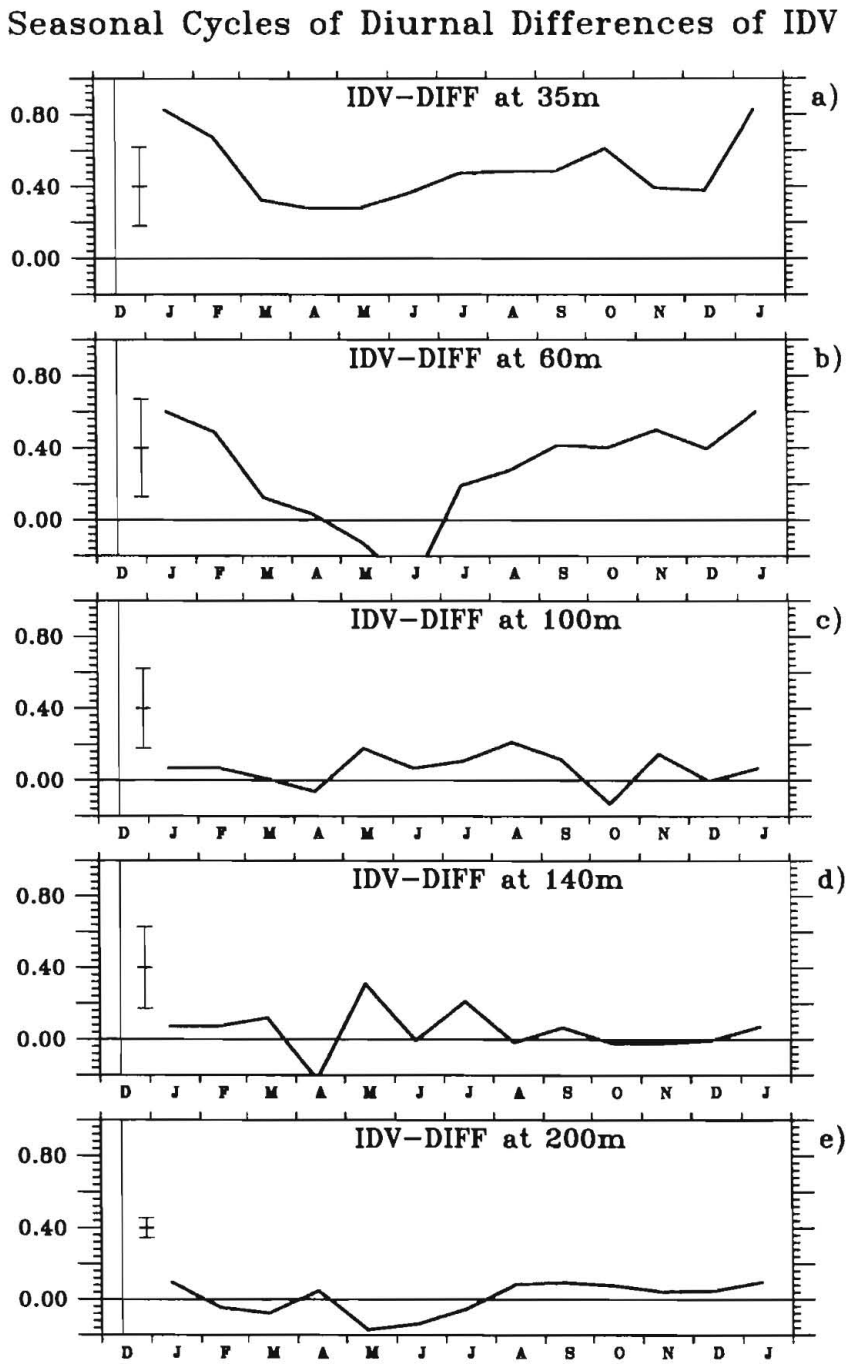

Figure 6.5. Seasonal cycles of the diurnal difference of IDV at a) 35 m, b) 60 m, c) 100 m, d) 140 m, and e) 200 m. Computed from normalized monthly mean differences of IDV between 0400-1000 and 1600-2000. Error bars represent average of all of the individual standard errors for each of the twelve calendar months.

with relative maxima occurring during the boreal summer months and near zero diurnal differences occurring during the boreal winter months. This weak annual cycle at 100 m, opposite in phase to the annual cycles of ΔIDV at 35 m and 60 m, was not significant based on ±one standard error of the mean. The seasonal variability of ΔIDV was not significant at both 140 m and 200 m since diurnal variations of IDV were usually not evident.

D. SURFACE FORCING AND THE DIURNAL CYCLE OF IDV

In this section, statistical relationships between the diurnal cycle of IDV and several indices of surface forcing are presented. Based on the earlier finding that the strongest diurnal difference of IDV occurred between the morning and evening time bins, monthly means of ΔIDV_{me} at 35 m, 60 m, and 100 m were used as the reference of the diurnal cycle of IDV to examine these relationships (Figure 6.1). With the prior finding that there was no apparent diurnal cycle of IDV at 140 m, 200 m, and 300 m, the statistical relationships between ΔIDV_{me} at these depths and the surface forcing indices are not of interest. The monthly mean time series of each of the surface forcing conditions described in section 4.2.1 were correlated with ΔIDV_{me}.

1. Surface Winds

In section 5.4, surface wind speed and zonal wind speed were shown to be strongly correlated with IDV at 35 m and 60 m on monthly time scales. In this section, correlations between monthly mean wind speed and direction, and the zonal and meridional wind components, and monthly mean ΔIDV_{me} at 35 m, 60 m, and 100 m are examined. Table 6.1 shows these correlations and their significance at the 95% confidence level based on the integral time scale between time series (Davis, 1976). Monthly mean ΔIDV_{me} at 35 m had positive correlation with wind speed, 0.345, and significant negative correlation, -0.361, with zonal wind. ΔIDV_{me} at 60 m had a strong positive correlation with wind speed, +0.557, and strong negative correlation with zonal winds, -0.580. These strong correlations and an examination of the monthly mean time series in Figure 6.6 show that ΔIDV_{me} increased with increased wind speed and easterly zonal winds. It is important to note that since diurnal variations of the local winds were small,

Table 6.1. Correlation coefficients between normalized monthly mean diurnal differences of isotherm displacement variance (ΔIDV) at 35m, 60m, and 100m and surface wind speed, zonal and meridional winds, and wind direction during the period November 1984 - October 1987. ΔIDV computed as 0400-1000 IDV minus 1600-2200 IDV. Statistical significance at the 95% confidence level was calculated based on the integral time scale between the time series (Davis, 1976). Statistically significant correlations are indicated by **Bold** type.

Variable 1	Variable 2	95% C.I.	r
Wind Speed	ΔIDV_035m	±0.353	0.345
	ΔIDV_060m	±0.392	**0.557**
	ΔIDV_100m	±0.324	0.216
Zonal Wind	**ΔIDV_035m**	±0.354	**-0.361**
	ΔIDV_060m	±0.397	**-0.580**
	ΔIDV_100m	±0.321	-0.230
Merid. Wind	ΔIDV_035m	±0.351	0.023
	ΔIDV_060m	±0.428	0.133
	ΔIDV_100m	±0.238	-0.022
Wind Dir.	ΔIDV_035m	±0.353	0.102
	ΔIDV_060m	±0.396	0.110
	ΔIDV_100m	±0.334	-0.061

about 0.2 ms^{-1}, it is unlikely that these correlations between the wind speed and zonal wind and ΔIDV_{me} at 35 m and 60 m were related to diurnal fluctuations of the local winds. The stronger correlations at 60 m could have been due to the shorter record length and large data gaps at 60 m during the boreal summers. The monthly mean values of ΔIDV_{me} at 100 m were not well correlated with wind speed or zonal wind. The monthly mean meridional wind and wind direction were not well correlated with ΔIDV_{me} at any of the TR depths.

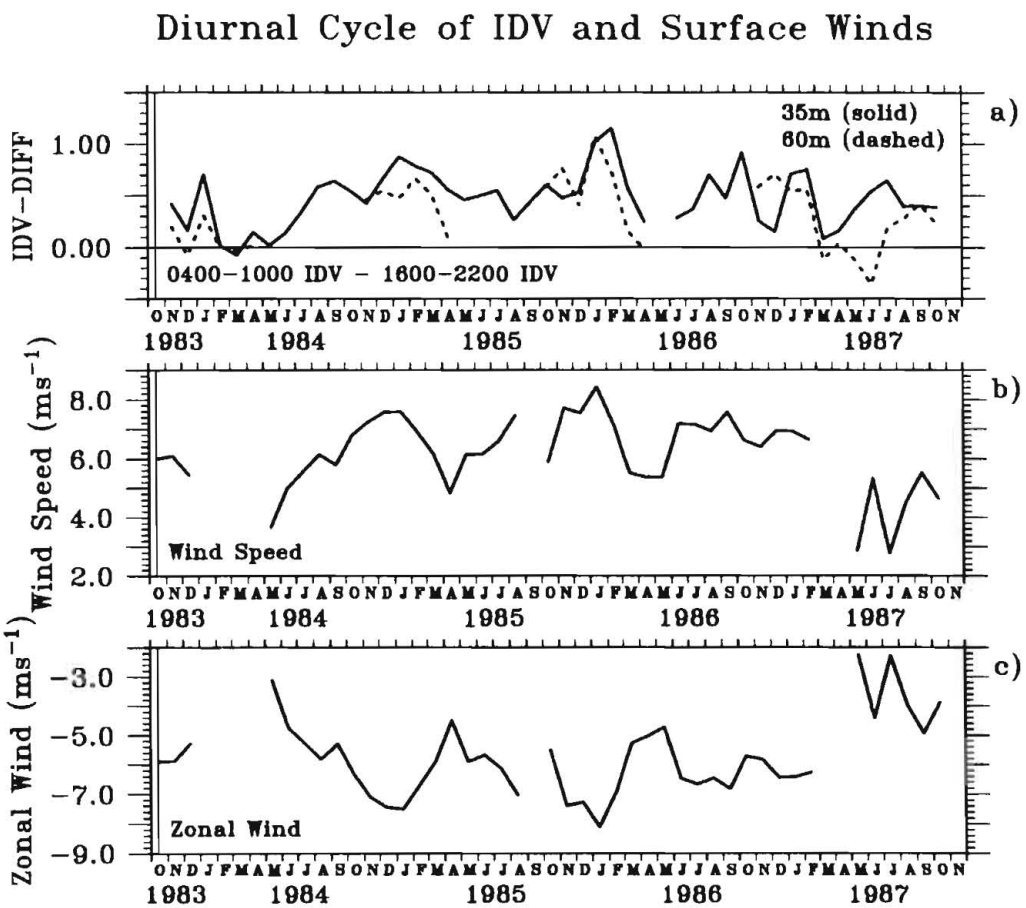

Figure 6.6. Time series of monthly mean diurnal differences of isotherm displacement variance (ΔIDV_{me}) at 35 m and 60 m, wind speed, and zonal wind during November 1983-October 1987. ΔIDV computed as 0400-1000 IDV minus 1600-2200 IDV normalized by the mean IDV.

2. Surface Heat and Buoyancy Fluxes

In Chapter V, statistical relationships between monthly mean IDV and monthly mean estimates of the surface heat and buoyancy fluxes were examined. Generally, correlations were weak. The only significant correlations were between IDV at 35 m and Q_e, and B_{net} during the evening time bin. In this section, relationships between the surface heat and buoyancy fluxes and the diurnal cycle of IDV in the upper 100 m are examined. Monthly means of the computed estimates of the terms of the surface heat flux and ΔIDV_{me} at 35 m and 60 m are shown in Figure 6.7. Correlation coefficients between the surface heat and buoyancy fluxes and ΔIDV_{me} at 35 m, 60 m, and 100 m are given in Table 6.2.

Earlier results showed that IDV in the upper 100 m was not well correlated with Q_s. The correlations between monthly mean ΔIDV_{me} at 35 m and 60 m and Q_s were 0.434 and 0.453, respectively. The correlation with ΔIDV_{me} at 35 m is statistically significant at the 95% confidence level based on the integral time scale of the two time series (Davis, 1976). Although the correlation with ΔIDV_{me} at 60 m was slightly greater than that at 35 m, it was not statistically significant due to greater confidence intervals associated with the shorter record length. The positive sign of these correlations indicates that ΔIDV_{me} increased during periods of increased shortwave radiation into the ocean. When monthly mean Q_s was anomalously low, such as during the 1984 ENSO cold episode and during the warming in 1987, the diurnal differences of IDV at 35 m and 60 m were low (Figure 6.2). Although increased shortwave radiation would increase the daytime stratification of the upper ocean, and hence reduce the daytime generation of convective mixing and possibly internal wave generation, the fact that Q_s is negligible during the nighttime hours means that an increase in daytime shortwave radiation corresponds to an increase in the diurnal difference in shortwave radiation. It is not unreasonable to expect an increase in the diurnal response of IDV when there was an increase in the diurnal solar forcing, and vice versa. Therefore, these results could be interpreted to indicate that increased Q_s results in an increase in the diurnal difference of IDV because of reduced daytime generation of IDV rather than due to increased

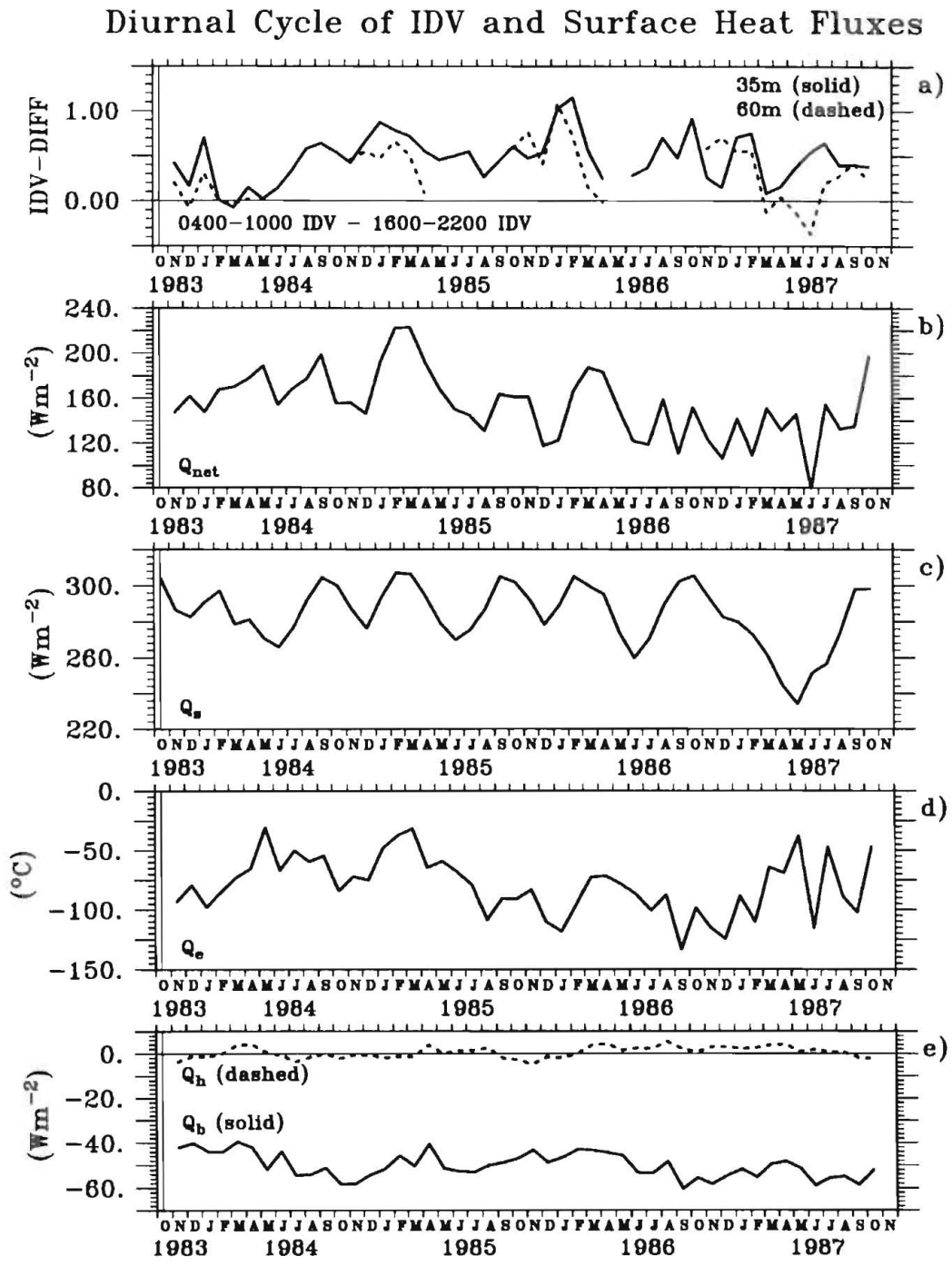

Figure 6.7. Time series of monthly mean a) diurnal differences of isotherm displacement variance (ΔIDV_{me}) at 35 m and 60 m, b) net surface net flux, Q_{net}, c) shortwave radiation, Q_s, d) latent heat flux, Q_e, and e) longwave radiation, Q_b, and sensible heat flux, Q_h, during November 1983-October 1987. ΔIDV_{me} computed as 0400-1000 IDV minus 1600-2200 IDV normalized by the mean IDV.

Table 6.2. Correlation coefficients between normalized monthly mean diurnal differences of isotherm displacement variance (ΔIDV) at 35 m, 60 m, and 100 m and surface heat and buoyancy fluxes, including net surface heat flux, Q_{net}, shortwave radiation, Q_s, latent heat flux, Q_e, sensible heat flux, Q_h, longwave radiation, Q_b, net surface buoyancy flux, B_{net}, and evaporation, E, during the period November 1983-October 1987. ΔIDV computed as 0400-1000 IDV minus 1600-2200 IDV. Statistical significance at the 95% confidence level was calculated based on the integral time scale between the time series (Davis, 1976). Statistically significant correlations indicated by **Bold** type.

VARIABLE 1	VARIABLE 2	95% C.I..	r
Q_{net}	ΔIDV 035m	±0.341	0.170
	ΔIDV 060m	±0.358	0.000
	ΔIDV 100m	±0.308	0.095
Q_s	ΔIDV 035m	±0.384	**0.434**
	ΔIDV 060m	±0.468	0.453
	ΔIDV 100m	±0.300	0.135
Q_e	ΔIDV 035m	±0.362	-0.061
	ΔIDV 060m	±0.423	-0.241
	ΔIDV 100m	±0.379	0.025
Q_b	ΔIDV 035m	±0.358	-0.062
	ΔIDV 060m	±0.429	-0.138
	ΔIDV 100m	±0.379	-0.064
Q_h	ΔIDV 035m	±0.358	**-0.359**
	ΔIDV 060m	±0.429	-0.415
	ΔIDV 100m	±0.311	0.012
B_{net}	ΔIDV 035m	±0.316	0.105
	ΔIDV 060m	±0.291	-0.156
	ΔIDV 100m	±0.305	0.260

nighttime generation of IDV. Although correlations were weak, comparison between daytime values of IDV at 35 m and 60 m (Figures 5.1a,b) and Q_s supports this interpretation.

Daytime IDV values were lowest during early 1984 and during most of 1987, both periods of anomalously low Q_s.

The only other term of the surface heat balance having significant correlation with ΔIDV_{me} in the upper 100 m was Q_h. The correlations between Q_h and the diurnal differences of IDV at 35 m and 60 m were -0.359 and -0.415, respectively. The negative sign of the correlations indicates that ΔIDV_{me} increased during periods when the sensible heat flux was from the ocean to the atmosphere. Although the sign agrees with intuition, the small relative magnitude of Q_h would not appear sufficient to generate significant convective mixing. Since Q_h is a function of wind speed, this significant correlation is most likely due to the strong correlation between wind speed and ΔIDV_{me}.

The remaining terms of the surface heat flux and the moisture flux terms of the surface buoyancy flux were not well correlated with ΔIDV_{me}.

E. DYNAMIC STABILITY AND THE DIURNAL CYCLE OF IDV

In this section, relationships between the dynamic stability during each of the four six-hour time bins and ΔIDV_{me} at 35 m, 60 m, and 100 m are examined. In Figures 4.8a-c, time-depth contour plots of monthly mean N, S, and Ri were presented. In examining the relationships between the diurnal cycle of IDV and the dynamic stability, diurnal variations of these dynamic stability parameters are discussed.

1. Buoyancy Frequency

Earlier results showed that N varied seasonally and interannually, and that these variations of N at several depths in the upper 100 m were negatively correlated with IDV at 35 m and 60 m, but not with IDV at 100 m. The correlations between the monthly mean ΔIDV_{me} at 35 m, 60 m, and 100 m and monthly means of local values of N for each of the four six-hour time bins are presented in Figure 6.8a. Significant negative correlation was observed at 35 m and 60 m for each of the four time bins. The negative

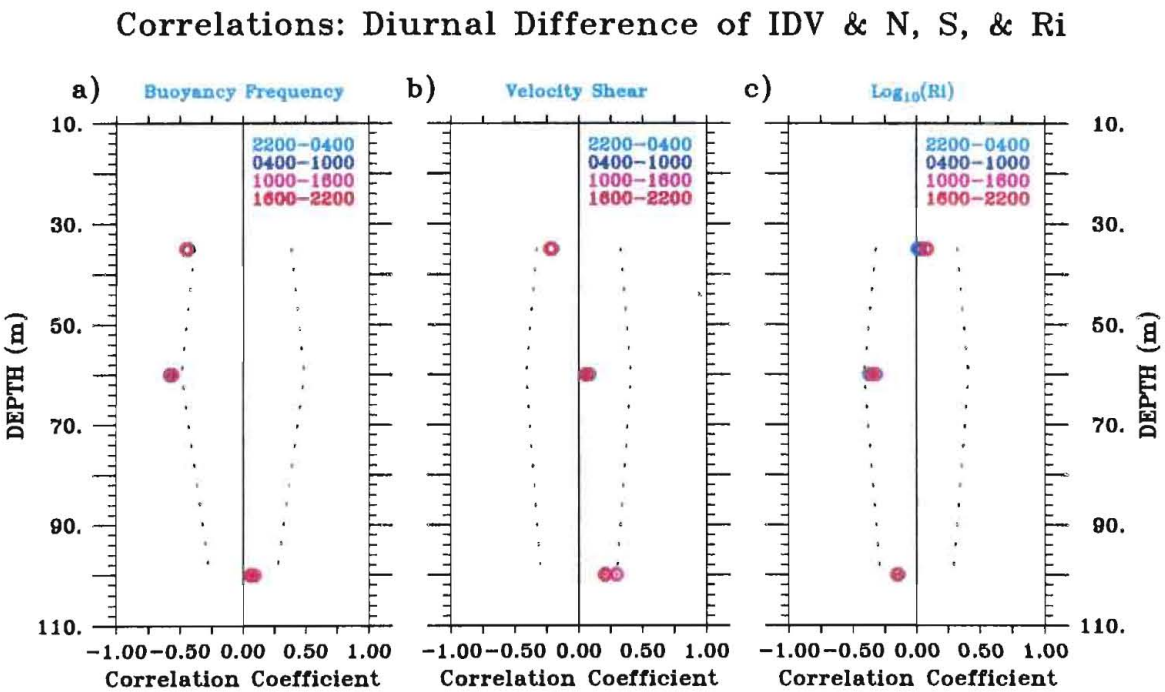

Figure 6.8. Correlation coefficients computed between diurnal differences of isotherm displacement variance (ΔIDV) and a) buoyancy frequency, N, b) velocity shear, S, and c) Richardson number, $\log_{10}(Ri)$ during November 1983-October 1987. ΔIDV computed as 0400-1000 IDV minus 1600-2200 IDV normalized by mean IDV.

sign of the correlations indicates that ΔIDV_{me} at 35 m and 60 m increased during periods of low N, and decreased during periods of high N. This suggests that strong stratification may have aided in suppressing the diurnal cycle of turbulence and high-frequency internal waves. Although daily values of ΔIDV_{me} were generally eliminated when the TRs were in the mixed layer before computing monthly statistics, the correspondence between high ΔIDV_{me} and low N suggests that the instruments were in the entrainment zone and that active mixing may have been occurring. If so, it would suggest that ΔIDV_{me} is largely a reflection of turbulence rather than internal waves.

Diurnal differences were computed from the fields of monthly mean N values between each of the four time bins. The resulting difference fields showed that the maximum diurnal differences occurred between the morning and evening time bins, as was observed for diurnal differences of IDV. Figure 6.9 is a time-depth contour plot of the monthly mean evening minus morning differences of N, ΔN_{em}. Large ΔN_{em} were observed in the upper 40 m or so, reflecting the strong diurnal mixing cycle associated with daytime stratification by solar heating and nighttime convective mixing. In the depth range of about 50-100 m, the sign of ΔN_{em} appeared to alternate with an annual period. During the boreal fall and winter months, values of ΔN_{em} in this depth range were small and positive, indicating that stratification increased slightly during the evening time bin. This penetration of the diurnal increase of N into the thermocline coincided with the pronounced increase of the diurnal cycle of IDV at 35 m and 60 m during the winter months (Figure 5.3a,b). Thus, this diurnal cycle of N in the thermocline appears to reflect the deep diurnal cycle of turbulence and internal waves that has been reported (Peters et al., 1988; Moum et al., 1989; McPhaden and Peters, 1992). During the boreal spring and summer months, values of ΔN_{em} in this 50-100 m depth range were strongly negative, indicating weaker stratification during the evening time bins, i.e. opposite the evening increase in stratification observed in the surface layer. The opposite sign of ΔN_{me} across the base of the mixed layer during these months indicates conventional mixed-layer dynamics with a diurnal buoyancy flux at the base of the mixed layer balanced by diurnally-steady upwelling by Ekman pumping. These seasonal variations of ΔN_{em} were

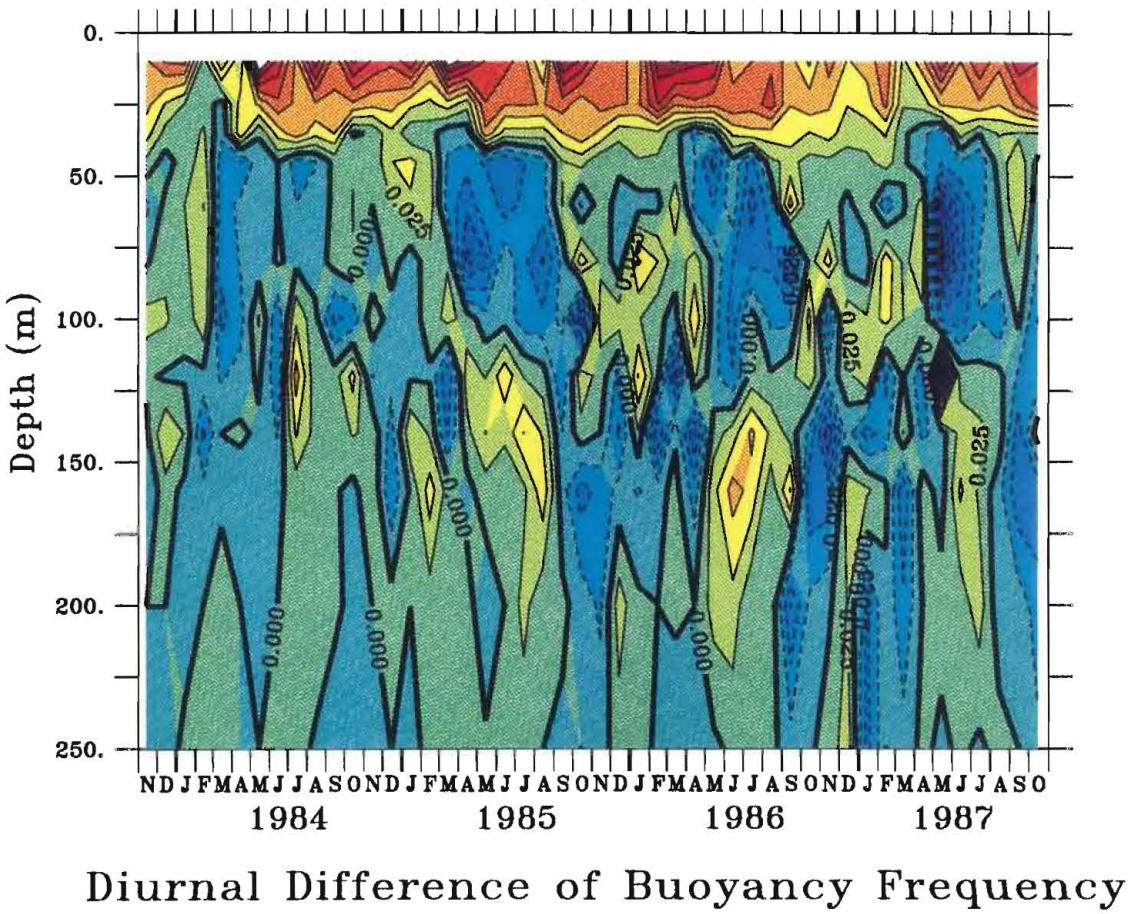

Figure 6.9. Time-depth contour plot of diurnal differences of monthly mean a) buoyancy frequency, ΔN_{em}, during November 1983-October 1987. ΔN_{em} computed as 1600-2200 N minus 0400-1000 N. Units are 10^{-2} x s^{-1}.

observed to vary interannually as well. During both the 1984 ENSO cold episode and the 1986/1987 ENSO warm episode, the daytime stratification of the surface layer was noticeably weaker.

Although pronounced diurnal differences of IDV and N were observed and ΔIDV_{me} at 35 m and 60 m was well correlated with N, correlations between ΔN_{em} and ΔIDV_{em} at 35 m, 60 m, and 100 m were not significant at the 95% confidence level. The fact that the diurnal cycle of IDV was correlated with N, but not ΔN_{em}, indicates that stratification in the surface layer may have provided a necessary, but not sufficient, condition for the diurnal cycle of the high-frequency variability.

2. Velocity Shear

In this section, the correlations between the diurnal cycle of IDV and shear, S, and its diurnal variations are examined. Figure 6.8b shows local correlations between monthly mean ΔIDV_{em} and S at 35 m, 60 m, and 100 m for each of the four six-hour time bins. At each of these three depths, correlations between S and ΔIDV_{em} were weak. Statistically significant correlation at the 95% confidence level was found only at 100 m and only during the day time bin.

Diurnal differences of monthly mean S between each of the four six-hour time bins showed that the maximum diurnal range occurred between the morning and evening time bins, ΔS_{em}, as was the case for IDV and N. Figure 6.10 is a time-depth contour plot of ΔS_{em}. Large ΔS_{em} was observed in the surface layer, which by this measure penetrated to between about 25 m and 50 m. Large positive ΔS_{em} in the surface layer indicates that shear increased during the evening time bin, a result consistent with observations and modeling studies showing a late afternoon diurnal jet caused by the increased stratification (Montgomery and Stroup, 1962; Schudlich, 1991). The vertical extent and magnitude of ΔS_{em} varied seasonally and interannually. On a few occasions, surface-related ΔS_{em} appeared to penetrate as deep as 100 m, most notably during the 1986/1987 ENSO warm episode with the passage of a pronounced Kelvin wave in November 1986. The seasonal cycle of ΔS_{em} in the surface layer was characterized by minima during the boreal spring and maxima during the boreal summer and fall.

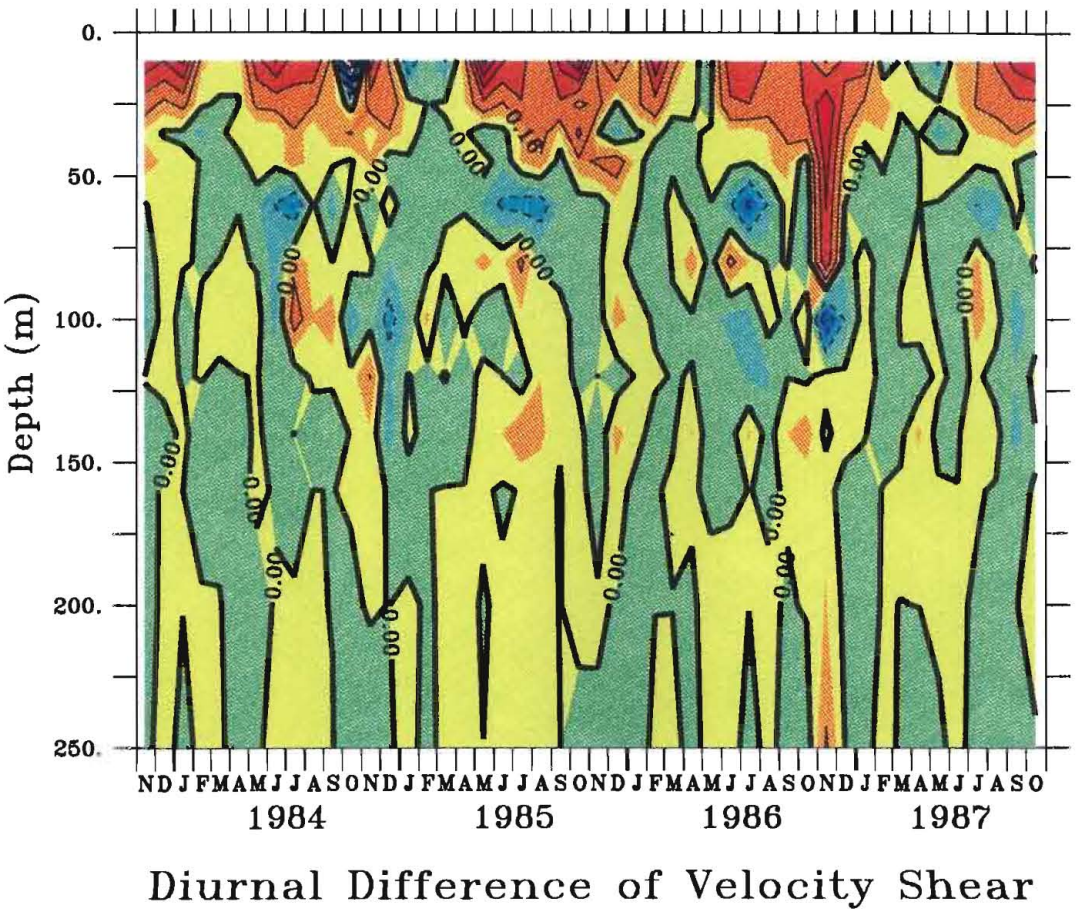

Figure 6.10. Time-depth contour plot of diurnal differences of monthly mean velocity shear, ΔS_{em}, during November 1983-October 1987. ΔS_{em} computed as 1600-2200 S minus 0400-1000 S. Units are 10^{-2} x s^{-1}.

As with the diurnal cycle of N, correlations between the diurnal cycle of S and the diurnal cycle of IDV at 35 m, 60 m, and 100 m were not statistically significant at the 95% confidence level.

3. Richardson Number

Local correlations between IDV and Ri in the upper 100 m were shown to be weak. Significant non-local correlations were found between IDV at 60 m and Ri at 80-120 m during the morning time bin and between IDV at 100 m and Ri at 10 m during the morning and evening time bins. In this section, the relationships between ΔIDV_{me} and Ri and the diurnal variations of Ri are examined. Figure 6.8c shows the local correlations between monthly mean ΔIDV_{me} and Ri at 35 m, 60 m, and 100 m for each of the four six-hour time bins. Correlations were weak at all three depths during all four time bins indicating that ΔIDV_{me} and Ri were not strongly related on these time scales.

Differences between monthly mean Ri for each of the four six-hour bins showed that the maximum diurnal range of Ri, ΔRi, occurred between the morning and evening time bins, ΔRi_{me}. A time-depth contour plot of ΔRi_{me}, Figure 6.11, shows large ΔRi_{me} occurred over seasonal and interannual time scales. Unexpected positive ΔRi_{me} indicates that surface layer Ri values were usually larger during the morning time bin than during the evening time bin. Generally, this positive ΔRi_{me} penetrated to about 25-50 m. There were occasions, however, when the vertical extent of these positive ΔRi_{me} extended to about 100 m, such as during the boreal winter of the 1986/1987 ENSO warm episode. During the 1984 ENSO cold episode, small ΔRi_{me} were observed in the surface layer while large positive ΔRi_{me} were observed between about 60 m and 130 m. The ΔRi_{me} in this latter depth range alternated in sign, with occasional periods of large negative ΔRi_{me} occurring during the 1986/1987 ENSO warm episode.

Correlations between ΔIDV_{me}, and ΔRi_{me} were not significant at 35 m, 60 m, and 100 m. The values of ΔIDV_{me} at 35 m were significantly correlated with the night minus day Ri difference, ΔRi_{nd}, at 35 m. This correlation was -0.36, indicating that the morning/evening ΔIDV at 35 m increased when the night/day diurnal difference of Ri decreased. Physically, it is unclear how a decrease in the diurnal difference in Ri could

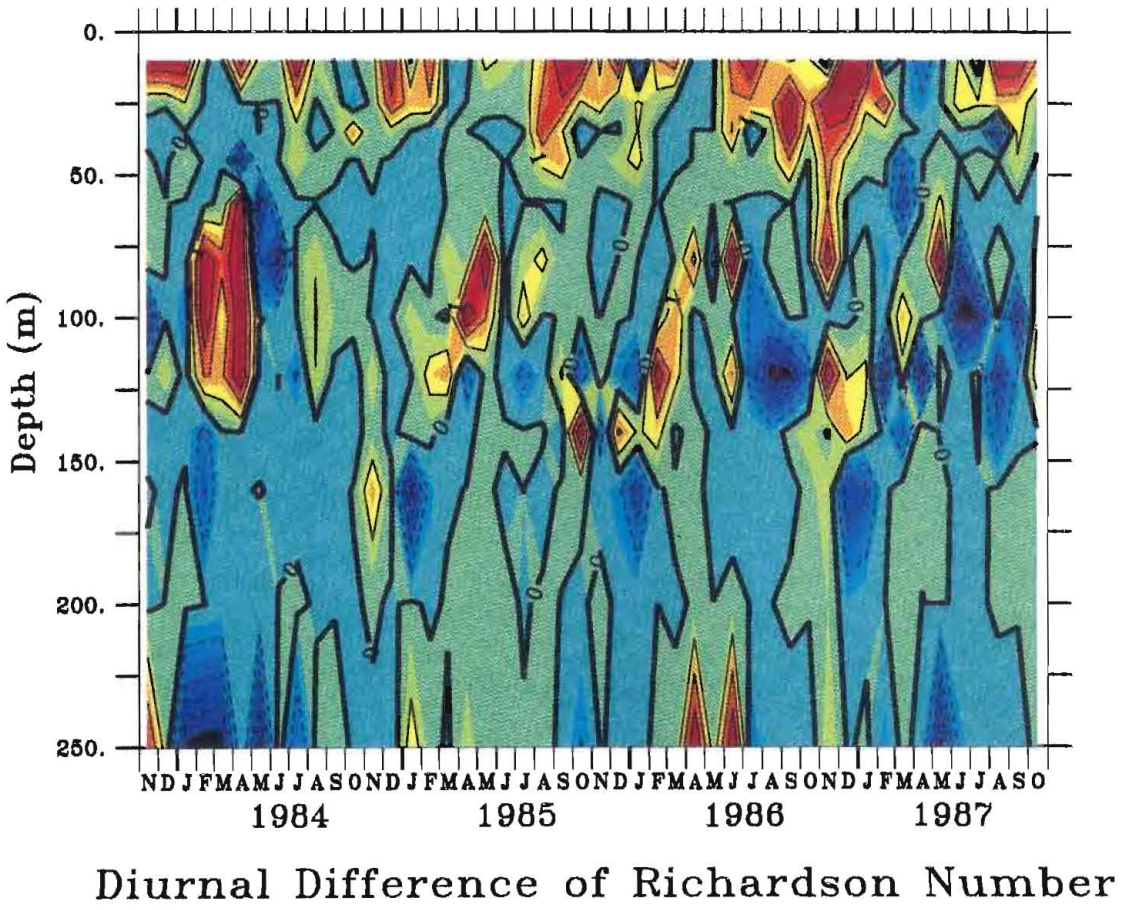

Figure 6.11. Time-depth contour plot of diurnal differences of monthly mean Richardson number, ΔRi_{me}, during November 1983-October 1987. ΔRi_{me} computed as 0400-1000 *Ri* minus 1600-2200 *Ri*.

be related to an increase in the diurnal cycle of turbulence or internal waves.

4. Longterm Mean Dynamic Stability

Although the correlations between monthly mean ΔIDV_{me} and the monthly mean diurnal differences of dynamic stability, ΔN_{em}, ΔS_{em}, and ΔRi_{me} were weak, the longterm mean diurnal differences suggest possible relationships. Figure 6.12 shows the four-year mean vertical profiles of ΔIDV_{me}, ΔN_{em}, ΔS_{em}, and ΔRi_{em} and the standard errors of the means. The longterm mean vertical structure of the diurnal cycle of IDV was discussed in section 6.1. Unlike Figures 5.2 and 6.3, which showed the longterm mean IDVs for each of the four time bins, Figure 6.12a shows the longterm mean ΔIDV_{me}. Recall that ΔIDV_{me} was computed as the monthly mean of the daily morning IDV minus the evening IDV normalized by the daily mean of the two IDV values. It is noteworthy that the standard errors of the mean ΔIDV_{me} are much smaller than the standard errors of the mean IDV. Although by this measure of significance ΔIDV_{me} at 100 m was significant, the sharp decay with depth of ΔIDV_{me} below 60 m agrees with the sharp decay with depth of IDV described previously. This difference in significance is a result of the normalization procedure, which acts to reduce the month-to-month variability by providing a relative measure of the diurnal difference of IDV.

The longterm mean ΔN_{em} was significantly positive in the upper 40 m and slightly negative between about 45 m and 100 m to one standard error of the mean (Figure 6.12b). In discussing Figure 6.9, a pronounced seasonal cycle of this change of sign of ΔN across the base of the mixed-layer was described. During the boreal winter, the diurnal cycle of N penetrated as deep as 100 m, reflecting the deep diurnal cycle of turbulent mixing. During the boreal summer, ΔN_{em} was negative in the thermocline region, indicating conventional mixed-layer physics with a diurnal buoyancy flux at the base of the mixed layer balanced by Ekman pumping. In the longterm mean (Figure 6.12b), a weak diurnal buoyancy flux from the surface layer to the thermocline is observed. The deep diurnal mixing cycle of the winter months apparently acts to reduce the buoyancy flux at the base of the mean mixed-layer.

A similar feature is apparent in the longterm mean ΔS_{em} profile. The longterm

mean ΔS_{em} was significantly positive in the upper 50 m and negative around 60 m, possibly indicating a diurnal momentum flux from the surface layer to the thermocline. It is important to note that the surface layer increase of S was nearly double the surface layer increase of N during the evening time bin. This is also reflected in the longterm mean profile of ΔRi_{em}, which shows significantly decreased Ri in the upper 50 m during the evening time bin. Investigators using TROPIC HEAT microstructure data indicated comparable or off-setting diurnal differences of N and S with no apparent diurnal differences of Ri (Chereskin et al., 1986; Moum et al., 1989). The Skyllingstad and Denbo (1994) model results showed increased instantaneous Ri in the mixed layer during the evening and decreased instantaneous Ri in the mixed layer during the morning. Similarly, preliminary results from TIWE data (Lien et al., 1994) have indicated increased Ri in the mixed layer during the evening and decreased Ri in the mixed layer during the morning.

The reasons for the apparent differences between the longterm mean diurnal differences of Ri computed here and those found during TIWE and in the Skyllingstad and Denbo model results remain uncertain. Examination of Figure 6.11 shows times when ΔRi_{me} was negative and agreed with the TIWE findings, i.e. higher Ri in the mixed layer during the afternoon. It is possible that since TIWE was conducted during the mature phase of the 1991/1992 ENSO warm event, the observed diurnal cycle of Ri may have indicated anomalous conditions. Figure 6.11 shows negative ΔRi_{me} during March through May 1987, which coincided with the mature phase of the 1986/1987 ENSO warm event. Some differences between results would also be expected due to different vertical and temporal resolution of the data. Whereas diurnal differences in Ri shown in Figure 6.12 include both times when the instruments (TRs and VACMs) were in the mixed layer and times when the instruments were below the mixed layer, the higher vertical resolution velocity data during TIWE enabled Lien et al. to examine these times separately.

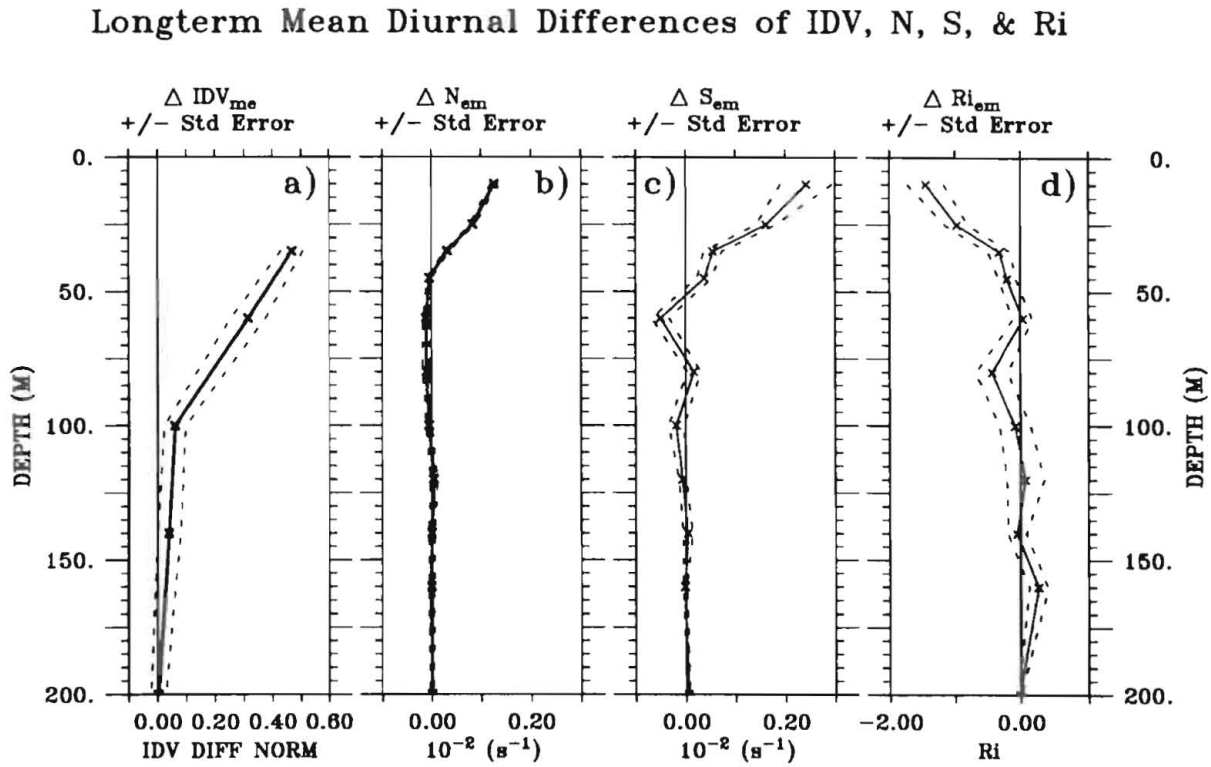

Figure 6.12. Longterm mean vertical profiles of diurnal differences of a) isotherm displacement variance, ΔIDV_{me}, b) buoyancy frequency, ΔN_{em}, c) velocity shear, ΔS_{em}, and D) Richardson number, ΔRi_{em}, computed over the period November 1983-October 1987. Dashed lines indicate ±one standard error of the mean.

F. MIXED-LAYER DEPTH AND THE DIURNAL CYCLE OF IDV

In section 5.6, strong correlation was observed between mixed-layer depth and IDV at both 35 m and 60 m. In this section, relationships between monthly mean ΔIDV_{me} at 35 m, 60 m, and 100 m and monthly mean mixed-layer depths for each of the four six-hour time bins and monthly mean diurnal ranges of mixed-layer depth are examined. Table 6.3 lists the correlation coefficients between each of these variables. Statistically significant correlations were observed between ΔIDV_{me} at 60 m and monthly mean mixed-layer depths for each of the evening, night, and morning time bins. These correlations were particularly strong during the night and morning time bins, -0.532 and -0.581, respectively. These negative correlations indicate that ΔIDV_{me} at 60 m increased during periods when the mixed layer was deep and decreased during periods when the mixed layer was shallow. In other words, when the mixed layer was deep, indicating either increased surface forcing or weakened background stability conditions or both, the diurnal difference of the high-frequency temperature variability increased at 60 m. Correlations between mixed-layer depth and ΔIDV_{me} at 35 m and 100 m were not significant at the 95% confidence level.

Significant positive correlations were observed between ΔIDV_{me} at 35 m and 60 m and the diurnal range of mixed-layer depth. The diurnal range of mixed-layer depth can be considered a measure of the nighttime mixing intensity. The positive correlations indicate that ΔIDV_{me} increased when the mixing intensity increased. This suggests a relationship between mixed layer dynamics and the diurnal cycle of the high-frequency temperature variability.

Table 6.3. Correlation coefficients, r, between monthly mean diurnal differences of IDV (ΔIDV_{mc}) at 35 m, 60 m, and 100 m and monthly mean mixed-layer depths (MLD) for four six-hour time bins and diurnal ranges of mixed-layer depth (ΔMLD) during November 1983-October 1987. ΔIDV_{mc} computed as 0400-1000 IDV minus 1600-2200 IDV normalized by mean IDV. ΔMLD computed as monthly mean of daily maximum MLD minus daily minimum MLD. Statistical significance at the 95% confidence level was calculated based on the integral time scale between time series (Davis, 1976). Statistically significant correlations are indicated by **Bold** type.

VARIABLES	2200-0400 95%c.i. r	0400-1000 95%c.i. r	1000-1600 95%c.i. r	1600-2200 95%c.i. r
MLD/ΔIDV_35	.359 -.197	.363 -.242	.354 -.054	.365 -.070
/ΔIDV_60	.406 **-.532**	.417 **-.581**	.389 -.353	.409 **-.428**
/ΔIDV_100	.268 -.079	.269 -.092	.290 -.007	.280 -.015
ΔMLD/ΔIDV_35	.327 **.443**			
/ΔIDV_60	.361 **.455**			
/ΔIDV_100	.295 .164			

G. DIURNAL CYCLE OF WAVE MOMENTUM FLUX

In section 6.1, the diurnal cycle of high-frequency temperature variability was shown to be confined above the core of the EUC, and in most cases above 100 m. To further examine the diurnal cycle of high-frequency variability in the upper equatorial ocean, 15-minute averaged velocity data were used to estimate the high-frequency wave momentum flux during November 1984. This period was chosen because it coincided with the microstructure measurements of the TROPIC HEAT 1 experiment and because the monthly mean profile of IDV shows a pronounced diurnal cycle penetrating well into the thermocline (Figure 6.13). During November 1984, the velocity shear was strong and stratification was relatively weak resulting in low Richardson numbers, *Ri* less than unity, down to 100 m. Surface winds were anomalously strong, with a mean wind speed of -7.01 ms^{-1}. The easterly zonal wind pseudo-stress was -51.89 m^2s^{-2} (McPhaden and McCarty, 1992). The monthly mean mixed-layer depth ranged between 11.8 m during the

IDV and *Ri* at 0°, 140°W During November 1984

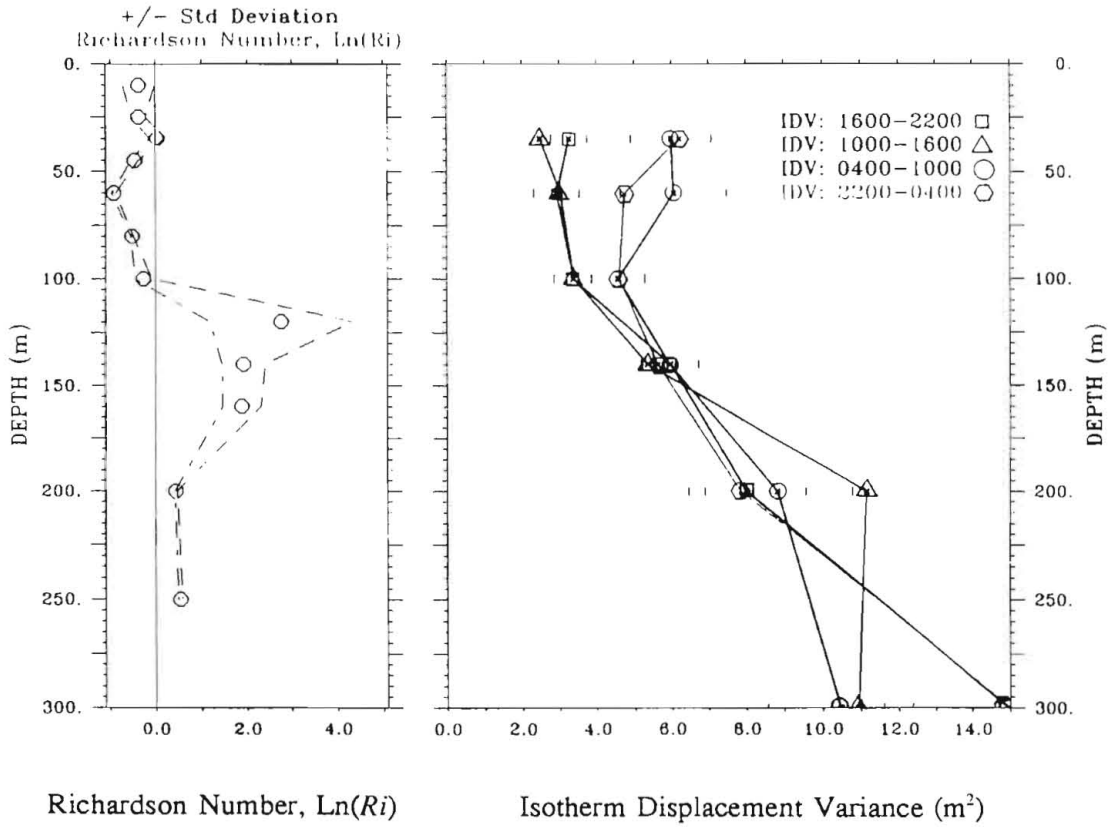

Figure 6.13. Monthly mean vertical profiles of isotherm displacement variance (IDV) during November 1984 for four six-hour time bins and monthly mean Richardson number profile. Error bars indicate ±1 standard error of the mean.

day time bin and 22.5 m during the morning time bin.

Figure 6.14 shows profiles of $\overline{u'w'}$ for each of the four six-hour time bins for the month of November 1984. Positive values of $\overline{u'w'}$ were observed in the depth range 45-120 m, indicating a downward flux of wave-induced westward momentum from the wind-driven surface flow to the EUC, decelerating the eastward flow. It appears that this downward flux of westward momentum did not penetrate the EUC core. The wave momentum flux divergence, $(\overline{u'w'})_z$, was divergent down to about 75 m and convergent below 75 m.

Diurnal differences of $\overline{u'w'}$ between the four time bins were not significant to one standard error of the mean, except at 25 m, where $\overline{u'w'}$ during the day time bin was greater than $\overline{u'w'}$ during the morning and evening time bins. Although these data indicate a vertical transport of energy from the surface layer to the EUC by high-frequency wave momentum flux, it appears that this flux was not related to diurnal forcing. It is likely that the observed wave momentum flux during November 1984 was driven by mechanical forcing by the anomalously large surface wind stress. It is not unreasonable to expect seasonal and interannual variability of the wave momentum flux, but since it does not appear related to the diurnal cycle of internal wave energy, these aspects are beyond the scope of this investigation.

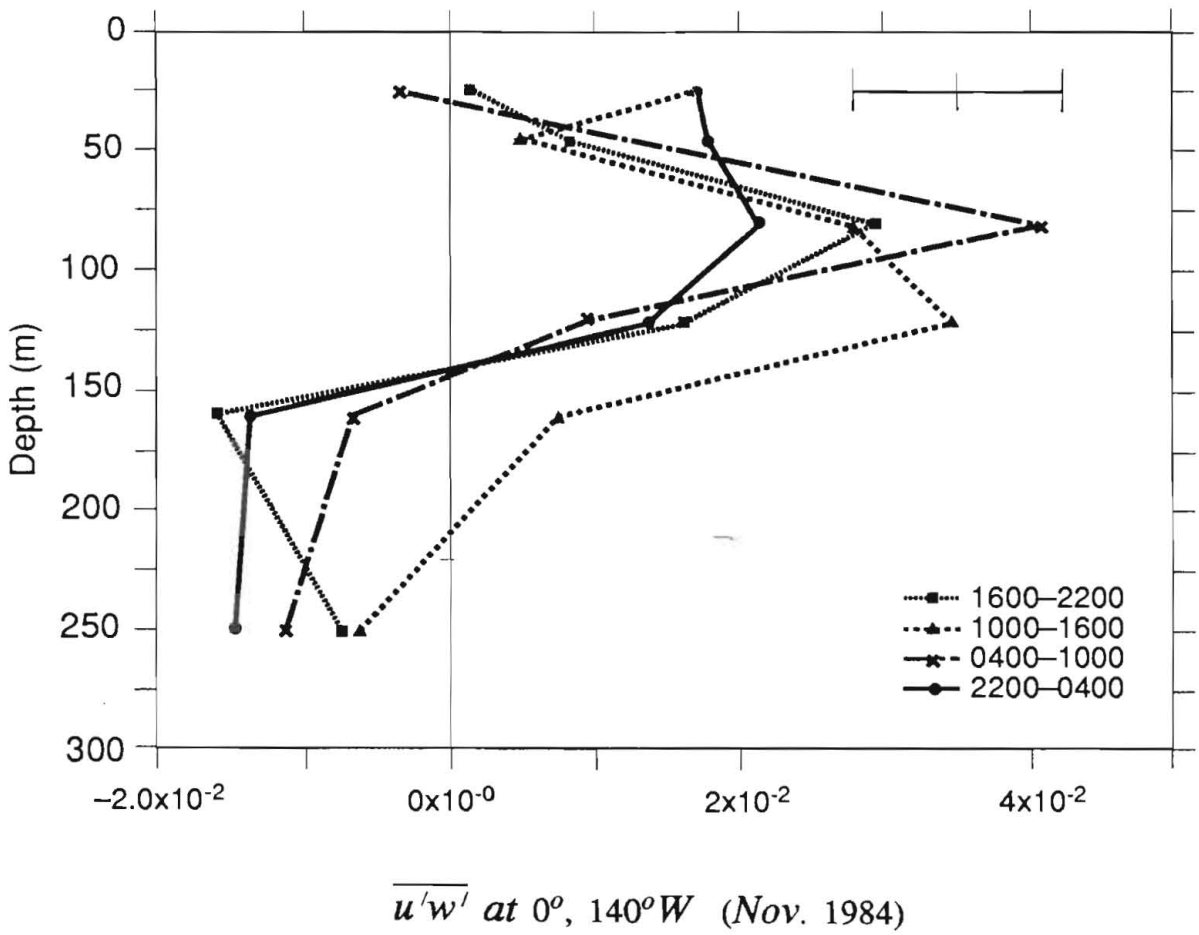

Figure 6.14. Monthly mean profiles of wave momentum flux for four six-hour time bins during November 1984. Method of computation described in section 3.2.8. Error bars indicate ±one standard error of the mean. Units are cm^2s^{-2}.

H. OTHER POSSIBLE SOURCES OF VARIANCE

1. Mooring Motion

Since the observations of high-frequency temperature variability used in the foregoing analyses were derived from moored buoy measurements that are known to be subject to vertical and horizontal motion, it is not unreasonable to assume that some of the temperature and velocity variability in the data were due to mooring motion. No independent measurements of mooring motion are available to accurately determine the contribution of mooring motion to such error. Unlike Boyd (1989) and Levine (1987), who were concerned about the effect of mooring motion on the vertical coherences of the internal wave spectrum, the concern here is whether or not mooring motion could degrade the observations of a diurnal cycle of high-frequency temperature variability. The most likely causes of increased mooring motion are wind and sea conditions. It is possible that part of the seasonal and interannual fluctuations of IDV that have been described are related to mooring motion caused by seasonal and interannual fluctuations of wind and sea conditions. However, since the diurnal variability of the surface winds is small at 0°, 140°W, it is not likely that the observed diurnal variations of IDV were related to mooring motion caused by these forces. Another possible cause of diurnal modulation of the temperature variability, either directly or indirectly by mooring motion, are the gravitational tides.

2. Gravitational Tides

Spectra of the unfiltered temperature and velocity data from the moorings have pronounced peaks at diurnal and semi-diurnal tidal frequencies. Since this study focuses on the diurnal variability of high-frequency wavelike motions, elimination or significant reduction of the diurnal and semi-diurnal tide from the data without significantly reducing the diurnal modulation of high-frequency waves is critical. Tidal analyses of both the temperature and velocity records showed 10-50% of the diurnal variance was removed by 32 harmonic constituents. These analyses were dependent on the depth and on the record length examined, which varied between 29 and 180 days. According to these harmonic analyses, the remaining 50-90% of the diurnal variance was determined to be unrelated to the barotropic tide. Although useful as an indicator of the

amount of tidal variance, the harmonic analyses are subject to errors associated with non-stationarity of the data. For the most part, the vertical temperature structure is affected by the baroclinic tide, but not the barotropic tide. Velocity, on the other hand, is affected by both baroclinic and barotropic tides.

The primary advantage of the procedure used in this study to filter the diurnal and semi-diurnal tide, described in section 3.1, was that it was applied locally and was therefore less subject to errors associated with the non-stationarity of the internal tides. A disadvantage of the procedure is the inability to easily quantify the role of the filter in reducing the variance. Although it is possible that some of the diurnal modulation of variance from the residual fields was tidally forced, the fact that the resulting residual variance had a well-defined vertical structure suggests that the barotropic tide was mostly removed. In their tidal analysis of velocity records in the eastern equatorial Pacific, Weisburg et al., (1987) found that the barotropic tide accounted for 78.8% of the tidal energy. The remaining baroclinic tide was random, isotropic, and without mode preference. Their partition between barotropic and baroclinic tidal energy is midway in the range of 50-90% given by Wunsch (1975) for the global ocean. Thus, it appears that most the tidal energy, that due to the barotropic tide, was reasonably well accounted for.

The remaining concern then lies with determining the impact of the baroclinic, or internal tide, on calculations using velocity data, such as velocity shear, Richardson number, and wave momentum flux. The internal tides are simply a form of internal wave with quasi-tidal periodicity (Wunsch, 1975). Theory and observations suggest that internal tides are generated by the passage of the barotropic tide over bathymetric features, though it is not possible to say with certainty that any of several mechanisms dominates (Wunsch, 1975). Variations in the density and velocity field near the generation region produce variations in the response of the internal tide. Away from the source, the internal tide is reflected and refracted by the density and velocity field though which it propagates, with the resulting internal tide being highly variable in time and space (Levine and Richman, 1989).

In evaluating the possible importance of the internal tide on the interpretation of results presented here, the surrounding bathymetry was compared with

the surrounding bathymetry for the analysis of Weisberg et al. (1987) from mooring data at 0°, 110° W. By comparison, the bathymetry near 0°, 140°W is relatively featureless. A few small seamounts are located about 250 km to the west. The shallowest of these is at a depth of about 2800 m, compared with the surrounding 4000 m abyssal plain. The nearest islands are the Marquesas located about 900 km to the south. Aside from the small seamounts, the nearest large bathymetric features in a zonal direction are about 1700 km to the west. The bathymetry surrounding the moored array used in Weisberg et al. (1987) is complex, with the east Pacific Rise and numerous fracture zones in close proximity. If internal tides are primarily generated by barotropic tides interacting with bathymetric features, as evidence suggests, it is not unreasonable to assume that the internal tide at 0°, 140°W would be no greater than, and possibly much less than, that described by Weisberg et al. (1987).

Examination of diurnal differences between four-year means of IDV and the dynamic stability parameters provide further indication that diurnal gravitational tides are not likely to have significantly modified the interpretation of results. The dominant diurnal tidal constituents, K1, P1, and O1, have periods of 23.93 hours, 24.07 hours, and 25.82 hours, respectively. These periods cause the constituents to shift relative to the solar day, with the K1 constituent retarding 3.93 minutes per day, the P1 constituent advancing 3.95 minutes per day, and the O1 constituent advancing almost two hours per day. Each year the K1 and P1 constituents cycle completely through a solar day, effectively averaging out shorter period contributions to the solar diurnal cycle. Calculations of means over the four-year record average over four complete K1 and P1 tidal cycles and over a hundred complete O1 tidal cycles. The fact that significant diurnal variations were observed in these longterm mean calculations and that the diurnal variations display significant vertical structure indicates that these diurnal cycles were forced by non-tidal processes.

VII. CONCLUSIONS

A. SUMMARY AND DISCUSSION

In this research, the diurnal cycle of high-frequency temperature fluctuations attributable to turbulence and internal waves in the upper central equatorial Pacific Ocean was examined over seasonal and interannual time scales. Using moored temperature and velocity data in the upper 300 m from 0^0, 140^0W during the period November 1983-October 1987, IDV, ΔIDV, and the vertical structure of ΔIDV were examined under surface forcing and dynamic stability conditions that varied over diurnal, seasonal, and interannual time scales. Using monthly mean values of ΔIDV as a proxy for turbulence and internal waves, a pronounced diurnal cycle of overturning and vertical displacement was observed at 35 m and 60 m, and this diurnal cycle was found to vary seasonally and interannually in response to the varying surface forcing and background conditions.

The diurnal cycle of turbulence and high-frequency internal waves was characterized by nighttime increases in IDV with maximum values occurring during the morning (0400-1000) time bin and minimum values occurring during the evening (1600-2200) time bin. This diurnal cycle of IDV is consistent with microstructure observations over a few short periods, showing that IDV is a useful proxy for turbulence and internal wave energy during periods when microstructure measurements are not available.

Since diurnal variations in the surface wind stress were small, IDV is presumed to have been diurnally-modulated by diurnal variations of the surface buoyancy flux, which were predominantly governed by the strong diurnal cycle of the shortwave radiation. In addition to regulating the diurnal cycle of IDV, the surface buoyancy flux induced pronounced diurnal variations of the mixed-layer depth and associated dynamic stability in the upper 50-100 m. As with ΔIDV, the diurnal differences of mixed-layer depth, N, S, and Ri were largest between the morning and evening time bins. As expected, N and S in the upper 50 m increased during the afternoon restratification. An interesting finding is that S increased by a factor of two more than N, resulting in decreased Ri in

the upper 50-60 m during the afternoon. This four-year mean diurnal cycle of *Ri* was contrary to short-term microstructure observations showing no apparent diurnal variation of *Ri* (Chereskin et al., 1986; Moum et al., 1989) or an opposite diurnal cycle of *Ri* in the mixed-layer (Lien et al., 1994). There were a few times during the four-year study period, most notably during the mature phase of the 1986/1987 ENSO warm event, when *Ri*'s computed from the mooring data were larger during the evening, in agreement with the Lien et al. (1994) results, which were based on observations taken during the mature phase of the 1991/1992 ENSO warm event. Differences in *Ri* results could also be related to large differences in the vertical and temporal resolution of the data. The longterm mean diurnal cycle of *Ri* reported here includes observations when the instruments were in the mixed layer and observations when the instruments were below the mixed layer.

In the four-year mean, the diurnal cycle of turbulence and internal waves, as proxied by ΔIDV, decayed sharply with depth below 60 m and was not significant at 100 m or deeper. Likewise, vertical correlations between ΔIDV_{me} at 35 m and ΔIDV_{me} at 60 m, 100 m, 140 m, 200 m, and 300 m indicated sharp decay with depth below 60 m. This is not to say that ΔIDV never penetrated below 60 m. In fact, on monthly time scales a weak diurnal cycle of IDV was observed at 100 m during about 29% of the months examined. Nevertheless, the combined longterm means and vertical correlations indicate that the diurnal cycle of turbulence and internal waves generally did not extend below the EUC. Therefore, it appears unlikely that vertical propagation of diurnally-forced waves from the surface layer to the deeper waters below the EUC contributed significantly to the equatorial momentum balance, as has been hypothesized by Dillon et al. (1989) and Wijesekera and Dillon (1991).

Although it cannot be determined with certainty whether these observations of IDV represent high-frequency internal waves, local shear instabilities, turbulent mixing, or some combination of these processes, the vertical structure of ΔIDV and the relationships between IDV and surface forcing, dynamic stability conditions, and mixed-layer depth provide important clues. The vertical structure of ΔIDV indicates that diurnally-forced vertically-propagating internal waves appear not to be transporting significant energy

from the surface layer through the EUC to the deep ocean. If vertically-propagating internal waves were generated in or near the base of the mixed layer, it appears that they did not propagate far vertically before breaking or triggering local shear instabilities and turbulent mixing.

Seasonally, both IDV and ΔIDV reached annual maxima during the boreal winter and minima during the boreal spring. These seasonal extrema coincided well with maximum wind speed and easterly zonal wind during the boreal winter and minimum wind speed and easterly zonal wind during the boreal spring. Similarly, mixed-layer depth and the diurnal range of mixed-layer depth had maxima during the winter and minima during the spring. Additionally, the seasonal cycle of the dynamic stability of the upper ocean was characterized by a narrow, high-S, low-Ri region at about 35 m during the boreal spring and a broad, weaker-S, low-Ri region at about the 60-m depth during the boreal winter. In summary, the boreal spring was characterized by weak winds, a shallow mixed layer, decreased diurnal range of mixed-layer depth, a shallow high-S, low-Ri region, and low IDV and ΔIDV. The boreal winter, on the other hand, was characterized by strong easterly winds, a deep mixed layer, increased diurnal range of mixed-layer depth, a relatively deep, broad, low-Ri region, and high IDV and ΔIDV.

The fact that IDV and ΔIDV at 35 m were at seasonal minima while the dynamic stability at 35 m was weakest suggests that IDV did not represent only local shear instabilities. In other words, the high-S, low-Ri region at 35 m during the boreal spring is expected to have been most likely to produce local shear instabilities. If local shear instabilities were generated, they were not reflected in the monthly mean IDV and ΔIDV. As the seasonal mixed layer and low-Ri region deepened to about 35 m and 60 m, respectively, during the boreal summer, IDV and ΔIDV both increased at 35 m, but remained low at 60 m. The low dynamic stability at 60 m did not correspond with increased IDV or ΔIDV. It is noteworthy that IDV and ΔIDV increased at 35 m, which was at the base of the mixed layer. During the boreal winter, when the mixed layer deepened to the seasonal maximum of about 50 m and the dynamic stability increased, IDV and ΔIDV increased to seasonal maxima at 35 m and 60 m, respectively. In this

case, temperature measurements at 35 m were often well within the mixed layer, as defined in this study. Although efforts were taken to remove IDV values at times when the instrument was within the mixed layer, it is possible that the remaining measurements of IDV at 35 m during the winter months were biased by turbulent mixing in the mixed layer, rather than internal waves or local shear instabilities. The winter IDV measurements at 60 m, on the other hand, were generally below the base of the mixed layer, so it is not clear whether ΔIDV represented increased IDV caused by internal waves, turbulent mixing, or a combination of these processes.

Over interannual time scales, IDV and ΔIDV showed some correspondence to ENSO variability, but this relationship was not always clear. The value of IDV at 35 m was observed to be low during the 1984 ENSO cold episode, steadily increasing during the ENSO build-up phase, and high during the 1986/1987 ENSO warm episode. The values of ΔIDV_{nd} at 35 m showed a similar pattern. The values ΔIDV_{me} at 35 m were similar, but values were higher during the ENSO build-up phase than during the mature phase of the 1986/1987 warm episode. Data gaps in the 60 m record made examination of the interannual variability more difficult. The values of IDV and ΔIDV at 60 m were low during the 1984 cold episode, high during the build-up phase and beginning of the 1986/1987 warm event, and low during the later half of the warm episode.

Monthly means of IDV at 35 m and 60 m over the four-year record were well correlated with wind speed, zonal wind, mixed-layer depth, diurnal range of mixed layer depth, latent heat flux, net surface buoyancy flux, and evaporation. Generally, IDV in the upper 60 m was significantly correlated with the stratification in the upper 100 m. Correlations between IDV and velocity shear and *Ri* were generally weak.

Monthly means of ΔIDV at 35 m and 60 m were well correlated with wind speed, zonal wind, shortwave radiation flux, sensible heat flux, diurnal range of mixed-layer depth, and buoyancy frequency in the upper 60 m. In addition, ΔIDV at 60 m was well correlated with mixed-layer depth. Each of the correlations was greater at 60 m than at 35 m, possibly a reflection of the shorter record length and data gaps during three of the boreal summers. The values of ΔIDV at 100 m were not well correlated with mixed-layer depth or any of the surface forcing or dynamic stability conditions.

What do these correlations between monthly mean values of IDV and ΔIDV and the surface forcing and background stability conditions reveal? Since both IDV and ΔIDV at 35 m and 60 m had the strongest correlations with the surface wind forcing, it seems reasonable that diurnal variations of IDV and ΔIDV were directly related to the amount of mechanical energy input into the ocean at the surface by the wind stress. Similarly, mixed-layer depth was strongly related to the surface wind stress, in agreement with most mixed layer theories. The complete explanation of the relationship between IDV and ΔIDV and mixed-layer depth is less certain. It is not unreasonable to suggest that processes controlling mixed-layer depth might have also contributed to the generation of the observed high-frequency temperature variability. In addition to mechanical forcing by the wind stress and thermodynamic forcing by the surface buoyancy flux, mixed-layer depth was strongly correlated with the dynamic stability parameters, N, S, and Ri. The relationships between dynamic stability and IDV and ΔIDV were not consistent on monthly time scales. Although shortwave radiation was significantly correlated with ΔIDV at 35 m, the lack of correlation with mean IDV is not readily explained.

High-frequency wave momentum flux during November 1984 indicated a downward flux of westward momentum from the wind-driven surface flow to the EUC, but apparently not through the core of the EUC. During November 1984, wave momentum flux did not appear to vary significantly on diurnal time scales. However, these wave momentum flux estimates were based on 15-minute averaged VACM data which effectively removed some of the high-frequency variability of interest.

B. CONCLUSIONS

The diurnal cycle of high-frequency temperature variability in the upper layers of the central equatorial Pacific Ocean was examined using moored buoy temperature and velocity data at 0°, 140°W, in the upper 300 m during the period November 1983-October 1987. The most noteworthy findings from this analysis are listed below.

- A pronounced diurnal cycle of IDV was observed at 35 m and 60 m, with a maximum during the morning hours and a minimum during the evening hours.

- The diurnal cycle of IDV decayed rapidly with depth below 60 m and was not generally significant at 100 m or deeper, indicating that it is unlikely that diurnally-forced waves propagate energy from the surface layer through the EUC core.

- The above two findings agree with microstructure observations and suggest that ΔIDV is a useful proxy for turbulence and internal waves in the equatorial Pacific Ocean.

- The diurnal cycle of turbulence and internal waves at both 35 m and 60 m, as proxied by ΔIDV, varied seasonally, with a maximum magnitude during the boreal winter and a minimum magnitude during the boreal spring.

- The diurnal cycle of turbulence and internal waves at both 35 m and 60 m, as proxied by ΔIDV, was strongly correlated with wind speed, zonal wind, mixed-layer depth, diurnal range of mixed-layer depth, and stratification in the upper 60 m.

- Pronounced diurnal cycles of the dynamic stability parameters were observed in the surface layer, with smaller Ri during the evening than during the morning.

REFERENCES

Akima, H., A new method of interpolation and smooth curve fitting based on local procedures, *J. of the ACM, 17,* 589-602, 1970.

Bishop, J.K.B., and W.B. Rossow, Spatial and temporal variability of global surface solar irradiance, *J. Geophys. Res., 96,* 16,839-16,858, 1991.

Bjerknes, J. Atmospheric teleconnections from the equatorial Pacific, *J. Phys. Oceanogr., 2,* 212-217, 1969.

Blumenthal, M.B., and M.A. Cane, Accounting for parameter uncertainties in model verification: an illustration with tropical sea surface temperature, *J. Phys. Oceanogr., 19,* 815-830, 1989.

Bond, N.A., and M.J. McPhaden, The diurnal cycle in the upper ocean heat content in the east-central equatorial Pacific, *Eos, Trans. Am. Geophys. Union, 75,* 130, 1994.

Booker, J.R., and F.P. Bretherton, The critical layer for internal gravity waves in a shear flow, *J. Fluid Mech.,27,* 513-539, 1967.

Boyd, T.J., Upper ocean internal waves in the central equatorial Pacific, Ph. D. Thesis, University of California, San Diego, Scripps Institution of Oceanography, 222pp, 1989.

Boyd, T.J., D.S. Luther, R.A. Knox, and M. C. Hendershott, High-frequency internal waves in the strongly sheared currents of the upper equatorial Pacific: observations and a simple spectral model, *J. Geophys. Res., 98,* 18,089-18,108, 1993.

Brainerd, K., and M.C. Gregg, Preliminary results of the COARE Microstructure pilot, *TOGA Notes, 4,* 1-6, 1991.

Bretherton, F.P., The propagation of groups of internal gravity waves in a shear flow, *Q.J.R. Meteorol. Soc., 92,* 446-480, 1966.

Bretherton, F.P., Momentum transport by gravity waves, *Q.J.R. Meteorol. Soc., 95,* 213-243, 1969.

Bryden, H.L., and E.C. Brady, Diagnostic model of the three-dimensional circulation in the upper equatorial Pacific Ocean, *J. Phys. Oceanogr., 15,* 1255-1273, 1985.

Bryden, H.L., and E.C. Brady, Eddy momentum and heat fluxes and their effects on the circulation of the equatorial Pacific Ocean, *J. Mar. Res., 47*, 55-79, 1989.

Bunker, A.F., Computations of surface energy flux and annual air-sea interaction cycles of the North Atlantic Ocean, *Mon, Wea. Rev., 104*, 1122-1140, 1976.

Busalacchi, A.J., and J.J. O'Brien, Interannual variability of the equatorial Pacific in the 1960's. *J. Geophys. Res., 86*, 10,901-10,907, 1981.

Caldwell, D.R., and T.M. Dillon, J.N. Moum, The rapid sampling vertical profiler, *J. Atmos. Oceanic Technol., 2*, 615-625, 1985.

Cane, M.A., Oceanographic events during El Nino, *Science, 222*, 1189-1195, 1983.

Carr, M.E., N.S. Oakey, B. Jones, M.R. Lewis, Hydrographic patterns and vertical mixing in the equatorial Pacific along 150°W, *J. Geophys. Res., 97*, 611-626, 1992.

Chereskin, T.K., J.N. Moum, P.J. Stabeno, D.R. Caldwell, C.A. Paulson, L. A. Regier, and D. Halpern, Fine-scale variability at 140°W in the equatorial Pacific, *J. Geophys. Res., 91*, 12,887-12,897, 1986.

Clark, N.E., L. Eber, R.M. Laurs, J.A. Renner, and J.F.T. Saur, Heat exchange between ocean and atmosphere in the eastern North Pacific for 1961-71. *NOAA Tech. Rep. NMFS SSRF-682*, National Oceanic and Atmospheric Administration, U.S. Dept. of Commerce, Washington, D.C., 1974.

Clark, T.L., T. Hauf, and J.P. Kuettner, Convectively forced internal gravity waves: Results from numerical experiments, *QJ. Meteorol.Soc.,112*, 899-925, 1986.

Crawford, W.R., and T.R. Osborn, Control of equatorial currents by turbulent dissipation, *Science, 212*, 539-540, 1981.

Crowe, E.L., F.A. Davis, and M.W. Maxfield, *Statistics Manual*, Dover Publications, Inc., New York, 288pp., 1960.

Darnell, W.L., W.F. Staylor, S.K. Gupta, and F.M. Dunn, Estimations of surface solar insolation using Sun-synchronous satellite data, *J. Clim.,1*, 820-835, 1988.

Davis, R.E., Predictability of sea surface temperature and sea level pressure anomalies over the North Pacific Ocean, *J. Phys. Oceanogr., 6*, 249-266, 1976.

Deser, C., Daily surface wind variations over the equatorial Pacific Ocean, submitted to *J. Geophys. Res.*, March 1994.

Dillon, T.M., and M.M. Park, The available potential energy of overturns as an indicator of mixing in the seasonal thermocline, *J. Geophys. Res., 92*, 5345-5353, 1987.

Dillon, T.M., J.N. Moum, T.K. Chereskin, and D.R. Caldwell, On the zonal momentum balance at the equator,*J. Phys., Oceanogr.,19*, 561-570, 1989.

Dorman, C.E., and R.H. Bourke, Precipitation over the Pacific Ocean, 30°S to 60°N, *Mon. Wea. Rev., 107*, 896-910, 1976.

Duing, W., and A. Leetmaa, Arabian sea cooling: A preliminary heat budget, *J. Phys. Oceanogr., 10*, 307-312, 1980.

Esbensen, S.K., and Y. Kushnir, The heat budget of the global ocean: An atlas based on estimates from surface marine observations, *Rep. 29*, 27pp., 188 charts, Clim. Res. Inst., Oreg. State Univ., Corvallis, 1981.

Eriksen, C.C., Evidence for a continuous spectrum of equatorial waves in the Indian Ocean, *J. Geophys. Res., 85*, 3285-3303, 1980.

Eriksen, C.C., The TROPIC HEAT Program: an overview. *Eos, Trans. Am. Geophys. Union, 66*, 50-52, 1985.

Freitag, H.P., M.J. McPhaden, and A.J. Shepherd, Equatorial current and temperature data: 108°W to 110°W: October 1979 to November 1983. *NOAA Data Rep. ERL PMEL-17*, 99pp., 1987.

Freitag, H.P., M.J. McPhaden, and A.J. Shepherd, Comparison of equatorial winds as measured by cup and propeller anemometers, *J. Atmos. Ocean. Tech., 6*, 328-332.

Freitag, H.P., and M.J. McPhaden, EPOCS moored temperature, current and wind measurements: 0°, 140°W; May-June 1987. *NOAA Data Rep. ERL PMEL-23*, 31pp., 1988.

Freitag, H.P., M.J. McPhaden, C.S. Coho, and A.J. Shepherd, Equatorial wind, current and temperature data: 108°W to 140°W; April 1983 to October 1987, *NOAA Data Rep. ERL PMEL-35*, 116pp., 1991.

Frouin, R., D.W. Lingner, C. Gautier, K.S. Baker, and R.C. Smith, A simple analytical formula to compute clear sky total and photosynthetically available solar irradiance at the ocean surface, *J. Geophys. Res., 94*, 9731-9742, 1989.

Fung, I., D.E. Harrison, and A.A. Lacis, On the variability of net longwave radiation at the ocean surface, *Rev. Geophys. Sp. Phys., 22*, 177-193,1984.

Garrett, C., and W.H. Munk, Space-time scales of internal waves, *Geophys. Fluid Dyn., 3*, 225-264, 1972.

Garrett, C. and W.H. Munk, Space-time scales of internal waves: a progress report, *J. Geophys. Res., 80*, 291-298, 1975.

Gargett, A.E., and T.R. Osborn, Small scale shear measurements during the fine and microstructure experiment, *J. Geophys. Res., 86*, 1929-1944, 1981.

Garwood, R.W., P.C. Chu, P. Muller, N. Schneider, Equatorial entrainment zone: the diurnal cycle. *Western Pacific International Meeting and Workshop on TOGA COARE Proceeding*, ed. J. Picaut, R. Lukas, and T. Delcroix. Centre ORSTROM de Noumea, New Caledonia publication, 435-443, 1989.

Gautier, C., G.R. Diak, and S. Masse, A simple physical model to estimate incident solar radiation at the sea surface from GOES satellite data, *J. Appl. Meteorol. 19*, 1005-1012, 1980.

Gill, A.E., *Atmosphere-Ocean Dynamics*, Academic Press, San Diego, CA, 662pp., 1982.

Gregg, M.C., Temperature and salinity microstructure in the Pacific equatorial undercurrent, *J. Geophys. Res., 81*, 1180-1196, 1976.

Gregg, M.C., and T. B. Sanford, Signatures of mixing from the Bermuda Slope, the Sargasso Sea, and the Gulf Stream, *J. Phys. Oceanogr., 10*, 105-127, 1980.

Gregg, M.C., H. Peters, J.C. Wessen, N.S. Oakey, and T.S. Shay, Intensive measurements of turbulence and shear in the equatorial undercurrent, *Nature, 318*, 140-144, 1985.

Halpern, D, R.A. Knox, D.S. Luther, and S.G.H. Philander, Estimates of equatorial upwelling between 140°W and 110°W During 1984, *J. Geophys. Res., 94*, 8018-8020, 1989.

Hansen, J.E., and L. Travis, Light scattering in planetary atmospheres, *Space Sci. Rev., 16*, 527-610, 1974.

Hayes, S.P., L.J. Mangum, J. Picaut, A. Sumi, and K. Takeuchi, TOGA-TAO: a moored array for real-time measurements in the tropical Pacific Ocean, *Bull. Amer. Meteor. Soc., 72*, 339-347, 1991.

Hastenrath, S., and P.J. Lamb, *Heat Budget Atlas of the tropical Atlantic and Eastern Pacific Oceans*, University of Wisconsin Press, 103pp., 1978.

Hebert, D., J.N. Moum, C.A. Paulson, D.R. Caldwell, T.K. Chereskin, and M.J. McPhaden, The role of the turbulent stress divergence in the equatorial Pacific momentum balance, *J. Geophys. Res., 96*, 7127-7136, 1991.

Hebert, D., J.N. Moum, C.A. Paulson, and D.R. Caldwell, Turbulence and internal waves at the equator. Part II: details of a single event, *J. Phys. Oceanogr., 22*, 1346-1356, 1992.

Horel,J.D. , and J.M. Wallace, Planetary scale atmospheric phenomena associated with the Southern Oscillation, *Mon. Weather Rev., 109*, 813-829, 1981.

Huff, T., and T.L. Clark, Three-dimensional numerical experiments on convectively forced internal gravity waves, *Q.J.R.Meteorol. Soc., 115*, 309-333, 1989.

Hughes, R.L., On the equatorial mixed layer, *Deep Sea Research, 27A*, 1067-1078, 1980.

Imawaki, S., P.P. Niiler, C.H. Gautier, D. Halpern, R.A. Knox, W.G. Large, D.S. Luther, J.C. McWilliams, J.N. Moum, and C.A. Paulson, A new method for estimating the turbulent heat flux at the bottom of the daily mixed layer, *J. Geophys. Res., 93*, 14,005-14,012, 1988.

Johnson, E.S., and D.S. Luther, Mean zonal momentum balance in the upper, central, equatorial Pacific Ocean, *J. Geophys. Res.*, in press, 1994.

Kase, R.H., and G. Siedler, Internal wave kinematics in the upper tropical Atlantic, *Deep Sea Res., 26*, suppl., 161-189, 1980.

Kessler, W.S., M.J. McPhaden, and K.M. Weickmann, Forcing of intraseasonal Kelvin waves in the equatorial Pacific, submitted to *J. Geophys. Res., 1994.*

Keuttner, J.P., P.A. Hildebrand, and T.L. Clark, Convection waves: Observations of gravity wave systems over boundary layers, *Q. J. R. Meteorol. Soc., 113*, 445-467, 1987.

Kraus, E.B., ed., *Modelling and Prediction of the Upper Layers of the Ocean*, NATO Advanced Study Institute, Urbino, Italy, Pergamon Press, 325 pp, 1977.

Kraus, E.B., The torque and flux balance in the upper equatorial ocean, *J. Geophys. Res.,92*, 14,242-14,250, 1987.

Lau, K.M., Oscillations in a simple equatorial climate system. *J. Atmos. Sci., 38*, 248-261, 1981.

Levine, M.D., The upper ocean internal wave field: influence of the surface and mixed layer, *J. Geophys. Res., 92*, 5035-5044, 1987.

Levine, M.D., R.A. deSzoeke, and P.P. Niiler, Internal waves in the upper ocean during MILE, *J. Phys. Oceanogr., 13*, 240-257, 1983a.

Levine, M.D., C.A. Paulson, M.G. Briscoe, R.A. Weller, and H. Peters, Internal waves in JASIN, *Philos. Trans. R. Soc. London, Ser. A, 308*, 389-405, 1983b.

Levine, M.D., and J.G. Richman, Extracting the internal tide from data: methods and observations from the mixed layer dynamics experiment, *J. Geophys. Res., 94*, 8125-8134.

Lien, R.C., M.C. Gregg, and J.N. Moum, Turbulence variability at the equator in the central Pacific during the 1991 El Nino, *Eos, Trans. Am. Geophys. Union, 75*, 186, 1994.

Lindstrom, E., R. Lukas, R. Fine, E. Firing, S. Godfrey, G. Meyers, and M. Tsuchiya, The western equatorial Pacific Ocean Circulation Study, *Nature, 330*, 533-537, 1987.

Lombardo, C.P. and M.C. Gregg, Similarity scaling of viscous and thermal dissipation in a convecting surface boundary layer, *J. Geophys. Res., 94*, 10,441-10,449, 1989.

Lukas, R., and E. Lindstrom, The mixed-layer of the western equatorial Pacific Ocean. *Dynamics of the Oceanic Surface Mixed Layer. Proc., Aha Huliko'a, Hawaiian Winter Workshop,* University of Hawaii at Manoa, P. Muller and D. Henderson, Eds., 67-94, 1987.

Mason, P.J., and R.I. Sykes, A two-dimensional numerical study of horizontal roll vortices in an inversion-capped planetary boundary layer, *Q.J.R. Meteorol. Soc., 108*, 801-823, 1982.

McPhaden, M.J., and S.P. Hayes, Variability in the eastern equatorial Pacific Ocean during 1986-1988, *J. Geophys. Res., 95*, 13,195-13,208, 1990.

McPhaden, M.J., and H. Peters, Diurnal cycle of internal wave variability in the equatorial Pacific Ocean: results from moored observations, *J. Phys. Oceanogr., 22*, 1317-1329, 1992.

McPhaden, M.J., and B. A. Taft, Dynamics of seasonal and intraseasonal variability in the eastern equatorial Pacific, *J. Phys. Oceanogr., 18*, 1713-1732, 1988.

McPhaden, M.J., and M.E. McCarty, Mean seasonal cycles and interannual variations at 0°, 140°W during 1980-1991, *NOAA Tech. Memo. ERL PMEL-95*, 118pp., 1992.

Meisner, B.N., and P.A. Arkin, Spatial and annual variations in the diurnal cycle of large-scale tropical convective cloudiness and precipitation, *Mon. Wea. Rev., 115,* 2009-2032, 1987.

Merle, J. Seasonal heat budget in the equatorial Atlantic Ocean, *J. Phys. Oceanogr., 10,* 464-469,1980.

Molinari, R.L., J.F. Festa, and E. Marmolejo, Evolution of sea surface temperature in the tropical Atlantic Ocean during FGGE, 1979, II. Oceanographic fields and heat balance in the mixed layer, *J. Mar. Res., 43,* 67-81, 1985.

Moum, J.N., and D.R. Caldwell, Local influence on shear-flow turbulence in the equatorial ocean, *Science, 230,* 315-316, 1985.

Moum, J.N., D.R. Caldwell, and C.A. Paulson, Mixing in the equatorial surface layer, *J. Geophys. Res., 94,* 2005-2021, 1989.

Moum, J.N., D. Hebert, C.A. Paulson, and D.R. Caldwell, Turbulence and internal waves at the equator, Part I: Statistics from towed thermistors and a microstructure profiler, *J. Phys. Oceanogr.,22, 1330-1345,* 1992.

Moum, J.N., M.J. McPhaden, D. Hebert, H. Peters, C.A. Paulson, and D.R. Caldwell, Internal waves, dynamic instabilities, and turbulence in the equatorial thermocline: an introduction to three papers in this issue, *J. Phys. Oceanogr., 22,* 1357-1359, 1992.

Muller, P., On the diffusion of momentum and mass by internal gravity waves, *J. Fluid Mech., 77,* 789-823, 1976.

Muller, P., R.W. Garwood, Jr., and J.P. Garner, Effect of vertical advection on the dynamics of the oceanic surface mixed layer, *Annales Geophys., 2,* 387-398, 1984.

Munk, W.H., Internal waves and small-scale processes. *Evolution of Physical Oceanography,* B.A. Warren and C. Wunsch, Eds., MIT Press, 264-290, 1981.

Oberhuber, J.M., An atlas based on the 'COADS' data set: The budgets of heat, buoyancy and turbulent kinetic energy at the surface of the global ocean. *Rep. 15,* Max-Planck-Institute for Meteorology, 20pp., 1988.

Obukhov, A.M., Turbulence in an atmosphere with nonuniform temperature, *Trudy Inst. Teoret. Geofiz. AN SSSR, 1,* 1946; translated and reprinted in *Bound.-Layer Meteor. 2,* 1971.

Pacanowski, R.H., and S.G.H. Philander, Parameterization of vertical mixing in numerical models of tropical oceans, *J. Phys. Oceanogr., 11*, 1443-1451, 1981.

Peters, H., Gregg, M.C., D.R. Caldwell, and J.N. Moum, Equatorial vertical mixing. In *Further Progress in Equatorial Oceanography*, (E.J. Katz and J.M. Witte, eds.), Nova Univ. Press, Fort Lauderdale, Florida, 1987.

Peters, H., M.C. Gregg, and J.M. Toole, On the parameterization of equatorial turbulence, *J. Geophys. Res., 93*, 1199-1218, 1988.

Peters, H., M.C. Gregg, and J.M. Toole, Meridional variability of turbulence through the equatorial undercurrent. *J. Geophys. Res., 94*, 18,003-18,009, 1989.

Philander, S. G., *El Nino, La Nina, and the Southern Oscillation*, Academic Press, San Diego, 293 pp., 1990.

Pinkel, R., Upper ocean internal wave observations from Flip, *J. Geophys. Res., 80*, 3892-3910, 1975.

Pinkel, R., Observations of the near-surface internal wavefield, *J. Geophys. Res., 11*, 1248-1257, 1981.

Pinkel, R., Doppler sonar observations of internal waves: The wavenumber-frequency spectrum, *J. Phys. Oceanogr., 14*, 1249-1270, 1984.

Price, J.F., R.A. Weller, and R. Pinkel, Diurnal cycling: observations and models of the upper ocean response to diurnal heating, cooling, and wind mixing. *J. Geophys. Res., 91*, 8411-8427, 1986.

Rao, M.S.V., W.V. Abbott, and J.S. Theon, Satellite-derived global oceanic rainfall atlas (1973-1974), *NASA Goddard Space Flight Center*, National Aeronautics and Space Administration, 211pp, 1976.

Rasmussen, E.M., and J.M. Wallace, Meteorological aspects of the El Nino/Southern Oscillation, *Science, 222*, 1195-1202, 1983.

Reed, R.K., On estimating insolation over the ocean, *J. Phys. Oceanogr., 7*, 482-485, 1977.

Rossby, C.G., and R.B. Montgomery, The layer of frictional influence in wind and ocean currents, *Pap. Phys. Oceanogr. Meteor., 3*, 101 pp., 1935.

Rossow, W.B., L.C. Garder, P.J. Lu, and A.W. Walker, International Satellite Cloud Climatology Project (ISCCP) documentation of cloud data. *WMO/TD-No.266*, 78pp. + 2 appendices, World Meteorol. Organ., Geneva, 1988.

Rossow, W.B., and R.A. Schiffer, ISCCP cloud data products, *Bull. Am. Meteorol. Soc., 72*, 2-20, 1991.

Schneider, N., and P. Muller, The meridional and seasonal structures of the mixed-layer depth and its diurnal amplitude observed during the Hawaii-to-Tahiti Shuttle Experiment, *J. Phys. Oceanogr., 20,* 1395-1404, 1990.

Schopf, P.S., and M.A. Cane, On equatorial dynamics, mixed layer physics and sea surface temperature, *J. Phys. Oceanogr., 13*, 917-935, 1983.

Schudlich, R.R., Upper ocean dynamics during the LOTUS and TROPIC HEAT experiments, Ph.D. thesis, Massachusetts Institute of Technology/Woods Hole Oceanographic Institution, WHOI-91-29, 158 pp., 1991.

Schudlich, R.R., and J.F. Price, Diurnal cycles of current, temperature, and turbulent dissipation in a model of the equatorial upper ocean, *J. Geophys. Res., 97*, 5409-5422, 1992.

Seager, R., S.E. Zebiak, and M.A. Cane, A model of the tropical Pacific sea surface temperature climatology, *J. Geophys. Res., 93*, 1265-1280, 1988.

Shay, T.J., and M.C. Gregg, Convectively driven turbulent mixing in the upper ocean, *J. Phys. Oceanogr., 16*, 1777-1798, 1986.

Shea, D.J., Climatological atlas: 1950-1979, Surface air temperature, precipitation, sea-level pressure, and sea-surface temperature (45°S-90°N), *NCAR/TN-269+STR*, National Center for Atmospheric Research, Boulder, Colorado, 196pp, 1986.

Skyllingstad, E.D. and D.W. Denbo, The role of internal gravity waves in the equatorial current system. accepted to *J. Geophys. Res.*, 1994.

Shukla, J., and J.M. Wallace, Numerical simulations of the atmospheric response to equatorial Pacific sea surface temperature anomalies. *J. Atmos. Sci., 40*, 1613-1630, 1983.

Stevenson, J.W., and P.P. Niiler, Upper ocean heat during the Hawaii-to-Tahiti Shuttle Experiment. *J. Phys. Oceanogr., 13*, 1894-1907, 1983.

Stull, R.B., *An Introduction to Boundary Layer Meteorology*, Kluwer Academic Publishers, Boston, 666pp., 1988.

Stull, R.B., and E.B. Kraus, The transilient model of the upper ocean, *J. Geophys. Res., 92*, 10,745-10,755, 1987.

Takahashi, T., The carbon dioxide puzzle, *Oceanus, 32-2*, 22-29, 1989.

Takahashi, T., P. Tans, and I. Fung, Balancing the budget, *Oceanus, 35-1*, 18-28, 1992.

Tarpley, J.D., Estimating incident solar radiation at the surface from geostationary satellite data, *J. Appl. Meteorol., 18*, 1172-1181, 1979.

Thorpe, S.A., Turbulence and mixing in a Scottish loch, *Philos. Trans. R. Soc. London, Ser. A, 286*, 125-181, 1977.

Toole, J.M., and S.P. Hayes, Finescale velocity-density characteristics and Richardson number statistics of the eastern equatorial Pacific, *J. Phys. Oceanogr., 14*, 712-726, 1984.

Toole, J.M., H.Peters, and M.C. Gregg, Upper ocean shear and density variability at the equator during TROPIC HEAT, *J. Phys. Oceanogr., 17*, 1397-1406, 1987.

Trenberth, K.E., G.W. Branstator, and P.A. Arkin, Origins of the 1988 North American Drought, *Science, 242*, 1640-1645, 1988.

Turner, J.S., *Buoyancy Effects in Fluids*, Cambridge University Press, 368pp., 1973.

Weare, B.C., P.T. Strub, and M.D. Samuel, Annual mean surface heat fluxes in the tropical Pacific Ocean, *J. Phys. Oceanogr., 11*, 705-717, 1981.

Weisburg, R.H., D. Halpern, T.Y. Tang, and S.M. Hwang, M_2 Tidal Currents in the Eastern Equatorial Pacific Ocean, *J. Geophys. Res., 92*, 3821-3826, 1987.

Weller, R.A., and P.K. Taylor, Surface conditions and air-sea fluxes, *CCCO-JSC Ocean Observing System Development Panel*, 131pp., Texas A&M University, College Station TX 77843-3146, 1993.

Wijesekera, H. W., and T.M. Dillon, Internal waves and mixing in the upper equatorial Pacific Ocean, *J. Geophys. Res., 96*, 7115-7125, 1991.

Wunsch, C., Internal tides in the ocean, *Rev. Geophys. Sp. Phys., 13*, 167-182, 1975.

Wunsch, C., and S.Webb, The climatology of deep ocean internal waves, *J. Phys. Oceanogr., 9*, 235-243, 1979.

Wyrtki, K., The thermal structure of the eastern Pacific Ocean, *Dtsch. Hydrogr. Ze., Suppl* A8, 6-84, 1964.

Wyrtki, K., The average annual heat balance of the North Pacific Ocean and its relation to ocean circulation, *J. Geophys. Res., 70,* 4547-4559, 1965.

Wyrtki, K., El Nino - The dynamic response of the equatorial Pacific ocean to atmospheric forcing, *J. Phys. Oceanogr., 5*, 572-584, 1975.

Wyrtki, K., An estimate of equatorial upwelling in the Pacific, *J. Phys. Oceanogr., 11*, 1205-1214, 1981.

Yue, F., H.P. Freitag, M.J. McPhaden, A.J. Shepherd, Wind, current, and temperature data at 0°, 165°E: January 1986 to March 1991, *NOAA Data Rep. ERL PMEL-36*, 54pp., 1991.

INITIAL DISTRIBUTION LIST

1.	Defense Technical Information Center Cameron Station Alexandria, VA 22304-6145	2
2.	Library, Code 52 Naval Postgraduate School Monterey, CA 93943-5002	2
3.	NOAA, Pacific Marine Environmental Laboratory 7600 Sand Point Way N.E. Seattle, WA 98115-0700	
	Attn: Director	1
	Dr. Michael J. McPhaden	2
	Dr. Nick Bond	1
	Dr. Eric S. Johnson	1
	Dr. Meghan Cronin	1
4.	Department of Oceanography	
	Attn: Chairman	1
	Prof. Roland W. Garwood, Jr., Code OC/Gd	2
	Prof. Albert J. Semtner, Code OC/Se	1
	Naval Postgraduate School Monterey, CA 93943-5000	
5.	Department of Meteorology Attn: Prof. Kenneth L. Davidson, Code MR/DS Naval Postgraduate School Monterey, CA 93943-5000	1
6.	Office of Naval Research Attn: Dr. Steven R. Ramp, Code 322PO Balston Tower 1, 4th Floor, Room 407-21 800 North Quincy Street Arlington, VA 22217	1
7.	Commanding Officer NOAA Ship TOWNSEND CROMWELL Attn: Lieutenant Commander Russell E. Brainard, NOAA #1 Sand Island Access Road Honolulu, HI 96819	10

8. Applied Physics Laboratory, HN-10
University of Washington
Attn: Dr. Ren-Chieh Lien 1
Dr. Mike C. Gregg 1
Dr. Hemantha W. Wijesekera 1
Seattle, WA 98195

9. College of Oceanography
Oregon State University
Attn: Dr. James N. Moum 1
Dr. Thomas M. Dillon 1
Dr. Murray D. Levine 1
Dr. Timothy J. Boyd 1
Corvallis, OR 97331

10. Scripps Institution of Oceanography
University of California, San Diego
Attn: Dr. Janet Sprintall 1
Dr. Niklas Schneider 1
9500 Gilman Drive MS-A-030
La Jolla, CA 92093-0230

11. Battelle/Marine Sciences Laboratory 1
1529 West Sequim Bay Road
Attn: Dr. Eric D. Skyllingstad
Sequim, WA 98382

12. Shannon Point Marine Laboratory 1
Western Washington University
Attn: Ms. Mary Anne Brainard
Anacortes, WA 98221

13. Rear Admiral Sigmund R. Petersen, NOAA 1
Director, Office of NOAA Corps Operations
1315 East-West Highway
Silver Spring, MD 20910-3282

14. Ocean Physics Group 1
Department of Earth Sciences
Attn: Dr. Dave Foley
University of Southern California
Los Angeles, CA 90089-0740